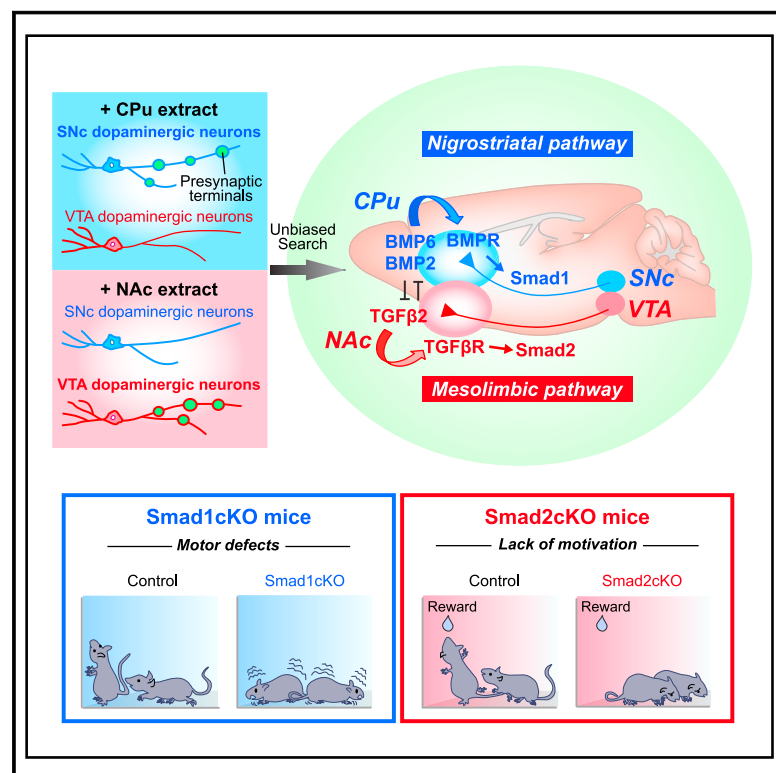


# The projection-specific signals that establish functionally segregated dopaminergic synapses

## Graphical abstract



## Authors

Akiko Terauchi, Patricia Yee, Erin M. Johnson-Venkatesh, ..., David D. Ginty, Wei-Chung A. Lee, Hisashi Umemori

## Correspondence

hisashi.umemori@childrens.harvard.edu

## In brief

Dopaminergic synapse formation of nigrostriatal and mesolimbic neurons is determined by distinct BMP6/2–Smad1 and TGF-β2–Smad2 pathways.

## Highlights

- An unbiased search identified projection-specific dopaminergic synaptic organizers
- BMP6/2–Smad1 and TGF-β2–Smad2 axes establish nigrostriatal vs. mesolimbic synapses
- BMP6, BMP2, and TGF-β2 synergize or antagonize to establish dopaminergic synapses
- Smad1 mutant mice show motor defects, and Smad2 mutant mice show a lack of motivation



## Article

# The projection-specific signals that establish functionally segregated dopaminergic synapses

Akiko Terauchi,<sup>1</sup> Patricia Yee,<sup>1</sup> Erin M. Johnson-Venkatesh,<sup>1</sup> Mariel P. Seiglie,<sup>1</sup> Lisa Kim,<sup>1</sup> Julia C. Pitino,<sup>1</sup> Eli Kritzer,<sup>1</sup> Qiyu Zhang,<sup>2</sup> Jie Zhou,<sup>3</sup> Yulong Li,<sup>4</sup> David D. Ginty,<sup>2</sup> Wei-Chung A. Lee,<sup>1</sup> and Hisashi Umemori<sup>1,5,\*</sup>

<sup>1</sup>Department of Neurology, F.M. Kirby Neurobiology Center, Boston Children's Hospital, Harvard Medical School, Boston, MA 02115, USA

<sup>2</sup>Department of Neurobiology and Howard Hughes Medical Institute, Harvard Medical School, Boston, MA 02115, USA

<sup>3</sup>Department of Computer Science, Northern Illinois University, DeKalb, IL 60115, USA

<sup>4</sup>State Key Laboratory of Membrane Biology, PKU-IDG/McGovern Institute for Brain Research, Peking-Tsinghua Center for Life Sciences, Peking University, Beijing 100871, China

<sup>5</sup>Lead contact

\*Correspondence: [hisashi.umemori@childrens.harvard.edu](mailto:hisashi.umemori@childrens.harvard.edu)

<https://doi.org/10.1016/j.cell.2023.07.023>

## SUMMARY

Dopaminergic projections regulate various brain functions and are implicated in many neuropsychiatric disorders. There are two anatomically and functionally distinct dopaminergic projections connecting the midbrain to striatum: nigrostriatal, which controls movement, and mesolimbic, which regulates motivation. However, how these discrete dopaminergic synaptic connections are established is unknown. Through an unbiased search, we identify that two groups of antagonistic TGF- $\beta$  family members, bone morphogenetic protein (BMP)6/BMP2 and transforming growth factor (TGF)- $\beta$ 2, regulate dopaminergic synapse development of nigrostriatal and mesolimbic neurons, respectively. Projection-preferential expression of their receptors contributes to specific synapse development. Downstream, Smad1 and Smad2 are specifically activated and required for dopaminergic synapse development and function in nigrostriatal vs. mesolimbic projections. Remarkably, Smad1 mutant mice show motor defects, whereas Smad2 mutant mice show lack of motivation. These results uncover the molecular logic underlying the proper establishment of functionally segregated dopaminergic synapses and may provide strategies to treat relevant, projection-specific disease symptoms by targeting specific BMPs/TGF- $\beta$  and/or Smads.

## INTRODUCTION

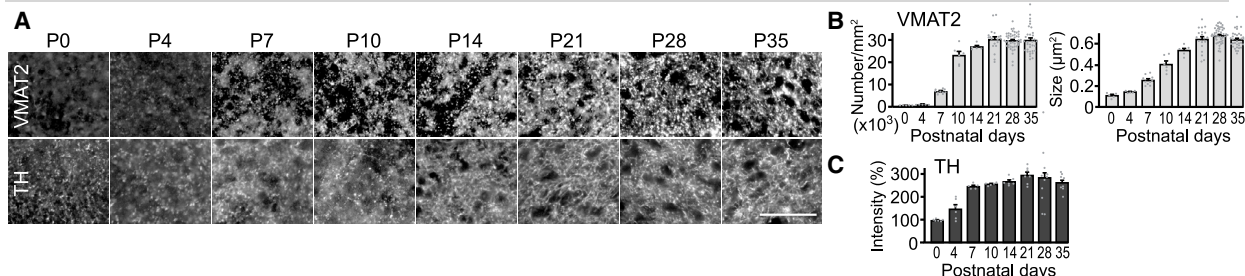
Dopaminergic pathways from the midbrain to the striatum play critical roles in many brain functions.<sup>1</sup> Dysfunction of these pathways is associated with numerous psychiatric and neurological disorders including drug addiction, attention-deficit/hyperactivity disorder (ADHD), schizophrenia, depression, and Parkinson's disease. Anatomically and functionally, the midbrain-to-striatum dopaminergic connections are classified into two separate pathways: the nigrostriatal and the mesolimbic pathways.<sup>2</sup> The nigrostriatal pathway transmits dopaminergic signals from the substantia nigra pars compacta (SNc) to the dorsal striatum (caudate-putamen [CPu]). The nigrostriatal pathway largely controls motor functions, and defects in this pathway are implicated in Parkinson's and Huntington's disease.<sup>3–5</sup> By contrast, the mesolimbic pathway transmits dopaminergic signals from the ventral tegmental area (VTA) to the ventral striatum (nucleus accumbens [NAc]). This pathway regulates motivation, emotion, and reward association and is implicated in addiction.<sup>6–8</sup> Therefore, the dopaminergic synaptic connections of these distinct pathways must be specifically established during

development for the optimal functioning of the brain. The understanding of the manner and molecules by which appropriate dopaminergic connections are established may also yield new insights into both the etiology and treatment of the neuropsychiatric disorders associated with defects in the dopaminergic pathways. There is, therefore, intense interest in elucidating the factors and mechanisms that control the establishment of dopaminergic synaptic connections.

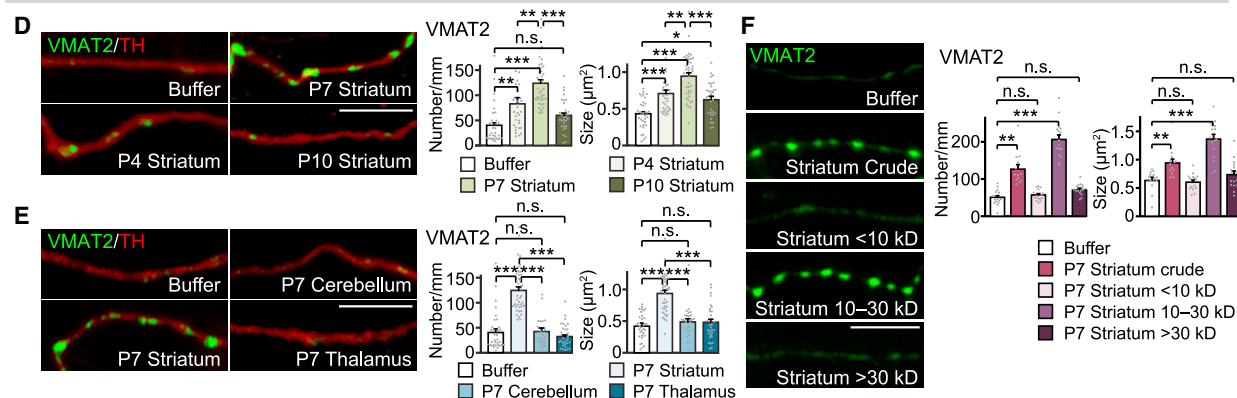
Here, by characterizing the development of dopaminergic synapses and performing an unbiased search, we identify that two groups of target-derived transforming growth factor  $\beta$  (TGF- $\beta$ ) family members, bone morphogenetic protein (BMP)6/BMP2 and TGF- $\beta$ 2, regulate dopaminergic synapse development in nigrostriatal and mesolimbic neurons, respectively. We further show that BMP6, BMP2, and TGF- $\beta$ 2 synergize or antagonize to establish appropriate dopaminergic synapses. Pathway-preferential expression of the BMP receptor (BMPR) and TGF- $\beta$  receptor (TGF- $\beta$ R) also contributes to specific dopaminergic synapse formation. Finally, we show that distinct signaling molecules, Smad1 and Smad2, are specifically activated and required for dopaminergic synapse development and function



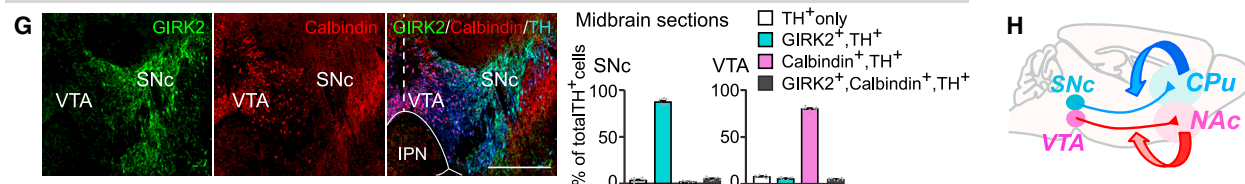
## Time course of dopaminergic synapse development in the striatum



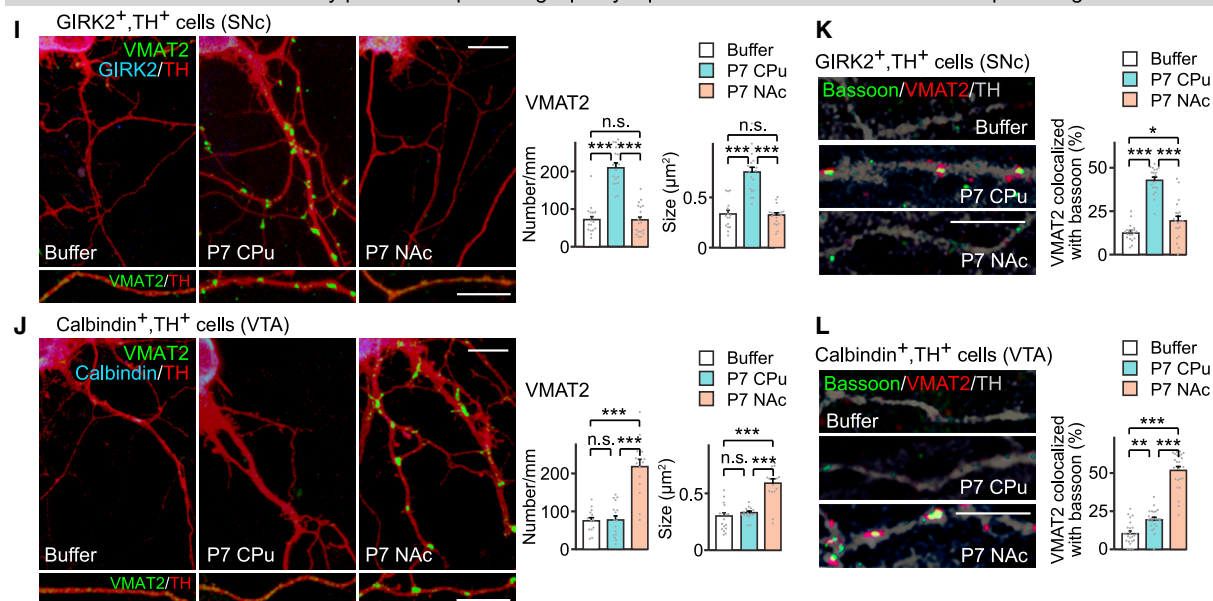
## Postnatal striatal extracts contain dopaminergic presynaptic organizing activity



## GIRK2 and calbindin are specific markers for SNc and VTA dopaminergic neurons, respectively



## CPu and NAc extracts selectively promote dopaminergic presynaptic differentiation in SNc or VTA dopaminergic neurons



(legend on next page)

in the nigrostriatal or mesolimbic pathway. Smad1 mutant mice show motor defects, and Smad2 mutant mice show lack of motivation, underscoring the importance of Smad1 and Smad2 signaling in establishing functional synapses that underlie relevant behaviors for the respective pathways. Together, our results uncover the molecular logic being utilized to establish parallel but functionally discrete dopaminergic pathways.

## RESULTS

### Identification and characterization of pathway-specific dopaminergic presynaptic organizing activity

We first determined when dopaminergic synaptic connections in the striatum are established during development (Figures 1A–1C). A hallmark feature of synaptic development is the accumulation of synaptic vesicles (SVs) at nerve terminals. Therefore, we examined the accumulation of dopaminergic SVs in the striatum during rat brain development. We monitored dopaminergic SV accumulation by immunostaining for vesicular monoamine transporter-2 (VMAT2), which transports dopamine into SVs. VMAT2 began to accumulate in the striatum at P4 (Figures 1A and 1B). The number of VMAT2 puncta dramatically increased from P7 to P10, then mildly increased until P21, and plateaued. The size of the VMAT2 puncta increased continuously from P4 to P21 and then plateaued. We next assessed dopaminergic axons. We found that dopaminergic axons, visualized by immunostaining for tyrosine hydroxylase (TH), were already present in the striatum at P0 and significantly increased until P7, which may include axon branching, followed by a plateau (Figures 1A and 1C). These results suggest that midbrain dopaminergic (mDA) axons in the striatum develop by P7, and as they develop, the axons differentiate into dopaminergic presynaptic terminals, with the peak of dopaminergic presynaptic differentiation occurring between P4 and P10.

We reasoned that the P4–P10 striatum should highly express factors that induce dopaminergic presynaptic differentiation of mDA neurons. As dopaminergic presynaptic terminals may not be tightly associated with postsynaptic sites,<sup>9–11</sup> we hypothesized that these factors might be soluble. To test this idea, we cultured rat midbrain neurons, treated them with striatal extracts

(soluble fractions) prepared from P4, P7, or P10 rats, and examined dopaminergic presynaptic differentiation by assessing VMAT2 clustering in TH-positive mDA neurons (Figure 1D). We found that treatment with the P7 striatal extract most effectively increased the density and size of VMAT2 puncta in mDA neurons. The P4 extract also increased VMAT2 accumulation but to a lesser extent than the P7 extract. The P10 extract only increased the size of VMAT2 puncta. These results indicate that the striatum expresses dopaminergic presynaptic organizing molecules and that their activity is high between P4 and P10 with its peak at ~P7, consistent with the peak of dopaminergic presynaptic differentiation *in vivo* (Figures 1A and 1B). Extracts prepared from non-target regions, cerebellum and thalamus, did not increase VMAT2 accumulation (Figure 1E). The morphology of cultured mDA neurons was not apparently changed by any of the extract treatments (Figures S1A and S1B). These results indicate that dopaminergic presynaptic organizers are selectively expressed by the postnatal striatum. We then characterized the active factors in the P7 striatal extract. We biochemically fractionated the extract based on molecular size. We found that the fraction containing 10–30 kDa proteins, but not <10 kDa or >30 kDa proteins, efficiently increased the accumulation of VMAT2 in cultured mDA neurons (Figure 1F). Altogether, these results reveal that the dopaminergic presynaptic organizers for mDA neurons are soluble proteins expressed by the striatum, with expression peaking at ~P7 and molecular sizes between 10 and 30 kDa.

We next tested the idea that the appropriate targets of nigrostriatal and mesolimbic pathways, the CPU and NAc, respectively, express distinct molecules that selectively promote the presynaptic development of each pathway. Nigrostriatal dopaminergic neurons are located in the SNc and express G-protein-regulated inward-rectifier potassium channel 2 (GIRK2), whereas mesolimbic dopaminergic neurons are situated in the VTA and express calbindin (Figure 1G: GIRK2 and calbindin show little overlap in mDA neurons).<sup>12,13</sup> Using cultured mDA neurons, we examined whether the CPU or NAc provides specific molecules that promote selective development of dopaminergic presynaptic terminals of SNc (GIRK2-positive) or VTA (calbindin-positive) dopaminergic neurons, respectively (see Figure 1H). Our midbrain

### Figure 1. Identification and characterization of pathway-specific dopaminergic presynaptic organizing activity in the striatum

(A–C) Time course of dopaminergic synapse development in the rat striatum. Presynaptic differentiation and targeting of dopaminergic axons were monitored by VMAT2 and TH immunostaining, respectively. (A) Representative images. Scale bar, 50  $\mu$ m. (B) Quantification of the density and size of VMAT2 puncta. (C) Quantification of TH immunoreactivity (relative to P0). n (fields; rats) = 5–45; 3–10 (B) and 5–11; 3–7 (C).

(D–F) Characterization of dopaminergic presynaptic organizing activity. Cultured midbrain neurons were treated with each extract at 4 DIV (days *in vitro*) and stained at 6 DIV for TH and VMAT2. (D) Age-dependent effects of striatal extracts on dopaminergic presynaptic differentiation. (E) Dopaminergic presynaptic organizing activity is specific to the striatal extract. (F) The molecular size of the dopaminergic presynaptic organizers is 10–30 kDa. Scale bars, 10  $\mu$ m. n (cells; independent experiments) = 20–39; 6–7 (D), 29–39; 7–8 (E), 13–16; 3 (F), one-way ANOVA with Tukey's test.

(G) GIRK2 and calbindin are markers for SNc or VTA dopaminergic neurons. P14 mouse coronal sections were immunostained for GIRK2, calbindin, and TH. Dashed line: midline; IPN, interpeduncular nucleus. Scale bar, 500  $\mu$ m. n (sections; mice) = 8; 4.

(H) Illustration of the nigrostriatal (SNc to CPU) and mesolimbic (VTA to NAc) dopaminergic pathways. We hypothesize that CPU and NAc provide specific molecules that promote dopaminergic presynaptic differentiation in SNc and VTA mDA neurons, respectively.

(I and J) CPU and NAc extracts selectively promote VMAT2 clustering in SNc or VTA dopaminergic neurons, respectively. Midbrain cultures were treated at 4 DIV with the extract and stained at 6 DIV. Scale bars, 10  $\mu$ m. n (cells; independent experiments) = 16–18; 4 (I), 16–18; 5 (J), one-way ANOVA with Tukey's test.

(K and L) CPU and NAc extracts preferentially promote bassoon clustering at dopaminergic presynaptic terminals in SNc or VTA dopaminergic neurons, respectively. Scale bars, 10  $\mu$ m. n (cells; independent experiments) = 20; 4 (K), 24; 3–4 (L), one-way ANOVA with Tukey's test.

Data are represented as mean  $\pm$  SEM.

See also Figure S1.



**Table 1. List of genes, which encode soluble, 10–30 kDa molecules, that are differentially expressed between P7 CPu vs. NAc (>2-fold difference)**

Symbol	Definition	Fold
<b>CPu/NAc</b>		
<i>Bmp6</i>	bone morphogenetic protein 6	2.35
<i>Tgfa</i>	transforming growth factor alpha	2.15
<i>Bmp2</i>	bone morphogenetic protein 2	2.04
<b>NAc/CPu</b>		
<i>Nrn1</i>	neurtin 1	9.26
<i>C1q/3</i>	complement component 1, q subcomponent-like 3	5.06
<i>Nxph3</i>	neurexophilin 3	2.69
<i>Tgfb2</i>	transforming growth factor beta 2	2.65
<i>Ocm</i>	oncomodulin	2.31
<i>Igf1</i>	insulin-like growth factor 1	2.14
<i>Bmp3</i>	bone morphogenetic protein 3	2.02

TGF- $\beta$  superfamily proteins were identified as candidates for pathway-specific dopaminergic presynaptic organizers. For a full list of differentially expressed genes, see [Tables S1](#) (CPu > NAc) and [S2](#) (NAc > CPu).

cultures contain similar numbers of SNc and VTA dopaminergic neurons. 48-h treatment of cultured midbrain neurons with the CPu or NAc extract prepared from P7 rat striata ([Figure S1C](#)) significantly induced VMAT2 clustering in mDA neurons ([Figure S1D](#)). Notably, we found that the CPu extract, but not the NAc extract, increased the density and size of VMAT2 puncta in SNc dopaminergic neurons ([Figure 1I](#)). By contrast, the NAc extract, but not the CPu extract, increased the density and size of VMAT2 puncta in VTA dopaminergic neurons ([Figure 1J](#)). We next examined whether active zone formation in mDA neurons is also induced by target-derived factors in a pathway-specific manner by evaluating the clustering of bassoon, an active zone protein, at VMAT2-positive dopaminergic presynaptic terminals. We found that the CPu extract preferentially promoted active zone formation in SNc dopaminergic neurons ([Figure 1K](#)), whereas the NAc extract affected VTA dopaminergic neurons ([Figure 1L](#)). Together, these results demonstrate that the CPu and NAc provide specific dopaminergic presynaptic organizing factors for the nigrostriatal (SNc) or mesolimbic (VTA) dopaminergic neurons, respectively.

### **BMP6/BMP2 and TGF- $\beta$ 2 are nigrostriatal or mesolimbic pathway-specific dopaminergic synaptic organizers**

We performed a microarray screen to identify candidate molecules for pathway-specific dopaminergic presynaptic organizers. We prepared RNA from the P7 rat CPu and NAc ([Figure S1C](#)) and identified genes that are differentially expressed between CPu vs. NAc, focusing on soluble molecules that are 10–30 kDa in size ([Tables 1](#), [S1](#), and [S2](#)). In the CPu, we identified three genes that are substantially more abundant (>2-fold difference) relative to the NAc: *Bmp6*, *Tgfa*, and *Bmp2*. Two of them, *Bmp6* and *Bmp2* encode the TGF- $\beta$  superfamily proteins, BMP6 and BMP2, respectively. Interestingly, in the NAc, we identified *Tgfb2*, which encodes another TGF- $\beta$  superfamily member TGF- $\beta$ 2, as a differentially expressed gene relative to the CPu.

BMPs bind BMPR and TGF- $\beta$ s bind TGF- $\beta$ R, and each receptor then activates distinct Smad signaling/transcription factors.<sup>14–16</sup>

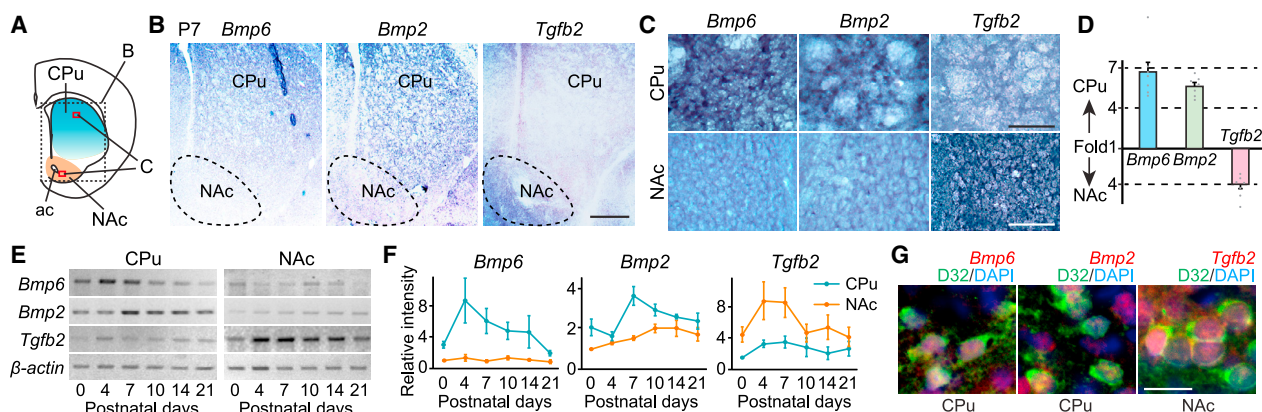
What is intriguing is that BMP6/BMP2 and TGF- $\beta$ 2 signaling are known to antagonize each other at the level of Smad complexes, by competing for the common Smad, Smad4, and through the upregulation of Smad inhibitors.<sup>16</sup> Therefore, BMP6/BMP2 and TGF- $\beta$ 2 are attractive candidates as pathway-specific dopaminergic presynaptic organizers; thus, we decided to focus on these TGF- $\beta$  family proteins in this study. In *Drosophila*, Smads have been shown to regulate neuromuscular synaptic growth<sup>17,18</sup>; however, the roles of BMP/TGF- $\beta$  and Smads in dopaminergic synapse formation in the mammalian brain are not known.

*In situ* hybridization experiments confirmed that the expressions of *Bmp6* and *Bmp2* mRNAs were much higher in the CPu than in the NAc of P7 rats ([Figures 2A–2D](#)). By contrast, the expression of *Tgfb2* mRNA was substantially higher in the NAc than in the CPu. We then examined their developmental expression by RT-PCR. *Bmp6*, *Bmp2*, and *Tgfb2* mRNA showed relatively low expression levels in the non-enriched region of striatum ([Figures 2E and 2F](#)). On the other hand, the levels of *Bmp6* and *Bmp2* mRNA in the CPu, and *Tgfb2* mRNA in the NAc, significantly increased during dopaminergic synapse formation, peaking at P4–P7 ([Figures 2E and 2F](#)), which is consistent with the age-dependent dopaminergic presynaptic organizing activity of the striatal extracts ([Figure 1D](#)). The majority of *Bmp6*, *Bmp2*, and *Tgfb2* mRNA-expressing cells were immuno-positive for DARPP32, a marker of medium spiny neurons (MSNs) (82.44%  $\pm$  2.13%, 76.53%  $\pm$  2.06%, and 74.08%  $\pm$  4.03%, respectively; [Figure 2G](#)). These results indicate that BMP6 and BMP2 are highly and preferentially expressed by MSNs in the CPu, whereas TGF- $\beta$ 2 is highly and preferentially expressed by MSNs in the NAc during dopaminergic synapse formation.

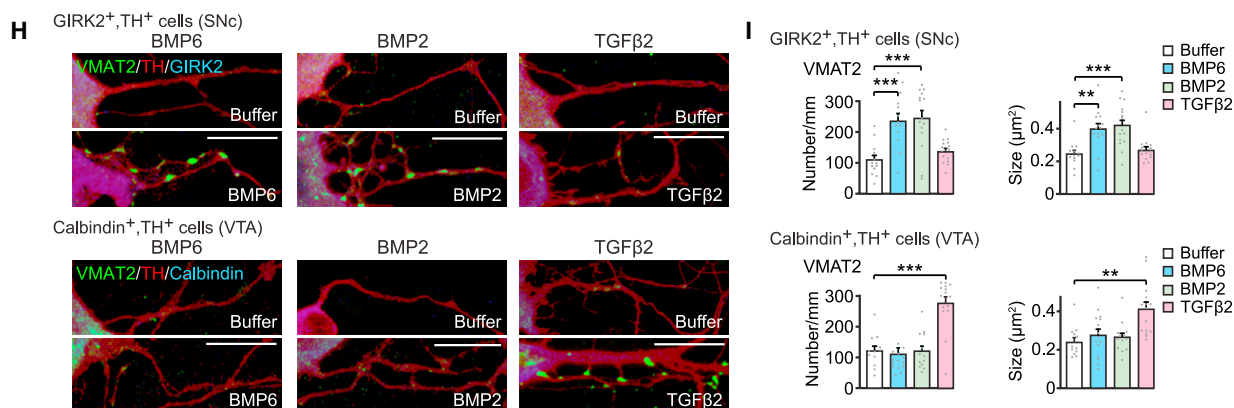
We next investigated whether BMP6, BMP2, and TGF- $\beta$ 2 can induce dopaminergic presynaptic differentiation in mDA neurons using cultured midbrain neurons. We found that BMP6 or BMP2 (10 ng/mL) or TGF- $\beta$ 2 (2 ng/mL) increased the number of mDA neurons with VMAT2 puncta, without affecting the total number of mDA neurons ([Figure S1E](#)). BMP6, BMP2, or TGF- $\beta$ 2 at these concentrations did not alter the proportion of SNc and VTA dopaminergic neurons ([Figures S1F and S1G](#)) and did not apparently affect the overall morphology and neurite elongation of SNc and VTA dopaminergic neurons ([Figures S1H and S1I](#)). Thus, BMP6, BMP2, and TGF- $\beta$ 2 have a specialized ability to induce dopaminergic presynaptic differentiation rather than more general neuronal differentiation. We then examined whether BMP6, BMP2, and TGF- $\beta$ 2 are pathway-specific dopaminergic presynaptic organizers. We found that BMP6 or BMP2 increased VMAT2 accumulation in SNc, but not VTA, dopaminergic neurons ([Figures 2H and 2I](#)). By contrast, TGF- $\beta$ 2 treatment increased VMAT2 accumulation in VTA, but not SNc, dopaminergic neurons ([Figures 2H and 2I](#)). These results suggest that BMP6/BMP2 and TGF- $\beta$ 2 are nigrostriatal and mesolimbic pathway-specific dopaminergic presynaptic organizers, respectively.

Why are there two BMPs for the nigrostriatal pathway? BMPs can form and signal as either homodimers or heterodimers. A

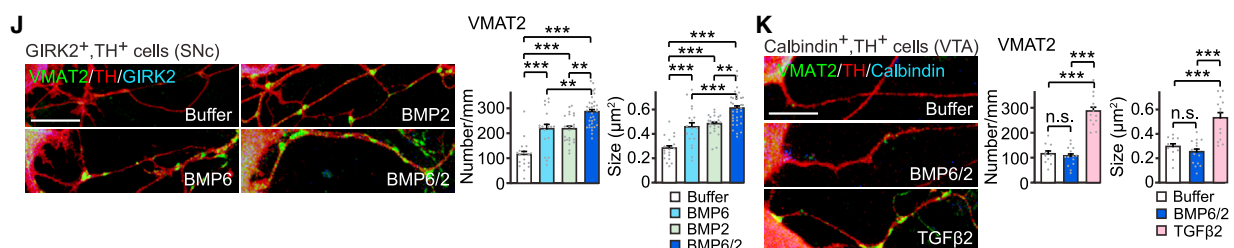
*Bmp6/Bmp2* and *Tgfb2* are preferentially expressed in the CPu or NAc during dopaminergic synapse development



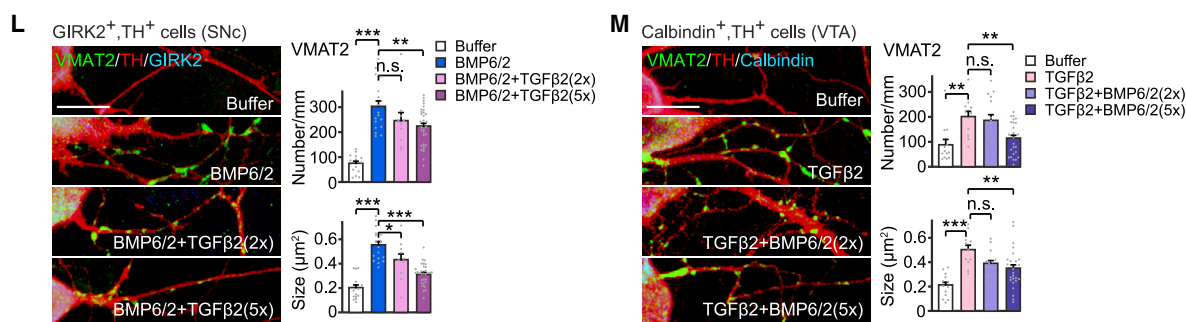
BMP6/BMP2 and TGF $\beta$ 2 selectively induce dopaminergic presynaptic differentiation in SNc or VTA dopaminergic neurons



BMP6/2 heterodimers have stronger synaptogenic effects than BMP6 or BMP2 homodimers



BMP6/2 and TGF $\beta$ 2 pathways antagonize each other in dopaminergic neurons



(legend on next page)

BMP6/2 heterodimer appears to have stronger signaling activity than either of the homodimers alone.<sup>19–21</sup> Hence, we tested the effects of the BMP6 homodimer, BMP2 homodimer, and BMP6/2 heterodimer on dopaminergic presynaptic differentiation in cultured mDA neurons. We found that indeed, BMP6/2 heterodimers show significantly stronger effects on VMAT2 clustering in SNc mDA neurons than either of the homodimers (Figure 2J). BMP6/2 did not have any effects on VTA mDA neurons (Figure 2K). These results suggest that BMP6 and BMP2 may exist as heterodimers to amplify their effects.

We next tested whether cross-inhibition between BMP6/2 and TGF- $\beta$ 2 signaling occurs in dopaminergic presynaptic differentiation. We found that the effects of BMP6/2 on dopaminergic presynaptic differentiation in SNc mDA neurons were suppressed by TGF- $\beta$ 2 in a dose-dependent manner (Figure 2L). Conversely, the effects of TGF- $\beta$ 2 on dopaminergic presynaptic differentiation in VTA mDA neurons were dose-dependently suppressed by BMP6/2 (Figure 2M). These results suggest that the BMP6/2 and TGF- $\beta$ 2 signaling pathways indeed antagonize each other in dopaminergic presynaptic differentiation.

We then asked whether BMP6, BMP2, and TGF- $\beta$ 2 are required for dopaminergic presynaptic differentiation *in vivo* in a pathway-specific manner. We silenced BMP6, BMP2, or TGF- $\beta$ 2 in the CPu and NAc in rats by short hairpin RNA (shRNA)-mediated knockdown (Figures 3A and 3D) and analyzed VMAT2 accumulation. In the CPu, the number and size of VMAT2 puncta were significantly decreased in the areas where BMP6 or BMP2 was knocked down relative to controls (Figures 3B and 3C). However, TGF- $\beta$ 2 knockdown did not affect VMAT2 accumulation in the CPu. Conversely, in the NAc, TGF- $\beta$ 2 knockdown resulted in a significant decrease in the number and size of VMAT2 puncta relative to controls (Figures 3E and 3F). No change in VMAT2 accumulation was observed when BMP6 or BMP2 was knocked down in the NAc. shRNA-mediated BMP6, BMP2, or TGF- $\beta$ 2 silencing did not change the intensity of TH immunostaining in either the CPu or NAc (Figures 3G and 3H), indicating that dopaminergic axons did reach the CPu and NAc. To further confirm our results, we performed rescue experiments by expressing shRNA-resistant BMP6, BMP2, or TGF- $\beta$ 2 together with shRNA. We found that the decreases in the VMAT2 density and size induced by *Bmp6*-shRNA in the CPu, *Bmp2*-shRNA in the CPu, and *Tgfb2*-shRNA in the NAc were

all completely rescued by the re-expression of BMP6, BMP2, and TGF- $\beta$ 2, respectively (Figure 3I). These results exclude the off-target effects of shRNA-mediated knockdown. Together, these results indicate that target-derived BMP6, BMP2, and TGF- $\beta$ 2 are necessary for dopaminergic presynaptic differentiation *in vivo*: BMP6 and BMP2 for the nigrostriatal pathway and TGF- $\beta$ 2 for the mesolimbic pathway. Interestingly, when we ectopically overexpressed BMP6, BMP2, or TGF- $\beta$ 2 in a region of low expression (i.e., TGF- $\beta$ 2 in the CPu where BMP6/BMP2 are abundant, or BMP6/BMP2 in the NAc where TGF- $\beta$ 2 is abundant), they decreased the density or size of VMAT2 puncta (Figure 3J). These results support the notion that BMP6/BMP2 and TGF- $\beta$ 2 can antagonize each other *in vivo*.

MSNs receive not only dopaminergic inputs but also glutamatergic and GABAergic inputs.<sup>22</sup> We next examined the effect of BMP6-, BMP2-, and TGF- $\beta$ 2-knockdown on glutamatergic and GABAergic presynaptic differentiation in the striatum. We did not find any significant differences in VGLUT1 (vesicular glutamate transporter 1; which labels corticostriatal glutamatergic synapses), VGLUT2 (vesicular glutamate transporter 2; thalamostriatal glutamatergic synapses), or VGAT (vesicular GABA transporter; GABAergic synapses) clustering between knockdown and control areas (Figure S2). These results indicate that BMP6, BMP2, and TGF- $\beta$ 2 are specifically required for dopaminergic presynaptic differentiation. Altogether, our results identify BMP6/BMP2 and TGF- $\beta$ 2 as pathway-specific dopaminergic presynaptic organizers *in vivo*.

### Differentially expressed BMPR and TGF- $\beta$ R mediate dopaminergic presynaptic differentiation of SNc and VTA mDA neurons through the activation of distinct Smads

We next sought the receptors that mediate dopaminergic presynaptic differentiation. Because BMP6/BMP2 and TGF- $\beta$ 2 bind distinct receptors, BMPR or TGF- $\beta$ R,<sup>14–16</sup> we first asked whether SNc and VTA dopaminergic neurons express BMPR and/or TGF- $\beta$ R. Immunostaining of cultured mDA neurons revealed that SNc dopaminergic neurons preferentially express BMPR (Figure 4A), and VTA dopaminergic neurons preferentially express TGF- $\beta$ R (Figure 4B). BMPR and TGF- $\beta$ R localize to nigrostriatal or mesolimbic axons (Figures 4C and 4D). In the midbrain, the expression of BMPR is significantly higher in the SNc than VTA, and that of

### Figure 2. BMP6/BMP2 and TGF- $\beta$ 2 are nigrostriatal or mesolimbic pathway-specific dopaminergic synaptic organizers, respectively

(A–G) *Bmp6/Bmp2* and *Tgfb2* are preferentially expressed by MSNs in CPu or NAc during dopaminergic synapse development. (A) Schematic illustration of rat striatum. ac, anterior commissure. Representative images in (B) and (C) were from the dotted-boxed area and the red-boxed areas. (B–D) *In situ* hybridization. (D) Quantification of the relative intensity (CPu vs. NAc; fold difference) of the signals. n (sections; rats) = 7; 4–5. Scale bars, 500  $\mu$ m (B), 100  $\mu$ m (C). (E and F) RT-PCR. The mRNA level from each age was normalized to that of P0 NAc (*Bmp6* and *Bmp2*) or P0 CPu (*Tgfb2*). n (independent experiments; rats) = 3–5; 3. (G) *Bmp6*, *Bmp2*, and *Tgfb2* fluorescence *in situ* hybridization followed by DARPP32 immunostaining. Scale bar, 20  $\mu$ m. Observations (sections; rats) = 8–9; 3–4. (H and I) BMP6/BMP2 and TGF- $\beta$ 2 selectively induce VMAT2 clustering in SNc or VTA dopaminergic neurons, respectively. Midbrain cultures were treated with recombinant BMP6, BMP2, or TGF- $\beta$ 2 protein at 3 DIV and stained at 7 DIV. Scale bars, 10  $\mu$ m. n (cells; independent experiments) = 12–15; 3–5, one-way ANOVA with Tukey's test.

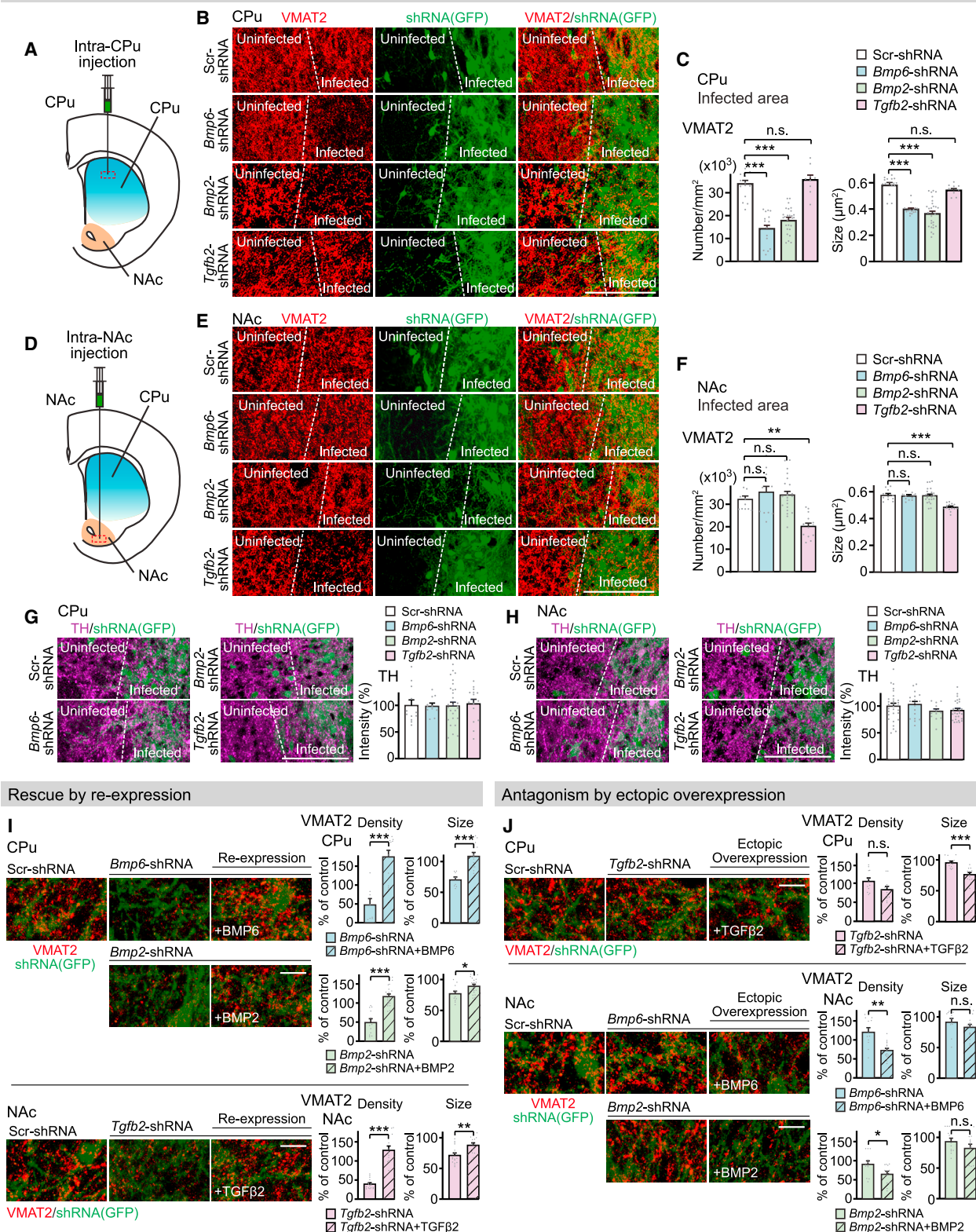
(J and K) BMP6/2 heterodimers more strongly induce VMAT2 clustering in SNc mDA neurons than BMP6 or BMP2 homodimers (J). BMP6/2 heterodimers do not show effects in VTA mDA neurons (K). Scale bars, 10  $\mu$ m. n (cells; independent experiments) = 18–33; 3–6 (J), 10–14; 2 (K), one-way ANOVA with Tukey's test. (L and M) BMP6/2 and TGF- $\beta$ 2 antagonize each other in mDA neurons. The effect of BMP6/2 heterodimers in SNc neurons is suppressed by TGF- $\beta$ 2 (L). The effect of TGF- $\beta$ 2 in VTA neurons is suppressed by BMP6/2 (M). Scale bars, 10  $\mu$ m. n (cells; independent experiments) = 10–31; 2–3 (L), 11–25; 3 (M), one-way ANOVA with Tukey's test.

Data are represented as mean  $\pm$  SEM.

See also Figure S1.



*In vivo* knockdown of BMP6, BMP2, or TGFβ2 impairs dopaminergic presynaptic differentiation in a pathway-specific manner



(legend on next page)



TGF- $\beta$ R is significantly higher in the VTA than SNc dopaminergic neurons (Figures 4E–4G). These results indicate that BMPR and TGF- $\beta$ R are preferentially expressed in the SNc or VTA dopaminergic neurons, respectively, suggesting that pathway-preferential localizations of these receptors contribute to specific dopaminergic presynaptic differentiation. To test this, we inhibited the activity of BMPR and TGF- $\beta$ R. We treated cultured mDA neurons with well-characterized BMPR and TGF- $\beta$ R inhibitors, LDN193189 and SB525334.<sup>23,24</sup> In SNc dopaminergic neurons, the CPu extract-induced VMAT2 clustering was completely blocked by the BMPR inhibitor but not by the TGF- $\beta$ R inhibitor (Figure 4H). By contrast, in VTA dopaminergic neurons, the NAc extract-induced VMAT2 clustering was completely blocked by the TGF- $\beta$ R inhibitor but not by the BMPR inhibitor (Figure 4I). These results demonstrate that BMPR and TGF- $\beta$ R specifically mediate the dopaminergic presynaptic differentiation of SNc and VTA neurons, respectively.

In the canonical signaling pathways, BMP6/BMP2 bind BMPR and activate (phosphorylate) Smad1/5/8, whereas TGF- $\beta$ 2 binds TGF- $\beta$ R and activates Smad2/3.<sup>14–16</sup> We next examined whether any Smads are activated by BMP6, BMP2, and TGF- $\beta$ 2 in mDA neurons. Based on the Allen brain atlas, Smad1 and Smad2, but not other Smads, are highly expressed in the midbrain. Therefore, we focused on Smad1 and Smad2. We found that BMP6 or BMP2, but not TGF- $\beta$ 2, treatment induced Smad1 activation in SNc dopaminergic neurons (Figures 4J and 4L). None of these factors induced Smad2 activation in SNc dopaminergic neurons (Figure 4J). By contrast, in VTA dopaminergic neurons, TGF- $\beta$ 2, but not BMP6 or BMP2, treatment induced Smad2 activation (Figures 4K and 4M). No factors induced Smad1 activation in VTA dopaminergic neurons (Figure 4K). These results indicate that BMP6/BMP2 and TGF- $\beta$ 2 activate distinct Smads, selectively in SNc or VTA dopaminergic neurons. We next examined the developmental time course of Smad activation in the midbrain *in vivo*. We found that the expression of phospho-Smad1 is highest at P4 and P7 in the SNc, whereas it did not change in the VTA (Figure 4N). By contrast, the expression of phospho-Smad2 is highest at P7 in the VTA, but no change was detected in the SNc (Figure 4O). These results indicate that the time courses of the activation of Smad1 and Smad2 are correlated with the time courses of BMP6/BMP2 and TGF- $\beta$ 2 expression in the striatum (Figures 2E and 2F). Additionally, we found that the expressions of phospho-Smad in the striatum and midbrain are correlated during development (Figures 4N–4Q), consistent with the notion that activated Smad is retro-

gradely transported from the striatum (synapse) to the midbrain (nucleus).<sup>25,26</sup>

### Smad1 specifically regulates nigrostriatal dopaminergic synapse formation, whereas Smad2 regulates mesolimbic dopaminergic synapse formation, *in vivo*

Next, we asked whether Smad1 and Smad2 regulate dopaminergic presynaptic differentiation *in vivo* in a pathway-specific manner. For specific inactivation of Smads in dopaminergic neurons during the time of synapse formation, we mated *Smad1<sup>flox/flox</sup>* and *Smad2<sup>flox/flox</sup>* mice<sup>27,28</sup> with *DAT-CreER* mice (tamoxifen-dependent Cre under the dopamine transporter [DAT] promoter) to generate *Smad1<sup>flox/flox</sup>::DAT-CreER* and *Smad2<sup>flox/flox</sup>::DAT-CreER* mice. We then injected tamoxifen at P1 to conditionally knockout (cKO) each Smad postnatally, resulting in *Smad1*cKO and *Smad2*cKO mice. We used *Smad<sup>wt/wt</sup>::DAT-CreER* mice injected with tamoxifen as control mice. Specific inactivation of *Smad1* or *Smad2* in mDA neurons in the cKO mice was confirmed by *in situ* hybridization (Figures S3A and S3B).

We first performed immunostaining for VMAT2 to assess dopaminergic presynaptic differentiation in the CPu and NAc at P14. In *Smad1*cKO mice, VMAT2 accumulation was significantly decreased in the CPu but not in the NAc (Figures 5A–5C). The decrease was more significant in the dorsal CPu than ventral CPu (Figures S3C and S3D), consistent with the gradient expression pattern of BMPs in the CPu (Figure 2B). By contrast, in *Smad2*cKO mice, VMAT2 accumulation was decreased in the NAc, but not in the CPu (Figures 5D–5F). These specific defects in VMAT2 accumulation were still observed in adult *Smad*cKO mice (Figures S3E–S3J). Thus, Smad1 and Smad2 appear to play critical roles in dopaminergic presynaptic differentiation of the nigrostriatal or mesolimbic dopaminergic pathway, respectively.

To ask whether Smads regulate dopaminergic presynaptic differentiation by direct or indirect means, we performed a series of control experiments. (1) We examined the numbers of mDA neurons in *Smad*cKO mice. There was no change in the numbers of SNc and VTA mDA neurons in these mice relative to control mice (Figures S4A–S4D). (2) We assessed the projection of mDA axons to the striatum. First, we found that inactivation of either Smad did not affect the intensity of TH staining in the CPu or NAc (Figures 5G, 5H, and S3K), suggesting that dopaminergic axons reached the striatum in *Smad*cKO mice. Second, we traced dopaminergic axons from the SNc and VTA in *Smad*cKO mice. We found that dopaminergic axon targeting is normal in

### Figure 3. *In vivo* knockdown of BMP6, BMP2, or TGF- $\beta$ 2 impairs dopaminergic presynaptic differentiation in the striatum in a pathway-specific manner

(A–H) Lentivirus expressing GFP together with *Bmp6*-shRNA, *Bmp2*-shRNA, *Tgfb2*-shRNA, or scrambled (Scr)-shRNA was injected into rat CPu (A) or NAc (D) at P3. Striatal sections were stained for VMAT2 (B and E) and TH (G and H) at P12. The rectangles in (A) and (D) approximately show the areas shown in (B and G) and (E and H), respectively. (C and F) The density and size of VMAT2 puncta in virus-infected area. (G and H) The intensities of TH immunostaining (relative to Scr-shRNA) in the virus-infected area. Scale bars, 100  $\mu$ m. n (fields; rats) = 9–27; 3–7 (C), 11–21; 4–5. (F), 11–30; 2–5 (G), 12–30; 2–4 (H), one-way ANOVA with Tukey's test.

(I) The decreases in the VMAT2 density and size induced by *Bmp6*-shRNA in CPu, *Bmp2*-shRNA in CPu, and *Tgfb2*-shRNA in NAc were rescued by the re-expression of BMP6, BMP2, and TGF- $\beta$ 2, respectively. Scale bars, 10  $\mu$ m. n (fields; rats) = 8–19; 2–5, Student's t test.

(J) Ectopic overexpression of TGF- $\beta$ 2 in CPu, and BMP6 or BMP2 in NAc, decreased the density or size of VMAT2 puncta. Scale bars, 10  $\mu$ m. n (fields; rats) = 11–16; 3, Student's t test.

Data are represented as mean  $\pm$  SEM.

See also Figure S2.

**A** SNc **B** VTA

BMPR/TH GIRK2 TGFβR/TH GIRK2

BMPR/TH Calbindin TGFβR/TH Calbindin

**C** Nigrostriatal Mesolimbic

BMPR/TH/Calbindin

**D** Nigrostriatal Mesolimbic

TGFβR/TH/Calbindin

**E** SNc VTA

BMPR/TH TGFβR/TH

**F** SNc VTA

BMPR/TH TGFβR/TH

**G** BMPR TGFβR

Intensity (% VTA)

Intensity (% SNc)

\*\*\*

\*\*\*

■ SNc ■ VTA

**H** **SNc** **VMAT2/TH/GIRK2**

Buffer  
P7CPu  
P7CPu+BMPRinh  
P7CPu+TβRinh

VMAT2 Number/mm  
Size (μm<sup>2</sup>)

n.s.  
\*\*\*  
\*\*\*  
\*\*\*  
n.s.  
n.s.  
\*\*\*  
\*\*

□ Buffer  
■ P7 CPu  
■ P7 CPu+BMPRinh  
■ P7 CPu+TβRinh

**I** **VTA** **VMAT2/TH/Calbindin**

Buffer  
P7NAc  
P7NAc+BMPRinh  
P7NAc+TβRinh

VMAT2 Number/mm  
Size (μm<sup>2</sup>)

n.s.  
\*\*\*  
n.s.  
n.s.  
\*\*\*  
n.s.  
\*\*\*  
n.s.

□ Buffer  
■ P7 NAc  
■ P7 NAc+BMPRinh  
■ P7 NAc+TβRinh

**J** SNC Treatment: Control, BMP6, BMP2, TGF $\beta$ 2

**K** VTA Treatment: Control, BMP6, BMP2, TGF $\beta$ 2

**L** pSmad1 positive cells in SNC (GIRK2<sup>+</sup>, TH<sup>+</sup>) cells

Treatment	% of SNC cells
Buffer	~15
BMP6	~75
BMP2	~70
TGF $\beta$ 2	~10

**M** pSmad2 positive cells in VTA (Calbindin<sup>+</sup>, TH<sup>+</sup>) cells

Treatment	% of VTA cells
Buffer	~15
BMP6	~25
BMP2	~15
TGF $\beta$ 2	~75

**N** Midbrain  
P0 P4 P7 P10 P21

SNc  
VTA

pSmad1/TH

**P** Striatum CPu  
pSmad1 on TH  
P0 P7  
Number/mm<sup>2</sup> (x10<sup>3</sup>) \*\*

**O** P0 P4 P7 P10 P21  
SNc  
VTA  
pSmad2/TH

**Q** Striatum NAc  
pSmad2 on TH  
P0 P7  
Number/mm<sup>2</sup> (x10<sup>3</sup>) \*\*

**R** Striatum CPu  
pSmad1 on TH  
P0 P7  
Number/mm<sup>2</sup> (x10<sup>3</sup>) \*\*

Cell 186, 3845–3861, August 31, 2023 3853

SmadCKO mice (Figures 5I–5L). (3) We examined the development of dendrites from mDA neurons in the SNr by immunostaining and found no defect in dendritic development in either SmadCKO mice (Figures S4E–S4I). (4) We evaluated the glutamatergic and GABAergic synapses formed onto mDA neurons in the SNr by immunostaining and found no change in SmadCKO mice (Figures S4J–S4O). (5) We assessed dopaminergic postsynaptic development by immunostaining for dopamine receptors, D1R and D2R, in the striatum of SmadCKO mice. We found no change in the intensity of D1R and D2R puncta (Figure S5). These results suggest that postnatal inactivation of Smads in mDA neurons does not affect the survival, axon targeting, and dendritic development of mDA neurons, glutamatergic and GABAergic synaptic input formed onto them, and dopaminergic postsynaptic differentiation in the striatum. Together, these results support the idea that Smad1 and Smad2 are specifically necessary for dopaminergic presynaptic differentiation.

We next performed electron microscopy (EM). To specifically identify dopaminergic presynaptic terminals in the striatum, we performed EM with dAPEX2 (dimeric enhanced ascorbate peroxidase)-based synaptic labeling (Figure S6).<sup>29</sup> We expressed mitochondrial matrix-targeted dAPEX2 (Matrix-dAPEX2) in mDA neurons of *Smad*CKO mice, and the mice were subjected to EM analysis at P32. After diaminobenzidine staining (Figure S6B), Matrix-dAPEX2 serves as an EM marker for mitochondria in mDA neurons (Figure S6C). The majority of mitochondria accumulates at presynaptic terminals (in control mice,  $81.0\% \pm 0.98\%$  of dAPEX2-labeled mitochondria are associated with SVs), and thus, presynaptic terminals from mDA neurons can be identified in the striatum by EM (Figures S6C and S6D). Using this method, we found that relative to control mice, *Smad1*CKO mice have significantly fewer SVs in dopaminergic presynaptic terminals in the CPU but equivalent numbers in the NAc (Figures 5M and 5O). By contrast, *Smad2*CKO mice have significantly fewer SVs in dopaminergic presynaptic terminals in the NAc, but not in the CPU (Figures 5N and 5P). The density of dAPEX2-labeled mitochondria in the striatum and the density and size of dopaminergic presynaptic terminals with labeled mitochondria were similar between *Smad*CKO and control mice (Figures S6E–S6G). These EM studies confirm that *Smad1* and *Smad2* are specifically required for the accumulation of SVs at dopaminergic presynaptic terminals in the CPU or NAc, respectively.

We next examined the physiological consequences of dopaminergic presynaptic defects in SmadCKO mice. We measured extracellular dopamine release *in vivo* in the CPU and NAc using fiber photometry with a genetically encoded fluorescent sensor for dopamine, GRAB<sub>DA</sub>.<sup>30</sup> We virally expressed GRAB<sub>DA</sub> in the CPU or NAc of SmadCKO mice and recorded fluorescent changes in response to amphetamine, a psychostimulant that increases dopamine transmission (Figures 5Q and 5R). In control mice, amphetamine injections induced a clear dopamine release (increase in  $\Delta F/F$ ) both in the CPU and NAc (Figures 5S and 5T). Smad1cKO mice showed a significant decrease in dopamine release in the CPU, but not in the NAc, relative to control mice (Figures 5S and 5U), whereas Smad2cKO mice showed a significant decrease in dopamine release in the NAc, but not in the CPU (Figures 5T and 5V). These results indicate that dopamine release is specifically impaired in the CPU of Smad1cKO and in the NAc of Smad2cKO mice. Finally, we examined action potential-dependent dopamine release in SmadCKO and control mice. We performed GRAB<sub>DA</sub> imaging in striatal slices to examine dopamine release in response to electrical stimulation.<sup>31</sup> We found that the level ( $\Delta F/F_0$ ) and extent (area) of dopamine release in Smad1cKO mice are significantly decreased relative to control mice in the CPU (Figures 5W–5Z). By contrast, no difference was found between Smad2cKO and control mice in the CPU. Altogether, our results demonstrate that Smad1 and Smad2 regulate dopaminergic presynaptic differentiation *in vivo* in a pathway-specific manner.

To examine whether Smads regulate the maintenance of dopaminergic synapses, we inactivated Smads in mDA neurons in adults (Figure S7A). We found that the inactivation of Smads in adults decreased the size of VMAT2 puncta, specifically in the CPU in Smad1cKO and in the NAc in Smad2cKO mice (Figures S7B–S7G). Inactivation of either Smad did not affect the TH intensity in the striatum (Figures S7H and S7I). These results suggest that in addition to the initial formation, Smads contribute to the maintenance of dopaminergic synapses in a region-specific manner.

Glia are involved in the differentiation and survival of mDA neurons.<sup>32,33</sup> To exclude the possibility that BMPs/TGF- $\beta$ 2 signal through glia for dopaminergic presynaptic differentiation, we postnatally inactivated Smad1 and Smad2 in astrocytes.<sup>34</sup> We found that in both cKO mice, there was no change in VMAT2

Figure 4. Differentially expressed BMPR and TGF- $\beta$ R mediate dopaminergic presynaptic differentiation of SNc and VTA neurons, respectively, through the activation of distinct Smads

(A–G) Differential expression of BMPR and TGF- $\beta$ R in mDA neurons. (A–D) Cultured midbrain neurons were stained at 7 DIV for GIRK2 or calbindin, TH, and BMPR or TGF- $\beta$ R. (A and B) Representative images of the cell body of SNc (GIRK2 $^{+}$ , TH $^{+}$ ) and VTA (calbindin $^{+}$ , TH $^{+}$ ) dopaminergic neurons. (C) BMPR is preferentially expressed in the nigrostriatal (calbindin $^{-}$ , TH $^{+}$ ) projections. (D) TGF- $\beta$ R is expressed in the mesolimbic (calbindin $^{+}$ , TH $^{+}$ ) projections. Scale bars, 10  $\mu$ m. Observations from 12 to 16 SNc or VTA cells from 3 independent experiments. (E–G) BMPR/TGF- $\beta$ R staining in midbrain sections. Low magnification images (E), high magnification images (F), and quantification of staining intensities (G). Scale bars, 200  $\mu$ m (E), 50  $\mu$ m (F). n (cells; mice)= 53–126; 2–3 (G), Student's t test. (H and I) BMPR and TGF- $\beta$ R specifically mediate dopaminergic presynaptic differentiation of SNc or VTA neurons, respectively. Cultured midbrain neurons were treated with the CPU or NAc extract with or without the BMPR inhibitor or TGF- $\beta$ R inhibitor (1  $\mu$ M) at 4 DIV and stained at 6 DIV. Scale bars, 10  $\mu$ m. n (cells; independent experiments) = 14–16; 4–5 (H), 13–16; 3 (I), one-way ANOVA with Tukey's test.

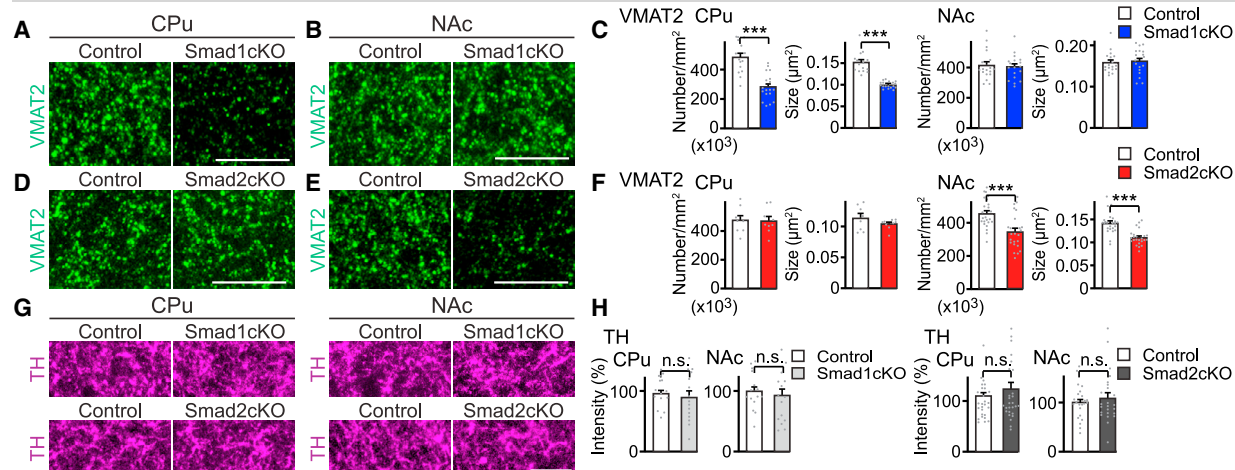
(J–M) BMP6/BMP2 activate Smad1 in SNc dopaminergic neurons; TGF- $\beta$ 2 activates Smad2 in VTA dopaminergic neurons. Cultured midbrain neurons were treated with each factor at 5 DIV for 45 min and stained for phospho-Smads. Scale bars, 10  $\mu$ m. n = 3–4 independent experiments, one-way ANOVA with Tukey's test.

(N–Q) Developmental time course of phospho-Smad1 and phospho-Smad2 expressions in dopaminergic neurons in the midbrain and striatum. Scale bars, 50  $\mu$ m (N and O) and 5  $\mu$ m (P and Q). n (fields; mice) = 30–90; 2–3 (N and O), 4–8; 2 (P and Q). Student's *t* test.

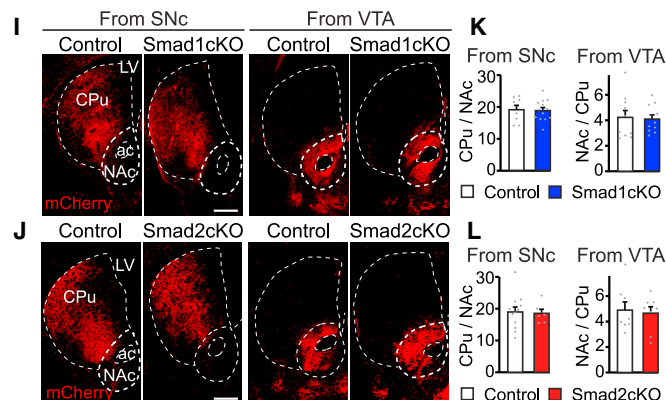
Data are represented as mean  $\pm$  SEM.



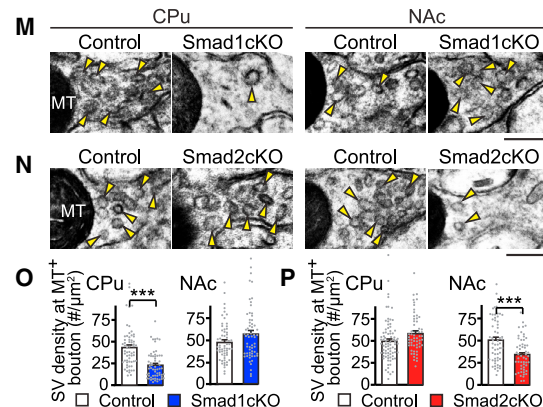
### Projection-specific defects in dopaminergic presynaptic differentiation in SmadcoKO mice



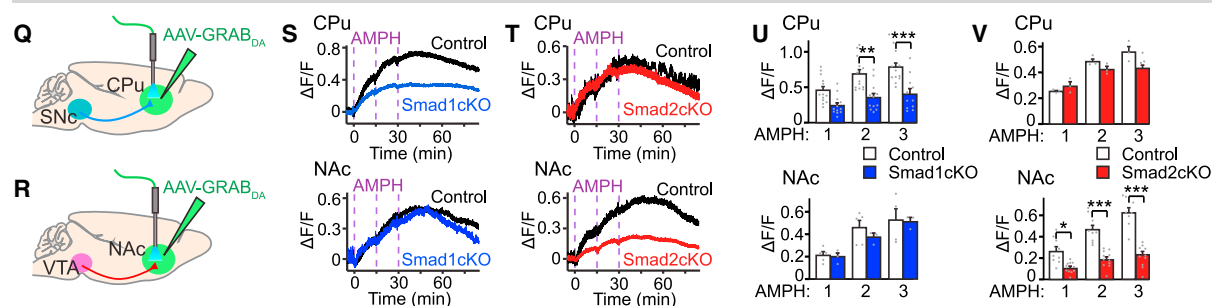
### Dopaminergic axon targeting is normal in SmadcKO mice



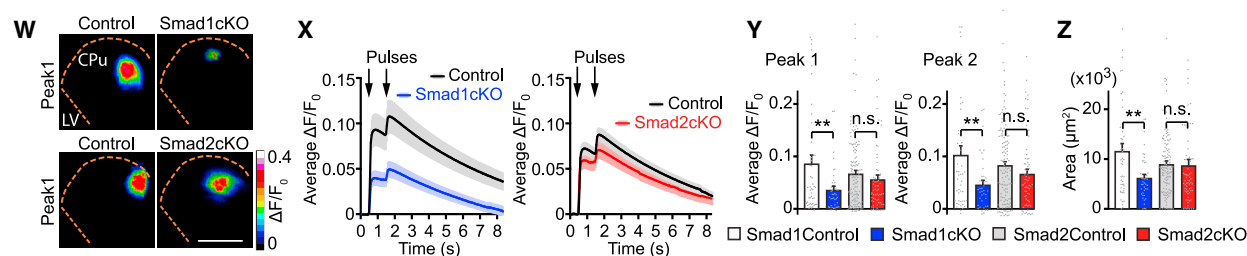
### Ultrastructure of dopaminergic presynaptic terminals



### Projection-specific decreases in dopamine release *in vivo* in Smad $\alpha$ 1KO mice



### Action potential-dependent dopamine release in Smad $\alpha$ KO mice



(legend on next page)



clustering (Figures S7J–S7O) or TH intensity (Figures S7P and S7Q) in the striatum. These data indicate that postnatal inactivation of Smads in astrocytes has no effect on dopaminergic presynaptic differentiation in the striatum, suggesting that BMPs/TGF- $\beta$ 2 are acting directly onto mDA neurons for their presynaptic differentiation.

### Smad1cKO mice show motor defects, and Smad2cKO mice show a lack of motivation

Finally, we investigated the behavioral consequences of Smad inactivation in mDA neurons. The nigrostriatal pathway regulates motor functions, such as exploration and movement, and cognitive functions, such as associative task learning.<sup>3–5,35–37</sup> On the other hand, the mesolimbic pathway regulates motivation, reward responses, and emotion.<sup>6–8,38–40</sup> Therefore, we performed the open-field test and the rearing test to assess exploration; the cylinder (limb asymmetry use) test to assess dopamine-dependent movement; the operant conditioning test to assess associative task learning, cognitive flexibility, and motivation; and the prepulse inhibition (PPI) test to assess sensorimotor gating.

In the open-field test, Smad1cKO mice, but not Smad2cKO mice, exhibited a decreased total distance traveled relative to control mice (Figure 6A). In the rearing test, the number of rearing events was significantly decreased in Smad1cKO mice, but not in Smad2cKO mice (Figure 6B). These results suggest that Smad1cKO, but not Smad2cKO, mice show impaired exploratory behavior, consistent with the role of the nigrostriatal pathway in exploration.

For the cylinder test, we unilaterally inactivated Smad1 or Smad2 in the mDA neurons located in the SNc or VTA. The cylinder test is a common behavioral test to evaluate dopamine-dependent motor impairment, and unilaterally dopamine-depleted rodents preferentially use the forelimb ipsilateral to the lesion for wall exploration and landing.<sup>41</sup> We found that the cKO mice, in which Smad1 was unilaterally inactivated in SNc mDA neurons, showed a significant reduction in the co-use of both forelimbs and instead, an increase in the use of ipsilateral forelimb for landing (Figure 6C), consistent with the role of the nigrostriatal pathway in movement. cKO mice in which Smad1 was

inactivated in VTA mDA neurons and those in which Smad2 was inactivated were normal in this test (Figure 6C).

In the operant conditioning test, we performed the visual discrimination (VD) task, which involves associative task learning and decision making, followed by the reversal learning (RL) task, which requires cognitive flexibility when faced with changing rules (Figure 6D). We performed one session per day. A session ends either after 60 trials or 60 min, whichever comes first (Figure 6E). In the VD task, Smad1cKO mice required more days to reach the criterion (>80% correct responses out of 60 trials within 60 min for 2–3 consecutive days) (Figure 6F, VD), made more errors (Figure 6G, VD), and needed more trials (Figure 6H, VD). Smad2cKO mice did not show such changes, suggesting that Smad1cKO, but not Smad2cKO, mice have defects in associative task learning, consistent with the role of the nigrostriatal pathway in task learning.<sup>37,42</sup> By contrast, in the RL task, Smad2cKO, but not Smad1cKO, mice required more days to reach the criterion (Figure 6F, RL). However, the numbers of errors made and trials needed to reach the criterion were not significantly different between control and Smad2cKO mice (Figures 6G and 6H, RL). We found that this discrepancy is because Smad2cKO mice, especially at the beginning of the RL task when the animals are challenged with changing rules, performed fewer trials (Figure 6I) and spent more time completing a session (Figure 6J, RL). This result suggests there is a lack of motivation<sup>43</sup> in Smad2cKO mice, which is consistent with the role of the mesolimbic pathway in regulating motivation. No such changes were found in Smad1cKO mice (Figures 6I and 6J).

PPI is affected by dopamine. The nigrostriatal and mesolimbic dopaminergic pathways appear to differentially regulate PPI: a decrease in PPI is associated with decreased nigrostriatal dopamine or increased mesolimbic dopamine.<sup>44–48</sup> We found that both Smad1cKO and Smad2cKO mice showed normal acoustic startle responses (Figure 6K). Interestingly, they showed distinct changes in PPI (Figure 6K): Smad1cKO mice showed a decrease in PPI, whereas Smad2cKO mice showed an increase in PPI.

These results are consistent with our finding that Smad1 and Smad2 specifically regulate the nigrostriatal and mesolimbic dopamine synapse formation, respectively, and indicate that

### Figure 5. Smad1 specifically regulates nigrostriatal dopaminergic synaptogenesis, whereas Smad2 regulates mesolimbic dopaminergic synaptogenesis, *in vivo*

In Smad1cKO and Smad2cKO mice, Smad1 or Smad2 is postnatally inactivated in dopaminergic neurons.

(A–H) Striatal sections from P14 Smad1cKO and control mice were immunostained for VMAT2 (A–F) and TH (G and H). VMAT2 clustering was specifically decreased in CPu of Smad1cKO (A–C) and in NAc of Smad2cKO mice (D–F). Scale bars, 10  $\mu$ m. n (fields; mice) = 15–18; 5 (C), 8–24; 7 (F), 15–27; 5–7 (H), Student's t test.

(I–L) Dopaminergic axons from the SNc or VTA were traced by expressing mCherry. (I and J) Representative images of coronal striatal sections from 2- to 4-month-old mice. LV, lateral ventricle. (K and L) Ratios of mCherry intensities were calculated to evaluate dopaminergic axon targeting from the SNc (ratios shown are CPu/NAc) and VTA (ratios shown are NAc/CPu). Scale bars, 500  $\mu$ m. n (sections; mice) = 8–12; 4–6, Student's t test.

(M–P) Ultrastructure of dopaminergic presynaptic terminals. Dopaminergic presynaptic terminals were identified by Matrix-dAPEX2-based synaptic labeling. Scale bars, 200 nm. The number of SVs (yellow arrowheads) in each dopaminergic presynaptic terminal (labeled-mitochondria-positive [MT<sup>+</sup>] bouton) was quantified (O and P). n (cells; mice) = 60; 3 (O), 55–80; 3–4 (P), Student's t test.

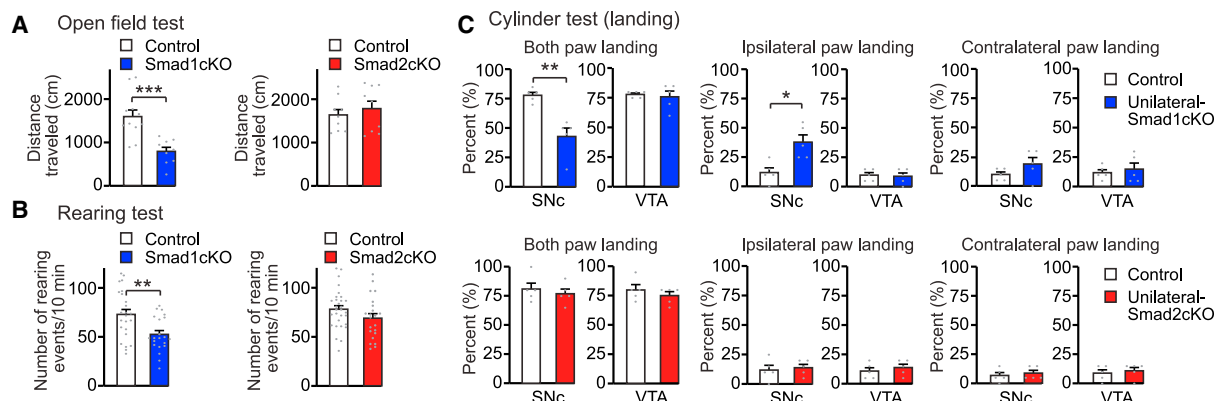
(Q–V) Extracellular dopamine release *in vivo* in CPu and NAc of Smad1cKO and control mice. Schematic of the adeno-associated virus (AAV)-GRAB<sub>DA</sub> injection and recording sites in the CPu (Q) and NAc (R). Dopamine release in response to amphetamine was measured using fiber photometry with GRAB<sub>DA</sub>. Amphetamine was injected three times (at 0, 15, and 30 min). (S and T) Representative traces of dopamine release (increase in  $\Delta F/F$ ). (U and V) Quantification of the peak  $\Delta F/F$  in response to each amphetamine injection in CPu and NAc. n (experiments; mice) = 3–13; 3–5, two-way ANOVA with Tukey's test.

(W–Z) Action potential-dependent dopamine release in Smad1cKO and control mice. GRAB<sub>DA</sub> imaging in CPu slices in response to electrical stimulation (W). The level (average  $\Delta F/F_0$ ) (X and Y) and extent (area) (Z) of dopamine release in response to electrical stimulation. Scale bar, 500  $\mu$ m. n (fields; mice) = 40–127; 4–8 (Y), 41–120; 4–8 (Z), one-way ANOVA with Bonferroni's test.

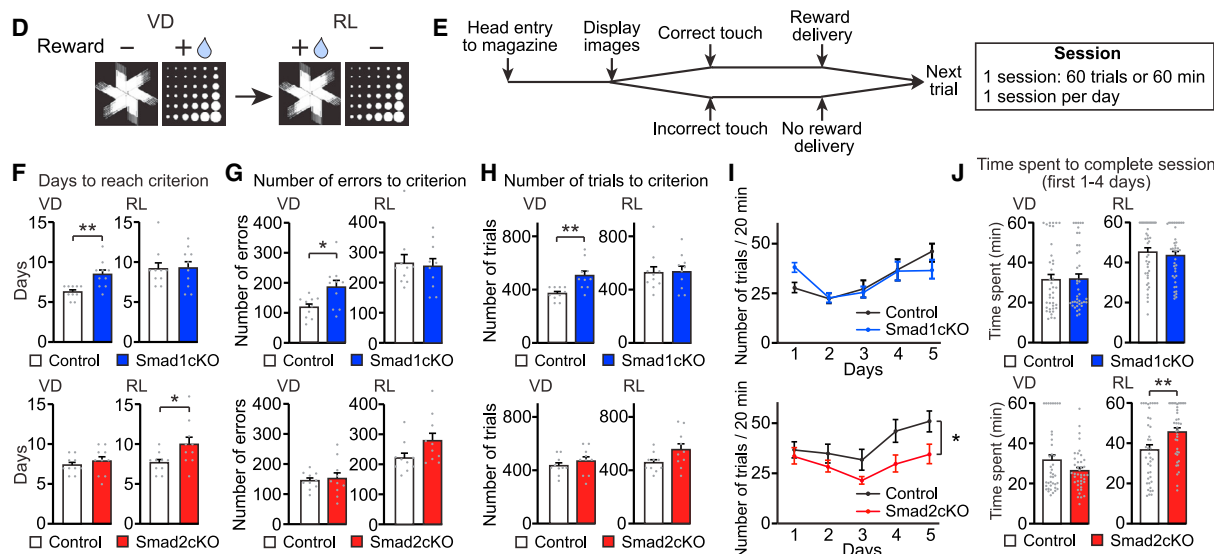
Data are represented as mean  $\pm$  SEM.

See also Figures S3–S7.

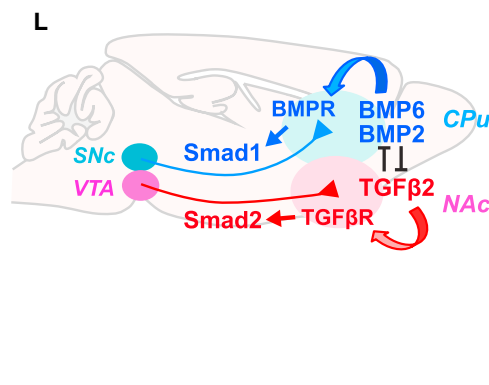
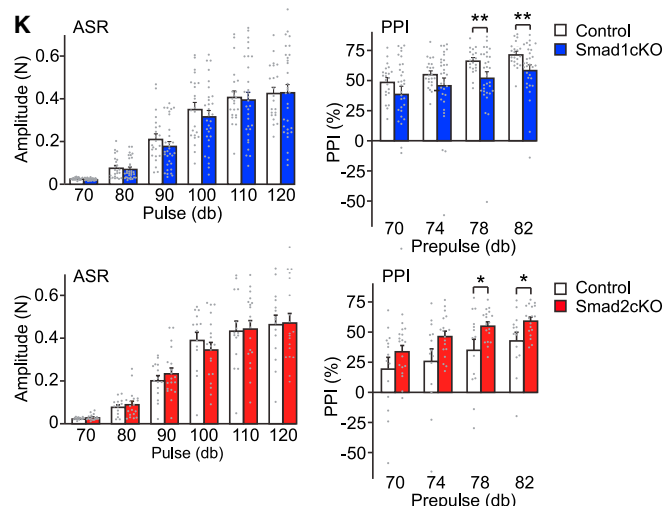
# Smad1cKO mice show motor defects



# Smad1cKO and Smad2cKO mice show distinct defects in the operant conditioning test



# Smad1cKO and Smad2cKO mice show distinct changes in prepulse inhibition



(legend on next page)

inactivation of Smad1 or Smad2 in dopamine neurons has significant consequences on relevant behaviors.

## DISCUSSION

Despite the well-known importance of the dopaminergic pathways to motor function, emotion, motivation, and reward association, as well as their implication in many diseases, we know very little about dopaminergic synaptogenesis. Here we showed that dopaminergic synapses are established in a pathway-specific manner by distinct target-derived factors with distinct signaling pathways that antagonize each other. We identify the BMP6/2-BMPR-Smad1 axis as the organizing pathway for nigrostriatal projections and the TGF- $\beta$ 2-TGF- $\beta$ R-Smad2 axis for mesolimbic projections (Figure 6L). Postnatal inactivation of Smads in mDA neurons did not affect their survival, axon targeting, dendritic development, and synapses formed onto them, indicating that postnatally, Smad signaling is specifically important for dopaminergic presynaptic differentiation. Interestingly, embryonic inactivation of TGF- $\beta$  signaling affects mDA neuron survival, dendritic growth, and synapses onto them,<sup>49–52</sup> suggesting that Smad signaling contributes to various aspects of development in a temporally regulated manner. In addition, BMP/TGF- $\beta$  signaling is known to act both locally and globally, which may contribute to synapse-specific, compartmentalized effects.

The specificity of the effects by BMP6/BMP2 vs. TGF- $\beta$ 2 is achieved at multiple levels. (1) BMP6/BMP2 and TGF- $\beta$ 2 are preferentially expressed by the CPu and NAc, respectively; (2) their receptors, BMPR and TGF- $\beta$ R, are preferentially expressed by nigrostriatal or mesolimbic neurons; and (3) distinct Smads mediate dopaminergic presynaptic development of nigrostriatal and mesolimbic pathways. An interesting aspect of our study is that the BMP-Smad1 and TGF- $\beta$ -Smad2 signaling pathways are known to antagonize each other.<sup>16</sup> Indeed, the effects of BMP6/2 on dopaminergic presynaptic differentiation in SNc neurons are suppressed by TGF- $\beta$ 2, and the effects of TGF- $\beta$ 2 on dopaminergic presynaptic differentiation in VTA neurons are suppressed by BMP6/2, which could strengthen the specific segregation of nigrostriatal and mesolimbic pathways. BMP3 might also play a role in enhancing this specificity. The *Bmp3* gene is more abundantly expressed in the NAc than CPu (Table 1). BMP3 is a unique BMP in that it can bind to BMPR but does

not signal.<sup>53</sup> Hence, BMP3 expressed in the NAc could act as an antagonist against BMP6/BMP2 (nigrostriatal dopaminergic organizers), and thus, it could increase the specificity for the mesolimbic pathway. BMPs may also synergize with each other for their effects. Indeed, we found that BMP6/2 heterodimers more strongly induce VMAT2 clustering in SNc dopaminergic neurons than either of the homodimers. Therefore, multiple BMP/TGF- $\beta$  signals appear to interact, by antagonizing or synergizing, to establish appropriate dopaminergic projections.

Secreted factors may also cooperate with cell-adhesion molecules, as they do at glutamatergic and GABAergic synapses.<sup>54–56</sup> A previous study suggested that neuroligin-2 may control the balance between GABAergic and dopaminergic synapses.<sup>11</sup> Thus, BMP6/BMP2/TGF- $\beta$ 2 and neuroligin-2 may work in concert by sequentially regulating dopaminergic synapse development—after the induction of dopaminergic presynaptic terminals by BMP6/BMP2/TGF- $\beta$ 2, neuroligin-2 may control the number of dopaminergic synapses.

Highlighting dopamine's importance is its central role in many neuropsychiatric disorders. The nigrostriatal dopaminergic pathway regulates movement and is associated with Parkinson's disease.<sup>3,4</sup> Many psychostimulants activate the mesolimbic dopaminergic pathway, and alterations in the mesolimbic pathway are implicated in many neuropsychiatric disorders such as schizophrenia, ADHD, depression, and addiction.<sup>6–8</sup> In fact, our behavioral studies revealed that Smad1cKO mice showed motor defects, whereas Smad2cKO mice showed lack of motivation. Therefore, these cKO mice may provide new models of neuropsychiatric disorders. Because Smads are involved in the development and maintenance of dopaminergic synapses, our results suggest that we could design new strategies to treat such disorders by targeting Smad1 and Smad2. Appropriate application or blockade of BMP-Smad1 or TGF- $\beta$ -Smad2 may regulate dopamine levels in a pathway-specific manner in order to treat neuropsychiatric disorders with abnormal dopaminergic synapses.

## Limitations of the study

It would be interesting to examine the genes downregulated in SmadcKO mice, and we are preparing mice to perform RNA sequencing. As a first step toward this question, we have examined the protein expressions of VMAT2 and bassoon in mDA neurons in SmadcKO mice. Our results suggest that there is a

### Figure 6. Smad1cKO mice show motor defects, and Smad2cKO mice show lack of motivation

(A) Open-field test. Total distance traveled in 5 min.  $n = 9–11$  mice, Student's  $t$  test.  
 (B) Rearing test. The number of rearing events in 10 min.  $n = 21–30$  mice, Student's  $t$  test.  
 (C) Cylinder test. Smad1 or Smad2 was unilaterally inactivated in mDA neurons located in the SNc or VTA for the cylinder test. Forelimb landings were classified into both-paw, ipsilateral-paw, or contralateral-paw landing.  $n = 5$  mice, Student's  $t$  test.  
 (D–J) Operant conditioning test. (D) One of the two images, “fan” or “marble,” was linked to a reward in the visual discrimination (VD) and reversal learning (RL) test, where the reward-linked image was reversed in RL. Reward-linked images were counter-balanced. (E) Timeline: one session ends either after 60 trials or 60 min, whichever comes first. One session was performed per day. The completion criterion of the tasks was set as  $>80\%$  correct responses out of 60 trials within 60 min for 2–3 consecutive days. The days spent to reach the criterion (F), the numbers of errors made to reach the criterion (G), and the numbers of trials needed to reach the criterion (H) were quantified. (I) Numbers of trials performed in 20 min during RL. (J) Time spent completing a session at the beginning of VD and RL.  $n = 10$  mice, Student's  $t$  test (F–H and J), and two-way repeated-measures ANOVA (I).  
 (K) Acoustic startle response (ASR) and prepulse inhibition (PPI).  $n = 15–31$  mice, Student's  $t$  test.  
 (L) Model: dopaminergic synapses are established in a pathway-specific manner by specific target-derived factors with distinct signaling pathways that antagonize each other: target-derived BMP6/BMP2 establish nigrostriatal dopaminergic synapses through BMPR and Smad1 signaling; target-derived TGF- $\beta$ 2 establishes mesolimbic dopaminergic synapses through TGF- $\beta$ R and Smad2 signaling.  
 Data are represented as mean  $\pm$  SEM.

significant decrease in the VMAT2 expression in the VTA (and not in the SNc) dopamine neurons in Smad2cKO mice, which may contribute to dopaminergic synaptic defects. The expression of bassoon was not significantly different between control and SmadcKO mice.

Testing the effects of BMP/TGF- $\beta$  on SmadcKO cultures will provide additional support. However, this requires the establishment of mouse dopaminergic neuronal cultures, which we found is much harder than rat dopaminergic neuronal cultures.

Although we have backcrossed the SmadcKO mice with C57BL/6J mice at least 5 times, there still could be differences in the genetic background, environmental factors, etc. that may affect the results. To minimize such variabilities, we have always used littermates as controls.

## STAR★METHODS

Detailed methods are provided in the online version of this paper and include the following:

- **KEY RESOURCES TABLE**
- **RESOURCE AVAILABILITY**
  - Lead contact
  - Materials availability
  - Data and code availability
- **EXPERIMENTAL MODEL AND STUDY PARTICIPANT DETAILS**
  - Animals
- **METHOD DETAILS**
  - Primary neuronal cultures
  - Brain extract preparation
  - Factors
  - Microarray
  - *In situ* hybridization
  - RT-PCR
  - Immunostaining
  - Imaging
  - shRNA constructs
  - AAV constructs
  - Lentivirus and AAV preparation
  - Stereotaxic injections to pups
  - Electron microscopy
  - Fiber photometry
  - GRAB<sub>DA</sub> imaging in striatal slices
  - Behavioral tests
- **QUANTIFICATION AND STATISTICAL ANALYSIS**
  - Degrees of freedom and F/t values in figures

## SUPPLEMENTAL INFORMATION

Supplemental information can be found online at <https://doi.org/10.1016/j.cell.2023.07.023>.

## ACKNOWLEDGMENTS

We thank Kelly Hoover, Julie Wilson, Rebecca Lin, Jaanvi Sant, and Jessica Wei for their help with histological and behavioral analysis; Cindy Carruthers, Masahiro Yasuda, and Michael Fox for their technical assistance; Salvador Brito, Mariko Hashimoto, and Todd Anthony for their help with fiber photom-

etry; Aditi Banerjee and Pascal Kaeser for their help with GRAB<sub>DA</sub> imaging; Sivapratha Nagappan-Chettiar for their critical reading of the manuscript; Boston Children's Hospital Viral Core for virus preparation; University of Michigan DNA Sequencing Core for microarray analysis; and the Harvard Medical School EM Facility for EM analysis. This work was supported by Tommy Fuss Center grant (A.T.), NIH grant R35-NS097344 (D.D.G.), NIH grant R01-DA042744, NIH grant R01-MH125162, and American Parkinson Disease Association grant (H.U.).

## AUTHOR CONTRIBUTIONS

Conceptualization, A.T. and H.U.; methodology, A.T., P.Y., E.M.J.-V., M.P.S., Q.Z., J.Z., Y.L., D.D.G., W.-C.A.L., and H.U.; software, J.Z.; formal analysis, A.T., P.Y., E.M.J.-V., M.P.S., L.K., J.C.P., E.K., and H.U.; investigation, A.T., P.Y., E.M.J.-V., M.P.S., L.K., J.C.P., and E.K.; resources, Q.Z., Y.L., D.D.G., and W.-C.A.L.; writing – original draft, A.T. and H.U.; writing – review & editing, all co-authors; supervision, H.U.; funding acquisition, J.Z., Y.L., D.D.G., W.-C.A.L., and H.U.

## DECLARATION OF INTERESTS

The authors declare no competing interests.

## INCLUSION AND DIVERSITY

We worked to ensure sex balance in the selection of non-human subjects. One or more of the authors of this paper self-identifies as an underrepresented ethnic minority in their field of research or within their geographical location.

Received: August 10, 2022

Revised: May 28, 2023

Accepted: July 14, 2023

Published: August 14, 2023

## REFERENCES

1. Cox, J., and Witten, I.B. (2019). Striatal circuits for reward learning and decision-making. *Nat. Rev. Neurosci.* 20, 482–494. <https://doi.org/10.1038/s41583-019-0189-2>.
2. Björklund, A., and Dunnett, S.B. (2007). Dopamine neuron systems in the brain: an update. *Trends Neurosci.* 30, 194–202. <https://doi.org/10.1016/j.tins.2007.03.006>.
3. Dauer, W., and Przedborski, S. (2003). Parkinson's disease: mechanisms and models. *Neuron* 39, 889–909. [https://doi.org/10.1016/s0896-6273\(03\)00568-3](https://doi.org/10.1016/s0896-6273(03)00568-3).
4. Sulzer, D. (2007). Multiple hit hypotheses for dopamine neuron loss in Parkinson's disease. *Trends Neurosci.* 30, 244–250. <https://doi.org/10.1016/j.tins.2007.03.009>.
5. Chen, J.Y., Wang, E.A., Cepeda, C., and Levine, M.S. (2013). Dopamine imbalance in Huntington's disease: a mechanism for the lack of behavioral flexibility. *Front. Neurosci.* 7, 114. <https://doi.org/10.3389/fnins.2013.00114>.
6. Dichter, G.S., Damiano, C.A., and Allen, J.A. (2012). Reward circuitry dysfunction in psychiatric and neurodevelopmental disorders and genetic syndromes: animal models and clinical findings. *J. Neurodev. Disord.* 4, 19. <https://doi.org/10.1186/1866-1955-4-19>.
7. Russo, S.J., and Nestler, E.J. (2013). The brain reward circuitry in mood disorders. *Nat. Rev. Neurosci.* 14, 609–625. <https://doi.org/10.1038/nrn3381>.
8. Volkow, N.D., and Morales, M. (2015). The brain on drugs: from reward to addiction. *Cell* 162, 712–725. <https://doi.org/10.1016/j.cell.2015.07.046>.
9. Yung, K.K., Bolam, J.P., Smith, A.D., Hersch, S.M., Ciliax, B.J., and Levey, A.I. (1995). Immunocytochemical localization of D1 and D2 dopamine receptors in the basal ganglia of the rat: light and electron microscopy. *Neuroscience* 65, 709–730. [https://doi.org/10.1016/0306-4522\(94\)00536-e](https://doi.org/10.1016/0306-4522(94)00536-e).



10. Descarries, L., Watkins, K.C., Garcia, S., Bosler, O., and Doucet, G. (1996). Dual character, asynaptic and synaptic, of the dopamine innervation in adult rat neostriatum: a quantitative autoradiographic and immunocytochemical analysis. *J. Comp. Neurol.* 375, 167–186. [https://doi.org/10.1002/\(SICI\)1096-9861\(19961111\)375:2<167::AID-CNE1>3.0.CO;2-0](https://doi.org/10.1002/(SICI)1096-9861(19961111)375:2<167::AID-CNE1>3.0.CO;2-0).
11. Uchigashima, M., Ohtsuka, T., Kobayashi, K., and Watanabe, M. (2016). Dopamine synapse is a neuroligin-2-mediated contact between dopaminergic presynaptic and GABAergic postsynaptic structures. *Proc. Natl. Acad. Sci. USA* 113, 4206–4211. <https://doi.org/10.1073/pnas.1514074113>.
12. Mendez, I., Sanchez-Pernaute, R., Cooper, O., Viñuela, A., Ferrari, D., Björklund, L., Dagher, A., and Isacson, O. (2005). Cell type analysis of functional fetal dopamine cell suspension transplants in the striatum and substantia nigra of patients with Parkinson's disease. *Brain* 128, 1498–1510. <https://doi.org/10.1093/brain/awh510>.
13. Thompson, L., Barraud, P., Andersson, E., Kirik, D., and Björklund, A. (2005). Identification of dopaminergic neurons of nigral and ventral tegmental area subtypes in grafts of fetal ventral mesencephalon based on cell morphology, protein expression, and efferent projections. *J. Neurosci.* 25, 6467–6477. <https://doi.org/10.1523/JNEUROSCI.1676-05.2005>.
14. Miyazono, K., Kamiya, Y., and Morikawa, M. (2010). Bone morphogenetic protein receptors and signal transduction. *J. Biochem.* 147, 35–51. <https://doi.org/10.1093/jb/mvp148>.
15. Bragdon, B., Moseychuk, O., Saldanha, S., King, D., Julian, J., and Nohe, A. (2011). Bone morphogenetic proteins: a critical review. *Cell. Signal.* 23, 609–620. <https://doi.org/10.1016/j.cellsig.2010.10.003>.
16. Wakefield, L.M., and Hill, C.S. (2013). Beyond TGF $\beta$ : roles of other TGF $\beta$  superfamily members in cancer. *Nat. Rev. Cancer* 13, 328–341. <https://doi.org/10.1038/nrc3500>.
17. Kalinovskiy, A., and Scheiffele, P. (2004). Transcriptional control of synaptic differentiation by retrograde signals. *Curr. Opin. Neurobiol.* 14, 272–279. <https://doi.org/10.1016/j.conb.2004.05.011>.
18. Ball, R.W., Warren-Paquin, M., Tsurudome, K., Liao, E.H., Elazzouzi, F., Cavanagh, C., An, B.S., Wang, T.T., White, J.H., and Haghighi, A.P. (2010). Retrograde BMP signaling controls synaptic growth at the NMJ by regulating trio expression in motor neurons. *Neuron* 66, 536–549. <https://doi.org/10.1016/j.neuron.2010.04.011>.
19. Guo, J., and Wu, G. (2012). The signaling and functions of heterodimeric bone morphogenetic proteins. *Cytokine Growth Factor Rev.* 23, 61–67. <https://doi.org/10.1016/j.cytogfr.2012.02.001>.
20. Isaacs, M.J., Kawakami, Y., Allendorph, G.P., Yoon, B.H., Izpisua Belmonte, J.C., and Choe, S. (2010). Bone morphogenetic protein-2 and -6 heterodimer illustrates the nature of ligand-receptor assembly. *Mol. Endocrinol.* 24, 1469–1477. <https://doi.org/10.1210/me.2009-0496>.
21. Valera, E., Isaacs, M.J., Kawakami, Y., Izpisua Belmonte, J.C., and Choe, S. (2010). BMP-2/6 heterodimer is more effective than BMP-2 or BMP-6 homodimers as inductor of differentiation of human embryonic stem cells. *PLoS One* 5, e11167. <https://doi.org/10.1371/journal.pone.0011167>.
22. Gerfen, C.R., and Surmeier, D.J. (2011). Modulation of striatal projection systems by dopamine. *Annu. Rev. Neurosci.* 34, 441–466. <https://doi.org/10.1146/annurev-neuro-061010-113641>.
23. Grygielko, E.T., Martin, W.M., Tweed, C., Thornton, P., Harling, J., Brooks, D.P., and Laping, N.J. (2005). Inhibition of gene markers of fibrosis with a novel inhibitor of transforming growth factor-beta type I receptor kinase in puromycin-induced nephritis. *J. Pharmacol. Exp. Ther.* 313, 943–951. <https://doi.org/10.1124/jpet.104.082099>.
24. Boergermann, J.H., Kopf, J., Yu, P.B., and Knaus, P. (2010). Dorsomorphin and LDN-193189 inhibit BMP-mediated Smad, p38 and Akt signalling in C2C12 cells. *Int. J. Biochem. Cell Biol.* 42, 1802–1807. <https://doi.org/10.1016/j.biocel.2010.07.018>.
25. Keshishian, H., and Kim, Y.S. (2004). Orchestrating development and function: retrograde BMP signaling in the Drosophila nervous system. *Trends Neurosci.* 27, 143–147. <https://doi.org/10.1016/j.tins.2004.01.004>.
26. Ji, S.J., and Jaffrey, S.R. (2012). Intra-axonal translation of SMAD1/5/8 mediates retrograde regulation of trigeminal ganglia subtype specification. *Neuron* 74, 95–107. <https://doi.org/10.1016/j.neuron.2012.02.022>.
27. Huang, S., Tang, B., Usoskin, D., Lechleider, R.J., Jamin, S.P., Li, C., Anzano, M.A., Ebendal, T., Deng, C., and Roberts, A.B. (2002). Conditional knockout of the Smad1 gene. *Genesis* 32, 76–79. <https://doi.org/10.1002/gene.10059>.
28. Ju, W., Ogawa, A., Heyer, J., Nierhof, D., Yu, L., Kucherlapati, R., Shafritz, D.A., and Böttinger, E.P. (2006). Deletion of Smad2 in mouse liver reveals novel functions in hepatocyte growth and differentiation. *Mol. Cell. Biol.* 26, 654–667. <https://doi.org/10.1128/MCB.26.2.654-667.2006>.
29. Zhang, Q., Lee, W.A., Paul, D.L., and Ginty, D.D. (2019). Multiplexed peroxidase-based electron microscopy labeling enables simultaneous visualization of multiple cell types. *Nat. Neurosci.* 22, 828–839. <https://doi.org/10.1038/s41593-019-0358-7>.
30. Sun, F., Zhou, J., Dai, B., Qian, T., Zeng, J., Li, X., Zhuo, Y., Zhang, Y., Wang, Y., Qian, C., et al. (2020). Next-generation GRAB sensors for monitoring dopaminergic activity in vivo. *Nat. Methods* 17, 1156–1166. <https://doi.org/10.1038/s41592-020-00981-9>.
31. Liu, C., Cai, X., Ritzau-Jost, A., Kramer, P.F., Li, Y., Khaliq, Z.M., Hallermann, S., and Kaeser, P.S. (2022). An action potential initiation mechanism in distal axons for the control of dopamine release. *Science* 375, 1378–1385. <https://doi.org/10.1126/science.abn0532>.
32. Hall, A.C., Mira, H., Wagner, J., and Arenas, E. (2003). Region-specific effects of glia on neuronal induction and differentiation with a focus on dopaminergic neurons. *Glia* 43, 47–51. <https://doi.org/10.1002/glia.10229>.
33. Arenas, E., Denham, M., and Villaseca, J.C. (2015). How to make a midbrain dopaminergic neuron. *Development* 142, 1918–1936. <https://doi.org/10.1242/dev.097394>.
34. Srinivasan, R., Lu, T.Y., Chai, H., Xu, J., Huang, B.S., Golshani, P., Coppola, G., and Khakh, B.S. (2016). New transgenic mouse lines for selectively targeting astrocytes and studying calcium signals in astrocyte processes in situ and in vivo. *Neuron* 92, 1181–1195. <https://doi.org/10.1016/j.neuron.2016.11.030>.
35. Haber, S.N. (2014). The place of dopamine in the cortico-basal ganglia circuit. *Neuroscience* 282, 248–257. <https://doi.org/10.1016/j.neuroscience.2014.10.008>.
36. Klaus, A., Alves da Silva, J., and Costa, R.M. (2019). What, if, and when to move: basal ganglia circuits and self-paced action initiation. *Annu. Rev. Neurosci.* 42, 459–483. <https://doi.org/10.1146/annurev-neuro-072116-031033>.
37. Conn, K.A., Burne, T.H.J., and Kesby, J.P. (2020). Subcortical dopamine and cognition in schizophrenia: looking beyond psychosis in preclinical models. *Front. Neurosci.* 14, 542. <https://doi.org/10.3389/fnins.2020.00542>.
38. Nestler, E.J., and Carlezon, W.A., Jr. (2006). The mesolimbic dopamine reward circuit in depression. *Biol. Psychiatry* 59, 1151–1159. <https://doi.org/10.1016/j.biopsych.2005.09.018>.
39. Salamone, J.D., Yohn, S.E., López-Cruz, L., San Miguel, N., and Correa, M. (2016). Activation and effort-related aspects of motivation: neural mechanisms and implications for psychopathology. *Brain* 139, 1325–1347. <https://doi.org/10.1093/brain/aww050>.
40. Halbout, B., Marshall, A.T., Azimi, A., Liljeholm, M., Mahler, S.V., Wassum, K.M., and Ostlund, S.B. (2019). Mesolimbic dopamine projections mediate cue-motivated reward seeking but not reward retrieval in rats. *eLife* 8, e43551. <https://doi.org/10.7554/eLife.43551>.
41. Schallert, T., Fleming, S.M., Leasure, J.L., Tillerson, J.L., and Bland, S.T. (2000). CNS plasticity and assessment of forelimb sensorimotor outcome in unilateral rat models of stroke, cortical ablation, parkinsonism and spinal

- cord injury. *Neuropharmacology* 39, 777–787. [https://doi.org/10.1016/s0028-3908\(00\)00005-8](https://doi.org/10.1016/s0028-3908(00)00005-8).
42. Losos, M.J., and Dunnett, S.B. (2011). Aberrant dopamine transmission and cognitive dysfunction in animal models of Parkinson's disease. *J. Parkinsons Dis.* 1, 151–165. <https://doi.org/10.3233/JPD-2011-11036>.
43. Hailwood, J.M., Heath, C.J., Robbins, T.W., Saksida, L.M., and Bussey, T.J. (2018). Validation and optimisation of a touchscreen progressive ratio test of motivation in male rats. *Psychopharmacology* 235, 2739–2753. <https://doi.org/10.1007/s00213-018-4969-6>.
44. Zhang, J., Forkstam, C., Engel, J.A., and Svensson, L. (2000). Role of dopamine in prepulse inhibition of acoustic startle. *Psychopharmacology* 149, 181–188. <https://doi.org/10.1007/s002130000369>.
45. Ralph, R.J., Paulus, M.P., Fumagalli, F., Caron, M.G., and Geyer, M.A. (2001). Prepulse inhibition deficits and perseverative motor patterns in dopamine transporter knock-out mice: differential effects of D1 and D2 receptor antagonists. *J. Neurosci.* 21, 305–313. <https://doi.org/10.1523/JNEUROSCI.21-01-00305.2001>.
46. Mena, A., and De la Casa, L.G. (2013). Prepulse inhibition modulation by contextual conditioning of dopaminergic activity. *Behav. Brain Res.* 252, 188–194. <https://doi.org/10.1016/j.bbr.2013.06.005>.
47. Rodrigues, S., Salum, C., and Ferreira, T.L. (2017). Dorsal striatum D1-expressing neurons are involved with sensorimotor gating on prepulse inhibition test. *J. Psychopharmacol.* 31, 505–513. <https://doi.org/10.1177/0269881116686879>.
48. Casado-Sainz, A., Gudmundsen, F., Baerentzen, S.L., Lange, D., Ringsted, A., Martinez-Tejada, I., Medina, S., Lee, H., Svarer, C., Keller, S.H., et al. (2022). Dorsal striatal dopamine induces fronto-cortical hypoactivity and attenuates anxiety and compulsive behaviors in rats. *Neuropsychopharmacology* 47, 454–464. <https://doi.org/10.1038/s41386-021-01207-y>.
49. Zhang, J., Pho, V., Bonasera, S.J., Holtzman, J., Tang, A.T., Hellmuth, J., Tang, S., Janak, P.H., Tecott, L.H., and Huang, E.J. (2007). Essential function of HIPK2 in TGF $\beta$ -dependent survival of midbrain dopamine neurons. *Nat. Neurosci.* 10, 77–86. <https://doi.org/10.1038/nn1816>.
50. Hegarty, S.V., Sullivan, A.M., and O'Keeffe, G.W. (2014). Roles for the TGF $\beta$  superfamily in the development and survival of midbrain dopaminergic neurons. *Mol. Neurobiol.* 50, 559–573. <https://doi.org/10.1007/s12035-014-8639-3>.
51. Luo, S.X., Timbang, L., Kim, J.I., Shang, Y., Sandoval, K., Tang, A.A., Whistler, J.L., Ding, J.B., and Huang, E.J. (2016). TGF- $\beta$  signaling in dopaminergic neurons regulates dendritic growth, excitatory-inhibitory synaptic balance, and reversal learning. *Cell Rep.* 17, 3233–3245. <https://doi.org/10.1016/j.celrep.2016.11.068>.
52. Chleilat, E., Skatulla, L., Rahhal, B., Hussein, M.T., Feuerstein, M., Kriegstein, K., and Roussa, E. (2018). TGF- $\beta$  signaling regulates development of midbrain dopaminergic and hindbrain serotonergic neuron subgroups. *Neuroscience* 381, 124–137. <https://doi.org/10.1016/j.neuroscience.2018.04.019>.
53. Gamer, L.W., Nove, J., Levin, M., and Rosen, V. (2005). BMP-3 is a novel inhibitor of both activin and BMP-4 signaling in *Xenopus* embryos. *Dev. Biol.* 285, 156–168. <https://doi.org/10.1016/j.ydbio.2005.06.012>.
54. Fox, M.A., and Umemori, H. (2006). Seeking long-term relationship: axon and target communicate to organize synaptic differentiation. *J. Neurochem.* 97, 1215–1231. <https://doi.org/10.1111/j.1471-4159.2006.03834.x>.
55. Chia, P.H., Li, P., and Shen, K. (2013). Cell biology in neuroscience: cellular and molecular mechanisms underlying presynapse formation. *J. Cell Biol.* 203, 11–22. <https://doi.org/10.1083/jcb.201307020>.
56. Siddiqui, T.J., and Craig, A.M. (2011). Synaptic organizing complexes. *Curr. Opin. Neurobiol.* 21, 132–143. <https://doi.org/10.1016/j.conb.2010.08.016>.
57. Robinson, J.E., Coughlin, G.M., Hori, A.M., Cho, J.R., Mackey, E.D., Turan, Z., Patriarchi, T., Tian, L., and Gradinaru, V. (2019). Optical dopamine monitoring with dLight1 reveals mesolimbic phenotypes in a mouse model of neurofibromatosis type 1. *eLife* 8, e48983. <https://doi.org/10.7554/eLife.48983>.
58. Gloss, B. (2011). Generation of an inducible Slc6a3 cre transgene. MGI Direct Data Submission MGI: J:173676. <https://www.informatics.jax.org/allele/MGI:5049906>.
59. Terauchi, A., Johnson-Venkatesh, E.M., Toth, A.B., Javed, D., Sutton, M.A., and Umemori, H. (2010). Distinct FGFs promote differentiation of excitatory and inhibitory synapses. *Nature* 465, 783–787. <https://doi.org/10.1038/nature09041>.
60. Umemori, H., Linhoff, M.W., Ornitz, D.M., and Sanes, J.R. (2004). FGF22 and its close relatives are presynaptic organizing molecules in the mammalian brain. *Cell* 118, 257–270. <https://doi.org/10.1016/j.cell.2004.06.025>.
61. Irizarry, R.A., Hobbs, B., Collin, F., Beazer-Barclay, Y.D., Antonellis, K.J., Scherf, U., and Speed, T.P. (2003). Exploration, normalization, and summaries of high density oligonucleotide array probe level data. *Biostatistics* 4, 249–264. <https://doi.org/10.1093/biostatistics/4.2.249>.
62. Schaeren-Wiemers, N., and Gerfin-Moser, A. (1993). A single protocol to detect transcripts of various types and expression levels in neural tissue and cultured cells: in situ hybridization using digoxigenin-labelled cRNA probes. *Histochemistry* 100, 431–440. <https://doi.org/10.1007/BF00267823>.
63. Kutner, R.H., Zhang, X.Y., and Reiser, J. (2009). Production, concentration and titration of pseudotyped HIV-1-based lentiviral vectors. *Nat. Protoc.* 4, 495–505. <https://doi.org/10.1038/nprot.2009.22>.
64. Bussey, T.J., Holmes, A., Lyon, L., Mar, A.C., McAllister, K.A., Nithianantharajah, J., Oomen, C.A., and Saksida, L.M. (2012). New translational assays for preclinical modelling of cognition in schizophrenia: the touchscreen testing method for mice and rats. *Neuropharmacology* 62, 1191–1203. <https://doi.org/10.1016/j.neuropharm.2011.04.011>.
65. Homer, A.E., Heath, C.J., Hvorslev-Eide, M., Kent, B.A., Kim, C.H., Nilsson, S.R., Alsiö, J., Oomen, C.A., Holmes, A., Saksida, L.M., et al. (2013). The touchscreen operant platform for testing learning and memory in rats and mice. *Nat. Protoc.* 8, 1961–1984. <https://doi.org/10.1038/nprot.2013.122>.
66. Brigman, J.L., Daut, R.A., Wright, T., Gunduz-Cinar, O., Graybeal, C., Davis, M.I., Jiang, Z., Saksida, L.M., Jinde, S., Pease, M., et al. (2013). GluN2B in corticostriatal circuits governs choice learning and choice shifting. *Nat. Neurosci.* 16, 1101–1110. <https://doi.org/10.1038/nn.3457>.
67. Toth, A.B., Terauchi, A., Zhang, L.Y., Johnson-Venkatesh, E.M., Larsen, D.J., Sutton, M.A., and Umemori, H. (2013). Synapse maturation by activity-dependent ectodomain shedding of SIRP $\alpha$ . *Nat. Neurosci.* 16, 1417–1425. <https://doi.org/10.1038/nn.3516>.
68. Dhamne, S.C., Silverman, J.L., Super, C.E., Lammers, S.H.T., Hameed, M.Q., Modi, M.E., Copping, N.A., Pride, M.C., Smith, D.G., Rotenberg, A., et al. (2017). Replicable in vivo physiological and behavioral phenotypes of the Shank3B null mutant mouse model of autism. *Mol. Autism* 8, 26. <https://doi.org/10.1186/s13229-017-0142-z>.
69. Patriarchi, T., Cho, J.R., Merten, K., Howe, M.W., Marley, A., Xiong, W.H., Folk, R.W., Broussard, G.J., Liang, R., Jang, M.J., et al. (2018). Ultrafast neuronal imaging of dopamine dynamics with designed genetically encoded sensors. *Science* 360, eaat4422. <https://doi.org/10.1126/science.aat4422>.
70. Schroeder, A., Vanderlinden, J., Vints, K., Ribeiro, L.F., Vennekens, K.M., Gounko, N.V., Wierda, K.D., and de Wit, J. (2018). A modular organization of LRR protein-mediated synaptic adhesion defines synapse identity. *Neuron* 99, 329–344.e7. <https://doi.org/10.1016/j.neuron.2018.06.026>.
71. González-Rodríguez, P., Zampese, E., Stout, K.A., Guzman, J.N., Ilijic, E., Yang, B., Tkatch, T., Stavarache, M.A., Wokosin, D.L., Gao, L., et al. (2021). Disruption of mitochondrial complex I induces progressive parkinsonism. *Nature* 599, 650–656. <https://doi.org/10.1038/s41586-021-04059-0>.

## STAR★METHODS

## KEY RESOURCES TABLE

REAGENT or RESOURCE	SOURCE	IDENTIFIER
<b>Antibodies</b>		
Mouse IgG2a monoclonal anti-bassoon antibody	Enzo Life Sciences	ADI-VAM-PS003; RRID: AB_10618753
Mouse IgG2b monoclonal anti-BMP receptor-II antibody	R&D Systems	MAB811-SP; RRID: AB_2259481
Goat anti-calbindin antibody	Nittobo Medical	Calbindin-Go-Af1040
Mouse IgG1 monoclonal anti-DARPP-32 Antibody	BD Transduction Laboratories	611520; RRID: AB_398980
Guinea pig polyclonal anti-GIRK2 antibody	Nittobo Medical	GIRK2-GP-Af830
Guinea pig polyclonal anti-dopamine receptor-1 antibody	Nittobo Medical	D1R-GP-Af500
Rabbit pig polyclonal anti-dopamine receptor-2 antibody	Nittobo Medical	D2R-Rb-Af750
Rabbit polyclonal anti-phospho-Smad1 antibody	Cell Signaling	13820; RRID: AB_2493181
Rabbit polyclonal anti-phospho-Smad2 antibody	EMD Millipore	AB3849; RRID: AB_177440
Rabbit polyclonal anti-phospho-Smad2 antibody	Cell signaling	Cat# 3108; RRID: AB_490941
Rabbit polyclonal anti-TGF $\beta$ receptor I-antibody	Sigma-Aldrich	SAB4502958; RRID: AB_10746304
Mouse IgG1 monoclonal anti-tyrosine hydroxylase antibody	Sigma-Aldrich	T2928; RRID: AB_477569
Mouse IgG2a monoclonal anti-tyrosine hydroxylase antibody	EMD Millipore	MAB5280; RRID: AB_2201526
Mouse monoclonal anti-tyrosine hydroxylase antibody, clone LNC1	Sigma-Aldrich	MAB318; RRID: AB_2201528
Rabbit polyclonal anti-VGAT antibody	Synaptic Systems	131 003; RRID: AB_887869
Guinea pig polyclonal anti-VGLUT1 antibody	EMD Millipore	AB5905; RRID: AB_2301751
Guinea pig polyclonal anti-VGLUT2 antibody	EMD Millipore	AB2251-I; RRID: AB_2665454
Rabbit polyclonal anti-VMAT2 antibody	Synaptic Systems	138 302; RRID: AB_887888
Rabbit polyclonal anti-VMAT2 antibody	Nittobo Medical	VMAT2-Rb-Af720
Alexa 488-conjugated donkey-anti-mouse IgG	Invitrogen	A-21202; RRID: AB_141607
Alexa 488-conjugated goat-anti-mouse IgG	Invitrogen	A-11029; RRID: AB_138404
Alexa 488-conjugated goat-anti-mouse IgG2a	Invitrogen	A-21131; RRID: AB_141618
Alexa 488-conjugated goat-anti-mouse IgG2b	Invitrogen	A-21141; RRID: AB_141626
Alexa 488-conjugated goat-anti-guinea pig IgG	Invitrogen	A-11029; RRID: AB_2534088
FITC-conjugated donkey-anti-rabbit IgG	Jackson ImmunoResearch	711-095-152; RRID: AB_2315776
Alexa 568-conjugated goat-anti-guinea pig IgG	Invitrogen	A-11075; RRID: AB_141954
Alexa 568-conjugated goat-anti-rabbit IgG	Invitrogen	A-11036; RRID: AB_10563566
Alexa 594-conjugated donkey-anti-goat IgG	Invitrogen	A-11058; RRID: AB_2534105
Alexa 647-conjugated donkey -anti-mouse IgG	Invitrogen	A-31571; RRID: AB_162542
Alexa 647-conjugated donkey-anti-rabbit IgG	Invitrogen	A-31573; RRID: AB_2536183
Alexa 647-conjugated donkey-anti-goat IgG	Invitrogen	A-21447; RRID: AB_2536183
Alexa 647-conjugated donkey-anti-guinea pig IgG	Jackson ImmunoResearch	706-605-148; RRID: AB_2340476
Alexa 350-conjugated goat-anti-mouse IgG1	Invitrogen	A-21120; RRID: AB_2535763
Alkaline-phosphatase-conjugated sheep anti-digoxigenin antibody	MilliporeSigma	11093274910; RRID: AB_2734716
POD-conjugated sheep anti-digoxigenin antibody	MilliporeSigma	11207733910; RRID: AB_514500
<b>Bacterial and virus strains</b>		
Lentivirus-scramble shRNA-GFP	This paper	N/A
Lentivirus- <i>Bmp6</i> shRNA-GFP	This paper	N/A
Lentivirus- <i>Bmp2</i> shRNA-GFP	This paper	N/A
Lentivirus- <i>Tgfb2</i> shRNA-GFP	This paper	N/A

(Continued on next page)

**Continued**

REAGENT or RESOURCE	SOURCE	IDENTIFIER
AAV-Syn-BMP6	This paper	N/A
AAV-Syn-BMP2	This paper	N/A
AAV-Syn-TGF $\beta$ 2	This paper	N/A
AAV2/1-DIO-Matrix-dAPEX2	Boston Children's Hospital Viral Core	Zhang et al. <sup>29</sup>
AAV2/9-GRAB <sub>DA2m</sub>	Boston Children's Hospital Viral Core	Sun et al. <sup>30</sup>
AAV2/9-rTH-Cre	Addgene	Robinson et al. <sup>57</sup> ; Cat# 107788
AAV2/9-Syn-DIO-mCherry	Boston Children's Hospital Viral Core	Halbout et al. <sup>40</sup>

**Chemicals, peptides, and recombinant proteins**

Recombinant human BMP6	PeproTech	Cat# 120-06
Recombinant human BMP2	PeproTech	Cat# 120-02
Recombinant human TGF $\beta$ 2	PeproTech	Cat# 100-35B
Recombinant human BMP6/BMP2	R&D Systems	Cat# 7145-BP-010
BMPR inhibitor (LDN193189)	Sigma-Aldrich	Cat# SML0559-5MG
TGF $\beta$ R inhibitor (SB525334)	Selleck Chemicals	Cat# S1476
PPD (para-phenylenediamine)	Sigma-Aldrich	Cat# P6001-50G
Fluoromount-G	Electron Microscopy Sciences	Cat# 17984-25
Neg 50 embedding medium	Thermo Fisher Scientific	Cat# 6502
Isoflurane	Patterson Veterinary	Cat# 14043-704-05
EMLA cream (Lidocaine/Prilocaine 2.5-2.5%)	Fougera & Co	N/A
Microcon-30kDa centrifugal filter unit	MilliporeSigma	Cat# MRCF0R030
Microcon-10kDa centrifugal filter unit	MilliporeSigma	Cat# MRCPR010
RNeasy Mini kit	Qiagen	Cat# 74104NB
NucleoSpin RNA plus	Takara	Cat# 740984.50
High-capacity cDNA reverse transcription kit	Applied Biosystems	Cat# 4368813
DIG RNA labeling mix	MilliporeSigma	Cat# 11277073910
NBT/BCIP stock solution	MilliporeSigma	Cat# 11681451001
TSA plus cyanine-3 system	PerkinElmer	Cat# NEL744001KT
RNAscope multiplex fluorescent reagent kit v2	Advanced Cell Diagnostics	Cat# 323100
<i>Mm-Smad1-C1</i> RNAscope probe	Advanced Cell Diagnostics	Cat# 524841
<i>Mm-Smad2-C2</i> RNAscope probe	Advanced Cell Diagnostics	Cat# 565191-C2
<i>Mm-Th-C4</i> RNAscope probe	Advanced Cell Diagnostics	Cat# 317621-C4
Opal 520	Akoya Biosciences	Cat# FP1487001KT
Opal 690	Akoya Biosciences	Cat# FP1497001KT
Trypan blue	Cytiva	Cat# SV30084.01
3,3'-diaminobenzidine tetrahydrochloride hydrate (DAB)	Sigma-Aldrich	Cat# D5637
D-amphetamine hemisulfate salt	Sigma-Aldrich	Cat# A5880-1G

**Critical commercial assays**

Affymetrix® rat gene 1.1 ST array strip	Affymetrix	Cat# 901627
Real-Time PCR detection system	Bio-Rad	CFX96

**Experimental models: Cell lines**

HEK 293TT	National Cancer Institute	Cat# NCI-293TT
HEK 293	ATCC	Cat# CRL-1573

**Experimental models: Organisms/strains**

Rat: Sprague Dawley	Envigo	Cat# SD
---------------------	--------	---------

(Continued on next page)



**Continued**

REAGENT or RESOURCE	SOURCE	IDENTIFIER
Rat: Sprague Dawley	Charles River	Cat# 001
Mouse: <i>DAT-CreER</i> mouse (C57BL/6-Tg(Slc6a3-icre/ERT2)2Gloss/J)	Gloss <sup>58</sup> The Jackson Laboratory	RRID: IMSR_JAX:016583
Mouse: <i>Aldh111-CreER</i> mouse (FVB-Tg(Aldh111-cre/ERT2)1Khakh/J)	Srinivasan et al. <sup>34</sup> The Jackson Laboratory	RRID: IMSR_JAX:029655
Mouse: <i>Smad1<sup>flox/flox</sup></i> mouse (B6;129-Smad1 <sup>tm1Abr</sup> /J)	Huang et al. <sup>27</sup> The Jackson Laboratory	RRID: IMSR_JAX:008366
Mouse: <i>Smad2<sup>flox/flox</sup></i> mouse (Smad2 <sup>tm1.1</sup> Epb/J)	Ju et al. <sup>28</sup> The Jackson Laboratory	RRID: IMSR_JAX:022074

**Oligonucleotides**

Forward primer for generating the <i>Bmp6</i> plasmid for <i>in situ</i> hybridization 5'- AGCAATCTGTGGGTGGTGAC -3'	This paper	N/A
Reverse primer for generating the <i>Bmp6</i> plasmid for <i>in situ</i> hybridization 5'- TGC GCAGCATGGTTTGGGGA -3'	This paper	N/A
Forward primer for generating the <i>Bmp2</i> plasmid for <i>in situ</i> hybridization 5'- GTCCTCAGCGAGTTTGAGTT -3'	This paper	N/A
Reverse primer for generating the <i>Bmp2</i> plasmid for <i>in situ</i> hybridization 5'- GAGACCAGCTGTGTTTCATCTT -3'	This paper	N/A
Forward primer for generating the <i>Tgfb2</i> plasmid for <i>in situ</i> hybridization 5'- TATCTCCACGTTGGGAACGC -3'	This paper	N/A
Reverse primer for generating the <i>Tgfb2</i> plasmid for <i>in situ</i> hybridization 5'- GGAGGGGAAGTGGGACGGCA -3'	This paper	N/A
Forward primer for <i>Bmp6</i> RT-PCR 5'- AGCAATCTGTGGGTGGTGAC -3'	This paper	N/A
Reverse primer for <i>Bmp6</i> RT-PCR 5'- TGC GCAGCATGGTTTGGGGA -3'	This paper	N/A
Forward primer for <i>Bmp2</i> RT-PCR 5'- GTCCTCAGCGAGTTTGAGTT -3'	This paper	N/A
Reverse primer for <i>Bmp2</i> RT-PCR 5'- GAGACCAGCTGTGTTTCATCTT -3'	This paper	N/A
Forward primer for <i>Tgfb2</i> RT-PCR 5'- TATCTCCACGTTGGGAACGC -3'	This paper	N/A
Reverse primer for <i>Tgfb2</i> RT-PCR 5'- GGAGGGGAAGTGGGACGGCA -3'	This paper	N/A
Forward primer for $\beta$ -actin RT-PCR 5'- CATCACTATTGGCAACGAGC -3'	This paper	N/A
Reverse primer for $\beta$ -actin RT-PCR 5'- ACTCATCGTACTCTGCTTG -3'	This paper	N/A
Sequence of <i>Bmp6</i> -shRNA ACGCCAGCGACACCACAAGGAGTTCAAGT	This paper	N/A
Sequence of <i>Bmp2</i> -shRNA GGAGAAGCCAGGTGTCTCCAAGAGACATG	This paper	N/A
Sequence of <i>Bmp2</i> -shRNA CAGGTCTTTGCACCAAGATGAACACAGCT	This paper	N/A
Sequence of <i>Tgfb2</i> -shRNA ACAGGTGTATAAGTGGAGACCAATACTT	This paper	N/A

(Continued on next page)

**Continued**

REAGENT or RESOURCE	SOURCE	IDENTIFIER
Sequence of <i>Tgfb2</i> -shRNA TGACCATCCTCTACTACATTGGCAATACG	This paper	N/A
Sequence of scramble-shRNA GCACTACCAGAGCTAACTCAGATAGTACT	OriGene	Cat# TR30015
Forward primer for <i>Bmp6</i> qPCR 5'- CCACCCAGTCGCAGGACGTG -3'	This paper	N/A
Reverse primer for <i>Bmp6</i> qPCR 5'- TGCGCAGCATGGTTTGGGGA -3'	This paper	N/A
Forward primer for <i>Bmp2</i> qPCR 5'- TTGGCCTGAAGCAGAGACC -3'	This paper	N/A
Reverse primer for <i>Bmp2</i> qPCR 5'- CTCCTGCATTTGTTCCCG -3'	This paper	N/A
Forward primer for <i>Tgfb2</i> qPCR 5'- GAGAAGGCAAGCCGGAGGGC -3'	This paper	N/A
Reverse primer for <i>Tgfb2</i> qPCR 5'- GAGACATCGAAGCGGACGAT -3'	This paper	N/A
Forward primer for $\beta$ -actin qPCR 5'- TGAGAGGGAAATCGTGCCTGACAT -3'	This paper	N/A
Reverse primer for $\beta$ -actin qPCR 5'- ACTCCTGCTTGCTGATCCACATCT -3'	This paper	N/A
<b>Recombinant DNA</b>		
pGEM-T easy vector	Promega	Cat# A1360
HuSH pRFP-C-RS	OriGene	Cat# TR30014
HuSH pRFP-C-RS containing the scramble shRNA cassette	OriGene	Cat# TR30015
<b>Software and algorithms</b>		
ImageJ	NIH	<a href="https://imagej.net/">https://imagej.net/</a> RRID:SCR_003070
Fiji	NIH	<a href="https://imagej.net/Fiji">https://imagej.net/Fiji</a> RRID:SCR_002285
cellSens	Olympus	<a href="https://www.olympus-lifescience.com/en/software/cellsens/">https://www.olympus-lifescience.com/en/software/cellsens/</a> RRID:SCR_016238
BZ analyzer software	KEYENCE	<a href="https://www.keyence.com/ss/products/microscope/bz-x800_research/">https://www.keyence.com/ss/products/microscope/bz-x800_research/</a>
EthoVision XT 11.5	Noldus	<a href="https://www.noldus.com/ethovision">https://www.noldus.com/ethovision</a> RRID:SCR_000441
ABET II Touch software	Lafayette Instrument Company	<a href="https://lafayetteneuroscience.com/products/abetii-touch-screen-software">https://lafayetteneuroscience.com/products/abetii-touch-screen-software</a>
MetaMorph	Molecular Devices	<a href="https://www.moleculardevices.com/">https://www.moleculardevices.com/</a> RRID:SCR_002368
MATLAB	Mathworks	<a href="https://www.mathworks.com">https://www.mathworks.com</a>
Prism 8	GraphPad Software	<a href="https://www.graphpad.com/scientific-software/prism/">https://www.graphpad.com/scientific-software/prism/</a>
Synapse on Dendrite Quantifier v2 ImageJ Plugin	This paper	<a href="http://faculty.cs.niu.edu/~zhou/tool/Synapse_on_Dendrite/">http://faculty.cs.niu.edu/~zhou/tool/Synapse_on_Dendrite/</a>
Clampex 10.7	Molecular Devices	<a href="https://www.moleculardevices.com/products/axon-patch-clamp-system/acquisition-and-analysis-software/pclamp-software-suite">https://www.moleculardevices.com/products/axon-patch-clamp-system/acquisition-and-analysis-software/pclamp-software-suite</a> RRID:SCR_011323
HCIImage Live	Hamamatsu	<a href="https://hciimage.com/hciimage-overview/hciimage-live/">https://hciimage.com/hciimage-overview/hciimage-live/</a> RRID:SCR_015041

## RESOURCE AVAILABILITY

### Lead contact

Further information and requests for resources and reagents should be directed to and will be fulfilled by the Lead Contact, Hisashi Umemori ([hisashi.umemori@childrens.harvard.edu](mailto:hisashi.umemori@childrens.harvard.edu)).

### Materials availability

shRNAs and AAVs generated in this study are available from the corresponding author on request.

### Data and code availability

- All data reported in this paper will be shared by the [lead contact](#) upon request.
- This paper does not report original code. The Synapse on Dendrite Quantifier v2 ImageJ Plugin is available at [http://faculty.cs.niu.edu/~zhou/tool/Synapse\\_on\\_Dendrite/](http://faculty.cs.niu.edu/~zhou/tool/Synapse_on_Dendrite/).
- Any additional information required to reanalyze the data reported in this paper is available from the [lead contact](#) upon request.

## EXPERIMENTAL MODEL AND STUDY PARTICIPANT DETAILS

### Animals

Sprague–Dawley rats were obtained from Envigo (Cat# SD) and Charles River (Cat# 001). *DAT-CreER* mice (RRID:IMSR\_JAX:016583, C57BL/6-Tg(Slc6a3-icre/ERT2)2Gloss/J), *Aldh-CreER* mice (RRID:IMSR\_JAX: 029655, B6;FVB-Tg(Aldh1l1-cre/ERT2)1Khakh/J), *Smad1<sup>flox/flox</sup>* mice (RRID:IMSR\_JAX:008366, B6;129-Smad1<sup>tm1Abr</sup>/J), and *Smad2<sup>flox/flox</sup>* mice (RRID:IMSR\_JAX:022074, *Smad2<sup>tm1.1Epb</sup>*)<sup>27,28,34,58</sup> were obtained from Jackson Laboratory. Both male and female rodents were used for both *in vitro* and *in vivo* studies except for the fiber photometry experiments (Figures 5Q–5V), open field test (Figure 6A), operant conditioning test (Figures 6D–6J), and imaging with adult *SmadCKO* mice (Figures S3E–S3K), where only male mice were used. Rats were housed in OptiRAT cages (one pregnant rat or one dam with a litter per cage) and mice in OptiMICE cages (4–5 mice per cage, except for fiber photometry where mice were singly housed), both with a 12-h/12-h light/dark cycle. The housing room temperature was  $22 \pm 1^\circ\text{C}$ . Rats and mice were allowed ad libitum access to food and water. Experiments were performed at 0–180 days of age in animals. All animal care and experiments were performed in accordance with the institutional guidelines and approved by the Institutional Animal Care and Use Committees at Boston Children's Hospital and the University of Michigan.

## METHOD DETAILS

### Primary neuronal cultures

For midbrain neuronal cultures, the ventral midbrain region that includes the SNc and VTA was dissected from P0 rats in 1 x Hank's balanced salt solution (HBSS; Gibco). The ventral midbrain pieces were pooled and incubated in dissociation media (82 mM Na<sub>2</sub>SO<sub>4</sub>, 30 mM K<sub>2</sub>SO<sub>4</sub>, 5.8 mM MgCl<sub>2</sub>, 0.25 mM CaCl<sub>2</sub>, 1 mM HEPES, 20 mM glucose, 0.001% phenol red, 1 mM cysteine, 10 units/ml papain; pH was adjusted to 7.0 with NaOH) at 37°C for 30 minutes. This was followed by trituration of the tissues in HBSS. The cell suspension was then centrifuged, and  $4.8\text{--}5.5 \times 10^4$  midbrain cells were plated on a poly-D-lysine coated round glass coverslip (diameter 12 mm, No.1, Carolina Biological) and cultured in Neurobasal-A medium (Invitrogen) supplemented with B27 (Invitrogen) or NeuralQ basal medium (Sigma-Aldrich) supplemented with GS21 (MTI-GlobalStem). In our cultures, 44.9% of dopamine neurons (TH-positive) are labeled with calbindin-only, 38.4% of dopamine neurons are labeled with GIRK2 only, and only 4.75% of dopamine neurons are labeled with both Calbindin and GIRK2. These cultures were used to examine the differentiation of dopaminergic presynaptic terminals.

For striatal neuronal cultures to test the knockdown efficiency of shRNAs, striata were dissected from P0 rats in HBSS and dissociated in a solution containing 0.5% trypsin and 0.02% DNase I, as described previously.<sup>59</sup>  $7.5 \times 10^5$  cells were then plated on a poly-D-lysine coated 35 mm tissue culture petri-dish (Falcon). These cells were cultured in Neurobasal-A medium supplemented with B27 or NeuralQ basal medium supplemented with GS21.

### Brain extract preparation

Preparation of brain extracts was described previously.<sup>60</sup> Briefly, striata from different age groups of rats (P4, P7, and P10) or distinct brain regions (striatum, cerebellum, thalamus, CPU, and NAc) from P7 rats were dissected, weighed, and homogenized in 10 volumes/weight of 400 mM NaCl, 1 mM EDTA, 10 mM Tris (pH 7.4). The dissection of the CPU and NAc used in this study is described in Figure S1C. The homogenates were centrifuged at  $15,000 \times g$  at 4°C for 15 min, and the supernatants were used as brain extracts. The P7 striatum extract was size fractionated using centrifugal filter units, Microcon-30kDa and Microcon-10kDa (MilliporeSigma). Brain extracts (1/50 volume of culture medium) were applied to midbrain cultures at 4 DIV.

## Factors

BMP6 (Peprotech Cat# 120-06), BMP2 (Peprotech Cat# 120-02), BMP6/2 (R&D Systems Cat# 7145-BP-010), and TGF $\beta$ 2 (Peprotech Cat# 100-35B) were used for *in vitro* experiments. Concentrations of the factors used were: 10 ng/ml of BMP6 and BMP2, and 2 ng/ml of TGF $\beta$ 2 in Figures 2H and 2I; 5 ng/ml of BMP6, BMP2, and BMP6/2 in Figure 2J; 5 ng/ml of BMP6/2 and 2 ng/ml of TGF $\beta$ 2 in Figure 2K; 3 ng/ml of BMP6/2, and 4 ng/ml (indicated as 2x) and 10 ng/ml (5x) of TGF $\beta$ 2 in Figure 2L; 1 ng/ml of TGF $\beta$ 2, and 20 ng/ml (2x) and 50 ng/ml (5x) of BMP6/2 in Figure 2M.

## Microarray

For microarray analysis, the CPu (18–23 mg) and NAc (7–10 mg) were dissected from the P7 rat striatum (Figure S1C). Four samples of both CPu and NAc tissues were obtained from 4 rats. Total RNA was prepared from each sample using the RNeasy Mini kit (Qiagen), and its quality was verified with Agilent 2100 BioAnalyzer. Microarray was performed using Affymetrix GeneChip Rat Gene 1.1 ST Array Strips. Genes with an expression value of 2<sup>4</sup> or greater were chosen for analysis.<sup>61</sup>

## In situ hybridization

*In situ* hybridization with digoxigenin (DIG)-labeled probes was performed as described.<sup>62</sup> DIG-labeled cRNA probes were generated by *in vitro* transcription using a DIG RNA labeling mix (MilliporeSigma). The templates for *Bmp6*, *Bmp2*, and *Tgfb2* *in vitro* transcription were generated by subcloning a part of rat *Bmp6* cDNA (498 bp), *Bmp2* cDNA (628 bp), and *Tgfb2* cDNA (550 bp) into pGEM-T Easy vector (Promega). The following primers were used for the subcloning of: rat *Bmp6*: BMP6-forward, 5'-AGCAATCTGTGGGTGGTGAC-3' and BMP6-reverse, 5'-TGCGCAGCATGGTTTGGGA-3'; *Bmp2*: BMP2-forward, 5'-GTCCTCAGCGAGTTTGAGTT-3' and BMP2-reverse, 5'-GAGACCAGCTGTGTTTCATCTT-3'; and *Tgfb2*: TGF $\beta$ 2-forward, 5'-TATCTCCACGTTGGGAACGC-3' and TGF $\beta$ 2-reverse, 5'-GGAGGGGAAGTGGGACGGCA-3'. The hybridized DIG-labeled *Bmp6*, *Bmp2*, or *Tgfb2* probe was detected by alkaline-phosphatase-conjugated sheep anti-DIG antibody (MilliporeSigma) followed by the NBT-BCIP detection system (MilliporeSigma). For fluorescence *in situ* hybridization followed by immunostaining, hybridized DIG-labeled *Bmp6*, *Bmp2*, or *Tgfb2* probe was detected by POD-conjugated sheep anti-DIG antibody (MilliporeSigma) followed by the TSA Plus Cyanine-3 system (PerkinElmer). Sections were then incubated with monoclonal anti-DARPP32 (1:1000, BD Biosciences, Cat#611520) followed by Alexa Fluor 488-conjugated anti-mouse IgG. *In situ* images were taken with a Nikon Coolpix 990 digital camera attached to an epifluorescence microscope (Olympus, BX61) under bright-field optics with 10x (Figure 2B) or 40x (Figure 2C) objective lens. The intensities of *in situ* signals were quantified with ImageJ (National Institute of Health). Images of fluorescence *in situ* hybridization were taken on an epifluorescence microscope with 40x objective lens (Olympus BX61). 12-bit images at a 1,376 x 1,032 pixel resolution were acquired using an XM10 monochrome camera (Olympus) (Figure 2G).

*In situ* hybridization with the RNAscope technology was performed using the RNAscope Multiplex Fluorescent Reagent Kit v2 (Advanced Cell Diagnostics). The probes used were *Mm-Smad1-C1*, *Mm-Smad2-C2*, and *Mm-Th-C4* RNAscope probes (Advanced Cell Diagnostics; Cat#524841, 565191-C2, and 317621-C4). P10 *Smad1cKO*, *Smad2cKO* and control mice were decapitated, and their brains were removed and immediately frozen in Neg 50 embedding medium (Thermo Fisher Scientific). Brains were sectioned at 16- $\mu$ m thickness using a cryostat (Leica Microsystems, CM3050S), and sections were mounted onto Diamond White Glass Charged Microscope Slides (Globe Scientific). Sections were fixed with 4% PFA in PBS for 15 min at 4°C, dehydrated in an ethanol dilution series, and air-dried. Sections were then treated with hydrogen peroxide for 10 min at room temperature, rinsed with MilliQ water, treated with Protease IV for 15 min at room temperature, and rinsed in PBS. Subsequently, sections were incubated with *Mm-Smad1-C1* and *Mm-Th-C4* (for *Smad1cKO* and control mice) or *Mm-Smad2-C2* and *Mm-Th-C4* (for *Smad2cKO* and control mice). Slides were incubated with the probes for 2 hours at 40°C in a HybEZ oven (Advanced Cell Diagnostics) and treated with the amplifier series (AMP1 for 30 min; AMP2 for 30 min; AMP3 for 15 min). Next, each channel's signal was developed (C1 and C4 for *Smad1cKO*; C2 and C4 for *Smad2cKO*) by treating sections with appropriate HRP reagents (HRP-C1, C2, or C4) for 15 min at 40°C, followed by appropriate Opal fluorophore reagents (Opal 690 for C1 and C2 [1:500 dilution] and Opal 520 for C4 [1:2500 dilution], Akoya Biosciences) for 30 min at 40°C. Sections were then treated with HRP blocker for 15 minutes at 40°C. Sections were washed with Wash Buffer between all incubation steps (2 min/wash). Finally, sections were stained with DAPI and mounted with Fluoromount-G (Electron Microscopy Sciences).

## RT-PCR

Total mRNA was extracted from the CPu or NAc from rats at different ages (P0, P4, P7, P10, P14 and P21) using NucleoSpin RNA Plus (Takara). cDNA was then generated using High-capacity cDNA reverse transcription kit (Applied Biosystems). The following primers were used for RT-PCR for: *Bmp6*: BMP6-forward, 5'-AGCAATCTGTGGGTGGTGAC-3' and BMP6-reverse, 5'-TGCGCAGCATGGTTTGGGA-3'; *Bmp2*: BMP2-forward, 5'-GTCCTCAGCGAGTTTGAGTT-3' and BMP2-reverse, 5'-GAGACCAGCTGTGTTTCATCTT-3'; *Tgfb2*: TGF $\beta$ 2-forward, 5'-TATCTCCACGTTGGGAACGC-3' and TGF $\beta$ 2-reverse, 5'-GGAGGGGAAGTGGGACGGCA-3'; and  $\beta$ -actin:  $\beta$ -actin forward, 5'-CATCACTATTGGCAACGAGC-3' and  $\beta$ -actin reverse, 5'-ACTCATCGTACTCCTGCTTG-3'. The intensities of amplified bands were quantified and analyzed using Fiji (National Institute of Health). For quantification, the band intensities were first normalized to those of  $\beta$ -actin. Then, the mRNA level from each age was normalized to that of P0 NAc (*Bmp6* and *Bmp2*) or P0 CPu (*Tgfb2*).



### Immunostaining

For immunostaining of brain sections, rats and mice were perfused with 4% paraformaldehyde (PFA) in PBS. Their brains were further fixed in 4% PFA in PBS overnight, immersed in 30% sucrose in PBS, and frozen in Neg 50 embedding medium (Thermo Fischer Scientific). Coronal sections were prepared using a cryostat (16- $\mu$ m thick) onto coated microscope slides (VWR). For VMAT2 staining, slides were incubated for five minutes at 30°C in a solution of pepsin (DAKO, S3002) in 0.2 N HCl (1 mg/ml HCl) prior to staining. For immunostaining of cultures, cells were fixed with 4% PFA for 15 min at 37°C as described previously.<sup>59</sup> For immunostaining of midbrain cultures with anti-calbindin antibody, cells were fixed with 4% PFA / 0.05% glutaraldehyde for 15 min at 37°C followed by a treatment with 100% methanol for 2 min at -20°C. For immunostaining of midbrain cultures with anti-GIRK2 antibody, cells were fixed with 1% PFA / 0.05% glutaraldehyde for 10 min at 37°C followed by a treatment with 100% methanol for 2 min at -20°C. After fixation, sections and cultures were incubated with blocking buffer (2% BSA, 2% goat serum, 0.1% Triton X-100 in PBS) for 30 min at room temperature, incubated with primary antibodies in 0.1% Triton X-100 in PBS for overnight at 4°C, and then incubated with secondary antibodies in 0.1% Triton X-100 in PBS for 1 hr at room temperature. For immunostaining with goat anti-calbindin antibodies, 2% BSA, 0.1% Triton X-100 in PBS was used as the blocking buffer. For immunostaining of brain sections with phospho-Smad antibodies, slides were treated with 0.3–0.5% Triton X-100 in PBS for 10 min at room temperature, incubated with blocking buffer, and then incubated with phospho-Smad antibodies for 2 hrs at room temperature. DAPI (Sigma-Aldrich) was added to each section as a nuclear stain. Stained slides were mounted with 0.5 % p-Phenylenediamine (PPD) in 20 mM Tris, pH 8.8 with 90 % glycerol (non-fluorescent) or Fluoromount-G (Electron Microscopy Sciences). Dilutions and sources of primary antibodies are: mouse anti-bassoon (1:400; Enzo Life Sciences, Cat# ADI-VAM-PS003), mouse anti-BMPR (anti-BMPRII; 1:300; R&D systems, Cat# MAB811-SP), goat anti-calbindin (1:500; Nittobo Medical, Cat# Calbindin-Go-Af1040), guinea pig anti-GIRK2 (1:400; Nittobo Medical, Cat# GIRK2-GP-Af830), guinea pig anti-dopamine receptor-1 (anti-D1R; 1:1000; Nittobo Medical, Cat# D1R-GP-Af500), rabbit anti-dopamine receptor-2 (anti-D2R; 1:1000; Nittobo Medical, Cat# D2R-Rb-Af750), rabbit anti-phospho-Smad1 (1:400; Cell Signaling; #13820), rabbit anti-phospho-Smad2 (1:400; EMD Millipore, Cat# AB3849), rabbit anti-phospho-Smad2 (1:500; Cell signaling, Cat# 3108), rabbit anti-TGF $\beta$ R (anti-TGF $\beta$ RI; 1:300; Sigma-Aldrich, Cat# SAB4502958), mouse anti-tyrosine hydroxylase (1:3000 for culture, 1:80000 for brain sections, Sigma-Aldrich, Cat# T2928), mouse anti-tyrosine hydroxylase (1:2500, EMD Millipore, Cat# MAB5280), mouse anti-tyrosine hydroxylase, clone LNC1 (1:800, Sigma, Cat# MAB318), rabbit anti-VGAT (1:1000, Synaptic Systems, Cat#131 003), guinea pig anti-VGLUT1 (1:4000; EMD Millipore, Cat# AB5905), guinea pig anti-VGLUT2 (1:1500; EMD Millipore, Cat# AB2251-I), rabbit anti-VMAT2 (1:300, Synaptic Systems, Cat#138 302), and rabbit anti-VMAT2 (1:1500, Nittobo Medical, Cat# VMAT2-Rb-Af720). Secondary antibodies used are (1:500 dilutions): Alexa 488-conjugated donkey anti-mouse IgG (Invitrogen, Cat# A-21202), Alexa 488-conjugated goat anti-mouse IgG (Invitrogen, Cat# A-11029), Alexa 488-conjugated goat anti-mouse IgG2a (Invitrogen, Cat# A-21131), Alexa 488-conjugated goat anti-mouse IgG2b (Invitrogen, Cat# A-21141), Alexa 488-conjugated goat anti-guinea pig IgG (Invitrogen, Cat# A-11029), FITC-conjugated donkey anti-rabbit IgG (Jackson ImmunoResearch, Cat# 711-095-152), Alexa 568-conjugated goat anti-guinea pig IgG (Invitrogen, Cat# A-11075), Alexa 568-conjugated goat anti-rabbit IgG (Invitrogen, Cat# A-11036), Alexa 594-conjugated donkey anti-goat IgG (Invitrogen, Cat# A-11058), Alexa 647-conjugated donkey anti-mouse IgG (Jackson ImmunoResearch, Cat# 715-605-150), Alexa 647-conjugated donkey anti-rabbit IgG (Invitrogen, Cat# A-31573), Alexa 647-conjugated donkey anti-goat IgG (Invitrogen, Cat# A-21447), Alexa 647-conjugated donkey anti-guinea pig IgG (Jackson ImmunoResearch, Cat# 706-605-148), and Alexa 350-conjugated goat anti-mouse IgG1 (Invitrogen, Cat# A-21120).

### Imaging

Fluorescent images were taken on epifluorescence microscopes (Olympus BX61: [Figure 1A](#); Olympus BX63: [Figure S1A](#); Keyence BZ-X810: [Figures 1G, 4E, 5I, 5J, and S4A–S4G](#)) and confocal microscopes (Olympus FV1000: [Figures 1D–1F](#); Zeiss LSM700: [Figures 1I–1L, 2H, 2J–2M, 3, 4A–4D, 4F, 4H–4K, 4N–4Q, 5A–5G, S3E–S3K, S4J–S4M, S5, and S7](#)). With the Olympus BX61 epifluorescence microscope, 12-bit images at a 1,376 x 1,032 pixel resolution were acquired with a 20x objective lens using an XM10 monochrome camera (Olympus). With the Olympus BX63 epifluorescence microscope, 12-bit images at a 1,376 x 1,038 pixel resolution were acquired with a 20x objective lens using an F-View II CCD camera (Soft Imaging System). With the Keyence BZ-X810 epifluorescence microscope, 8-bit images at a 960 x 720 ([Figures 1G and S4A–S4G](#)), 5018 x 1733 ([Figure 4E](#)), or 6432 x 4759 ([Figures 5I and 5J](#)) pixel resolution were acquired with a 20x ([Figures 1G, 4E, and S4A–S4G](#)) or 10x ([Figures 5I and 5J](#)) objective lens. With confocal microscopes, 12-bit (FV1000) or 8-bit (LSM700) images at a 1,024 x 1,024 pixel resolution were obtained using 25x, 40x and 63x objective lenses with a 0.5x, 1.0x, 1.2x, or 1.5x zoom. Images were acquired as a Z-stack (12–25 optical sections; 0.8  $\mu$ m (25x objective lens), 0.45  $\mu$ m (40x objective lens), or 0.35  $\mu$ m (63x objective lens) step size). Images in the same set of experiments were acquired with identical acquisition settings regarding the exposure time, laser power, detector gain, and amplifier offset for each wavelength.

The intensity of stained signals, and the size and density of stained puncta were quantified and analyzed using MetaMorph software (Molecular Devices). For images of TH immunostaining from rat and mouse striatal sections, the mean staining intensity in the anterior commissure (for images of the NAc) or in the corpus callosum (for images of the CPu) was calculated as the background signal and subtracted from each image. For images of VMAT2 immunostaining from rat and mouse striatal sections, the mean

staining intensity plus five standard deviations in the anterior commissure (for images of NAc) or the mean staining intensity plus seven standard deviations in the corpus callosum (for images of rat striatum and mouse CPU) was calculated as the background signal and subtracted from each image.

To evaluate the mDA dendrite elongation in the SNr (Figures S4F–S4I), the SNr was equally divided into the proximal and distal regions from the SNc (see Figure S4E). The average TH intensities in the distal and proximal SNr regions were quantified with MetaMorph software. The intensities were normalized to the intensity in the proximal region of the control mice.

To analyze the densities of phospho-Smad on the axons of mDA neurons (TH-positive) in the striatum (Figures 4P and 4Q), the numbers of phospho-Smad puncta on TH-positive axons were divided by the total area of TH-positive axons. The numbers of phospho-Smad puncta on TH-positive axons were quantified using the Synapse on Dendrite Quantifier v2 ImageJ Plugin ([http://faculty.cs.niu.edu/~zhou/tool/Synapse\\_on\\_Dendrite/](http://faculty.cs.niu.edu/~zhou/tool/Synapse_on_Dendrite/)). For each image, the background intensity was calculated from TH-negative cell bodies. For phospho-Smad images, the cut-off intensity was set at the background intensity plus five standard deviations. For TH images, the cut-off intensity was set at the background intensity plus six standard deviations. The total area of TH-positive axons was quantified using ImageJ.

To analyze the densities of excitatory (VGLUT2-positive) and inhibitory (VGAT-positive) synapses on the dendrites of mDA neurons (TH-positive) in the SNr (Figures S4J–S4O), the numbers of VGLUT2 or VGAT puncta on TH-positive dendrites were divided by the total area of TH-positive dendrites. The numbers of VGLUT2 and VGAT puncta on TH-positive dendrites were quantified using the Synapse on Dendrite Quantifier v2 ImageJ Plugin. For each image, the background intensity was calculated from TH-negative cell bodies. For VGLUT2 and VGAT images, the cut-off intensity was set at the background intensity plus four standard deviations. For TH images, the cut-off intensity was set at the background intensity plus three standard deviations. The total area of TH-positive dendrites was quantified using ImageJ.

For images of cultured neurons stained for VMAT2 and/or bassoon, the staining intensity in the shaft of neurites in control cultures was calculated as the background signal and subtracted from each image. Puncta smaller than 4 pixels were excluded from analysis.

For images of cultured neurons treated with extracts (Figure S1A), ImageJ was used for the measurement of the length of the longest neurite of the cells.

The total intensity of the AAV-driven mCherry signal (Figures 5I and 5J) in the CPU and NAc was quantified and analyzed using ImageJ. The IsoData or Moments method was used for background subtraction in the CPU or NAc, respectively.

### shRNA constructs

The *Bmp6*, *Bmp2*, and *Tgfb2* specific shRNA expression plasmids were constructed using synthetic oligonucleotides, which were cloned into the BamHI/HindIII sites of the HuSH shRNA vector (pRFP-C-RS, OriGene). The following target sequences were used: *Bmp6*-shRNA: ACGCCAGCGACACCACAAGGAGTTCAAGT, *Bmp2*-shRNA: GGAGAAGCCAGGTGTCTCCAAGAGACATG and CAGGTCTTTGCACCAAGATGAACACAGCT, *Tgfb2*-shRNA: ACAGGTGTATAAGTGGAGACCAAATACTT and TGACCATCTCTA CTACATTGGCAATACG. The sequence for scrambled-shRNA was: GCACTACCAGAGCTAACTCAGATAGTACT. The U6 promoter and shRNA sequence from the HuSH shRNA plasmid was then subcloned into the FUGW vector, which also contains the ubiquitin promoter-driven EGFP. For *Bmp2*-shRNA and *Tgfb2*-shRNA vectors, two shRNA target sequences were inserted into the FUGW vector to increase the efficiency of *Bmp2* and *Tgfb2* knockdown.

### AAV constructs

AAV-Syn-BMP6, AAV-Syn-BMP2, and AAV-Syn-TGFβ2 plasmids, which contain the coding sequences for BMP6, BMP2, and TGFβ2, respectively, were made by RT-PCR from rat striatal RNA. To generate shRNA-resistant coding sequences, silent mutations were introduced into the shRNA target sequences using primers containing point mutations. In addition, HA tag sequences were inserted in front of the stop codon. Each primer to amplify the coding sequence includes unique restriction enzyme sites at their 3' and 5' ends (see sequences listed below). The amplification of each coding sequence was separated into two PCR fragments. After restriction enzyme digestion, these two PCR products were simultaneously cloned into BamHI/HindIII sites (for making AAV-Syn-BMP6) or BamHI/EcoRI sites (for making AAV-Syn-BMP2 and AAV-Syn-TGFβ2) of the pAAV-hSyn vector. The following primers were used for amplification of: BMP6 product1: forward, 5'-TACCGGATCCGCCACCATGCCCGGGCTGGGGCGGAGGGCGC-3' and reverse, 5'-GCTGCCTAGGGGAGAACTCCTTGTCTGCTACTC-3'; BMP6 product2: forward, 5'-CTCCCTAGGCAAAGGCAT CATAAAGAATTCAAGT-3' and reverse, 5'-TCACAAGCTTTCATGCAACATCTGGGACATCGTATGGGTAATGACATCCACAAGC TCT-3'; BMP2 product1: forward, 5'-GGAAGGATCCGCCACCATGGTGGCCGGGACCCGCTGTCTTCTA-3' and reverse, 5'-CCG AAGGCCTTGACAAGGGGCGGCCGGATG-3'; BMP2 product2: forward, 5'-GTCAAGGCCTTCGGACGACGTCCTCAGCGAGTT TGAGTTGA-3' and reverse, 5'-TCTGGAGCTCCGCAGATGTGAGAACTCATCAGTAGG-3'; TGFβ2 product1: forward, 5'-TACC AGATCTGCCACCATGCACTACTGTGTGCTGAGAAC-3' and reverse, 5'-GTGGCTCGAGATCCTGGGACACACAGC-3'; TGFβ2 product2: forward, 5'-GGATCTCGAGCCACTCAGATTTTGTATTATATCGGAAATAC-3' and reverse, 5'-TCAAGAATTCTTATG CAACATCTGGGACATCATAAGGGTAGCTGCATTTACAAGACTTG-3'.

The constructs for AAV-DIO-Matrix-dAPEX2 (Addgene plasmid #117177),<sup>29</sup> AAV-GRAB<sub>DA</sub> (AAV-GRAB<sub>DA2m</sub>, Addgene plasmid #140553),<sup>30</sup> AAV-rTH-Cre (Addgene plasmid #107788),<sup>57</sup> and AAV-DIO-mCherry (Addgene plasmid #50459)<sup>40</sup> were described previously.

### Lentivirus and AAV preparation

Lentiviruses were generated at the Boston Children's Hospital Viral Core or by using the standard calcium phosphate transfection protocol with hygromycin B-resistant HEK 293TT cells (National Cancer Institute). Briefly, 24 hrs prior to transfection,  $2.5\text{--}3.0 \times 10^6$  HEK 293TT cells were plated on a poly-D-lysine coated 10 cm petri-dish (BD Falcon) and cultured in IMDM medium (Thermo Fisher Scientific) containing GlutaMAX (Thermo Fisher Scientific) and 10% FBS (Corning). Two hours prior to transfection, 75% of medium was replaced with fresh IMDM medium supplemented with GlutaMAX and 10% FBS. FUGW-shRNA plasmids, the delta-8.9 packaging plasmid, and the VSV-G envelope plasmid were transfected into HEK 293TT cells. Viral supernatant was harvested at 24 hrs after the transfection. New medium was then added into the dishes, and viral supernatant was again harvested 24 hrs later. Viral supernatant from the two harvests was combined and cleared with  $0.45\text{ }\mu\text{m}$  pore PVDF Millex-HV filter (Millipore). Lentivirus was concentrated with polyethylene glycol (PEG) 6000.<sup>63</sup> Precipitated lentivirus was collected by centrifugation, suspended in PBS, and stored in aliquots at  $-110^\circ\text{C}$ , or immediately used to transduce recipient cells. The titers of viruses were assessed by measuring the number of GFP-positive HEK 293 cells (ATCC) after infection with a series of diluted lentiviruses.

The efficiency of shRNA-mediated knockdown of target genes was evaluated using rat striatal cultures. Cultured neurons were infected with lentivirus expressing *Bmp6*-shRNA, *Bmp2*-shRNA, *Tgfb2*-shRNA or scrambled-shRNA at 2 DIV. 10-fold virions relative to the number of plated cells were added into the cultures (all neurons were infected as determined by co-expressed GFP, which was clearly visible by 4 DIV). At 12 DIV, mRNA from cultured cells was prepared, and *Bmp6*, *Bmp2*, and *Tgfb2* mRNA expressions were determined by quantitative PCR (qPCR) (Bio-Rad). *Bmp6*, *Bmp2*, and *Tgfb2* mRNA expression levels were normalized to  $\beta$ -actin levels. The following primers were used for qPCR of: *Bmp6*: BMP6-forward, 5'-CCACCCAGTCGCAGGACGTG-3' and BMP6-reverse, 5'-TGCGCAGCATGGTTTGGGGA-3'; *Bmp2*: BMP2-forward, 5'-TTGGCCTGAAGCAGAGACC-3' and BMP2-reverse, 5'-CTTCCTGCATTTGTTCCCG-3'; *Tgfb2*: TGF $\beta$ 2-forward, 5'-GAGAAGGCAAGCCGGAGGGC-3' and TGF $\beta$ 2-reverse: 5'-GAGACATCGAAGCGGACGAT-3'; and  $\beta$ -actin:  $\beta$ -actin forward, 5'-TGAGAGGGAAATCGTCGTGACAT-3' and  $\beta$ -actin reverse, 5'-ACTCCTGCTTGCTGATCCACATCT-3'. Knockdown efficiency was measured by the amount of target mRNA in shRNA expressing neurons relative to scramble-shRNA expressing neurons. Three independent experiments were used to measure the knockdown efficiency. The knockdown efficiency of *Bmp6*-shRNA was  $87.22 \pm 6.48\%$  (97.95%, 75.56%, and 88.14%), *Bmp2*-shRNA  $79.90 \pm 8.30\%$  (94.79%, 78.83%, and 66.08%), and *Tgfb2*-shRNA  $83.44 \pm 2.96\%$  (88.42%, 78.16%, and 83.73%).

The AAV-BMP6, AAV-BMP2, AAV-TGF $\beta$ 2, AAV-DIO-Matrix-dAPEX2, AAV-GRAB<sub>DA</sub> (AAV-GRAB<sub>DA2m</sub>), and AAV-DIO-mCherry were produced at the Boston Children's Hospital Viral Core. AAV9-rTH-Cre was obtained from Addgene (Cat# 107788).

### Stereotaxic injections to pups

Prior to stereotaxic injections, one or two pups per litter were used by dye injection (HyClone trypan blue solution (Cytiva)) to adjust for any coordinate variability between litters. Analgesic (meloxicam, 1 mg/kg s.c., or EMLA cream (lidocaine 2.5% and prilocaine 2.5%), topical skin application) was administered prior to surgery. Pups were anesthetized with ice and secured in a stereotaxic frame (Stoelting or Harvard Apparatus). A small hole was drilled on the skull above the target structure, and an injection needle (33-gauge, Plastics One) attached to a 10  $\mu\text{l}$  injection syringe (Hamilton) was inserted into the target brain region. The injection syringe was tethered to a motorized stereotaxic injector (Stoelting or Harvard Apparatus). After the surgery, pups were warmed at  $37^\circ\text{C}$  until they recovered and then were returned to a cage with a nursing mother.

For shRNA knockdown experiments (Figures 3A–3H and S2), 1.2  $\mu\text{l}$  of lentivirus suspended in PBS ( $1\text{--}1.5 \times 10^9$  Infectious Units (IFU)/ml) was delivered to the CPu or NAc of P3 rats at a constant speed (0.25  $\mu\text{l}/\text{min}$ ). The injection needle was kept in place for two min post-injection to minimize the upward flow of viral solution after removing the needle. The default coordinate for the dorsal striatum (CPu) was: AP = +1.4 mm, ML =  $\pm 1.6$  mm, DV = -3.1 mm relative to bregma, and the coordinate for the ventral striatum (NAc) was: AP = +1.55 mm, ML =  $\pm 1.25$  mm, DV = -4.3 mm the relative to bregma.

For shRNA rescue experiments (Figures 3I and 3J), 100 nl of shRNA lentivirus ( $1.0 \times 10^{11}$  genome copies (GC)/ml) was mixed with 100 nl of saline (for scrambled-shRNA), AAV-BMP6 (for *Bmp6*-shRNA), AAV-BMP2 (for *Bmp2*-shRNA), or AAV-TGF $\beta$ 2 (for *Tgfb2*-shRNA) in saline. The titer of the AAV was  $2.0 \times 10^{13}$  GC/ml. Each virus mixture was delivered to the CPu or NAc of P2 rats at a constant speed (50 nl/min). The default coordinate for the CPu was: AP = +1.47 mm, ML =  $\pm 2.20$  mm, DV = -2.93 mm relative to bregma, and the NAc was: AP = +1.50 mm, ML =  $\pm 1.24$  mm, DV = -4.05 mm relative to bregma.

For AAV-DIO-Matrix-dAPEX2 injections, 220 nl of AAV suspended in PBS ( $4 \times 10^{12}$  GC/ml) was delivered to the ventral midbrain of P4 *Smad1cKO*, *Smad2cKO*, and control mice at a constant speed (50 nl/min). The default coordinate for the ventral midbrain was: AP = -0.12 mm, ML =  $\pm 0.17$  mm, DV = -3.7 mm relative to lambda.

For the axon tracing experiment (Figures 5I–5L) and cylinder test (Figure 6C), AAV-rTH-Cre and AAV-DIO-mCherry were mixed and co-injected unilaterally into the SNc or VTA of P2 mice. 125 nl of AAV mixture suspended in PBS was delivered at a constant speed (50 nl/min), and this injection was repeated twice (total 250 nl into a hemisphere). The viral titers were: AAV9-rTH-Cre,  $5 \times 10^{12}$  GC/ml, and AAV2/9-Syn-DIO-mCherry,  $4 \times 10^{12}$  GC/ml. The default coordinates for the SNc were AP = -0.01 mm, ML = -0.89 mm, DV = -3.73 mm and AP = -0.02 mm, ML = -0.86 mm, DV = -3.74 mm relative to lambda. The default coordinates for the VTA were AP = -0.06 mm, ML = +0.15 mm, DV = -3.77 mm and AP = -0.06 mm, ML = +0.17 mm, DV = -3.75 mm relative to lambda.

For GRAB<sub>DA</sub> imaging in striatal slices (Figures 5W–5Z), 125 nl of AAV-GRAB<sub>DA</sub> suspended in PBS (6.24 × 10<sup>12</sup> GC/ml) was delivered into the CPU of P2 control and SmadCKO mice at a constant speed (50 nl/min). The injection was repeated twice (total 250 nl). The default coordinates were AP = 2.50 mm, ML = -1.28 mm, DV = -2.35 mm and AP = 2.40 mm, ML = -1.33 mm, DV = -2.30 mm relative to lambda.

### Electron microscopy

After AAV-DIO-Matrix-dAPEX2 injections at P4 and tamoxifen administrations at P18 and P19, P32 Smad1cKO, Smad2cKO and control mice were transcardially perfused with Ames' media with heparin (oxygenized with 95% O<sub>2</sub>, 5% CO<sub>2</sub>, warmed to 37°C) and then with fixative (2.5% glutaraldehyde and 2% PFA in cacodylate buffer [0.15 M sodium cacodylate and 0.04% CaCl<sub>2</sub>, pH 7.4] warmed at 37°C). Harvested brains were post-fixed in the same fixative at 4°C for overnight. The brains were then washed with cacodylate buffer and sliced with a vibratome (Leica VT1000S) into 180 μm sections in cacodylate buffer. The sections were washed for 10 min twice in cacodylate buffer containing 50 mM glycine, rinsed with cacodylate buffer for 10 min, and incubated with 0.3 mg/ml 3,3'-diaminobenzidine tetrahydrochloride hydrate (Sigma-Aldrich) in cacodylate buffer (DAB solution) in the dark for 30 min. 10 μl of cacodylate buffer containing 0.3% H<sub>2</sub>O<sub>2</sub> was then added to the DAB solution to initiate the peroxidase reaction, and the reaction proceeded in the dark for 30 min. After the reaction, the sections were rinsed in cacodylate buffer and fixed with cacodylate buffer containing 3% glutaraldehyde at 4°C at least for overnight. Images of stained sections were taken by Olympus SZ51 stereo microscope with a 1.2x zoom using PowerShot SX170 IS camera (Canon) (Figure S6B). Stained sections were washed with cacodylate buffer and osmicated in cacodylate buffer containing 2% osmium tetroxide and 2.5% potassium ferrocyanide for 60 min. Sections were then washed with ddH<sub>2</sub>O and stained in 0.05 M sodium maleate (pH 5.15) and 1% uranyl acetate at 4°C overnight. After washing with ddH<sub>2</sub>O, sections were dehydrated in graded alcohol series and propylene oxide, and infiltrated with epoxy resin mix (1:1 of TAAB Epon resin : propylene oxide) at 4°C overnight. The sections were embedded in TAAB Epon sandwiched between two layers of Aclar plastic (EMS) and polymerized at 60°C for 48 hours. After polymerization, small areas in the CPU (default size was 1.25 mm × 0.78 mm) and the NAc (default size was 1.0 mm × 0.8 mm) were cut out and glued onto blank resin blocks for sectioning. Samples were sectioned using Leica EM UC7 ultramicrotome with Diatome diamond knives, and ultra-thin sections (40–50 nm) were prepared and observed with JEOL 1200EX transmission electron microscope. The digital images were captured with AMT 2k CCD camera system (Advanced Microscopy Techniques).

Images were taken from the CPU and NAc as indicated in Figure S1C. 3,000x magnified pictures (1–4 pictures/CPU or NAc/mouse) were used for the analysis of the density of labeled mitochondria (Figure S6E) and dopaminergic presynaptic terminals (Figure S6F). Dopaminergic presynaptic terminals were defined as boutons containing a labeled mitochondrion and at least one synaptic vesicle. For the analysis of the size of dopaminergic presynaptic terminals (Figure S6G) and the synaptic vesicle density at dopaminergic presynaptic terminals (Figures 5M and 5N), 20,000x or 30,000x magnified pictures were used (17–20 pictures/CPU or NAc/mouse). The size of the dopaminergic presynaptic terminal (the area occupied by mitochondria was subtracted) was measured by Fiji. For synaptic vesicle density (Figures 5O and 5P), the number of synaptic vesicles at each dopaminergic presynaptic terminal was manually counted and divided by the size of each dopaminergic presynaptic terminal.

### Fiber photometry

For dopamine imaging with fiber photometry, adult Smad1cKO, Smad2cKO, and control mice (age: 4–6 months) were used. Mice were anesthetized with 1.5% isoflurane (Patterson Veterinary) with a constant gas flow rate of 1 L/min, then placed in a stereotaxic frame (Harvard Apparatus). A small hole was drilled on the skull above the target structure, and a 2-μl injection syringe (Hamilton) attached to a stereotaxic injector (Harvard Apparatus) was inserted into the target brain region. A total of 750 nl of AAV-GRAB<sub>DA2m</sub> suspended in PBS was delivered at a constant speed (125 nl/min). The coordinates used were as follows: CPU: AP = +1.10 mm, ML = ±1.10 mm, DV = -2.65 mm relative to bregma, and NAc: AP = +1.30 mm, ML = ±1.25 mm, DV = -4.30 mm relative to bregma.

Immediately after the virus injection, an optical fiber cannula (400-μm core, 0.48 NA; Doric Lenses) was unilaterally implanted and placed into the CPU or NAc with the coordinates used for viral delivery. Four stainless steel screws were fastened to the mouse skull around the cannula, and dental restorative filled resin (Henry Schein) and acrylic cement were applied to firmly anchor the cannula. After surgery, the mice were warmed at 37°C until they recovered and were single-housed for the duration of the experiment. Analgesic (meloxicam, 1 mg/kg s.c.) was administered daily by subcutaneous injection after surgery for 4 days.

Four weeks after optic fiber probe implantation, mice were connected from their implanted cannulas to a fiber optic patch cord (400-μm core, 0.48 NA; Doric Lenses), held in place by a zirconia sleeve. *In vivo* fiber photometry recording in both CPU and NAc was performed by delivering two light emitting diodes (50 μW at fiber tip) at 465 nm (GRAB<sub>DA</sub> stimulation wavelength) and 405 nm (control for artifact fluorescence) through the optic fiber at different sinusoidally modulated frequencies (231 Hz and 531 Hz, respectively) (LED drivers, Doric Lenses). Emitted fluorescence was collected by the same fiber, passed through a 500–550 nm emission filter (Doric Lenses), and focused onto a Newport Visible Femtowatt Photoreceiver (Model 2151) and recorded using a real-time processor (RZ5, TDT).

Real time recording was performed all through amphetamine-induced locomotor activity paradigm. Briefly, each mouse was habituated in a white square open field arena (50 × 50 cm, 30 lux) for 30 min. The mouse then received an intraperitoneal injection of saline (10 ml/kg), and the basal locomotion activity of the mouse was measured for 30 min. After the basal activity was recorded, each



mouse received three intraperitoneal injections of amphetamine (2 mg/kg; with a 15 min interval, Sigma-Aldrich), and the locomotor activity of the mouse was monitored for a total of 90 min. The movement of the mouse was captured by a CCD camera during the test. All data acquisition and analyses were carried out by an individual blind to the genotype.

The  $\Delta F/F$  of the GRAB<sub>DA</sub> emitted signal to amphetamine responses was calculated as  $(F_{\text{raw}} - F_{\text{baseline}})/F_{\text{baseline}}$  using MATLAB, with the average intensity within a 2 min window prior to the first amphetamine injection set as the normalizing  $F_{\text{baseline}}$ .

### GRAB<sub>DA</sub> imaging in striatal slices

Imaging was based on the protocol in Liu et al.<sup>31</sup> Mice were injected with AAV-GRAB<sub>DA2m</sub> at P2 and then used for GRAB<sub>DA</sub> imaging in slices between P16 and P25. Slices were made by decapitating mice, quickly removing their brains, blocking off the cerebellum, and bisecting the two cortical hemispheres. 250  $\mu\text{m}$  coronal slices were then cut using a VT1200S vibratome (Leica). Cutting was done in an ice-cold solution containing: 75 mM NaCl, 2.5 mM KCl, 7.5 mM MgSO<sub>4</sub>, 75 mM sucrose, 1 mM NaH<sub>2</sub>PO<sub>4</sub>, 12 mM glucose, 26.2 mM NaHCO<sub>3</sub>, 1 mM myo-inositol, 3 mM pyruvic acid, and 1 mM ascorbic acid. Slices were then incubated at room temperature in an incubation solution containing: 126 mM NaCl, 2.5 mM KCl, 2 mM CaCl<sub>2</sub>, 1.3 mM MgSO<sub>4</sub>, 1 mM NaH<sub>2</sub>PO<sub>4</sub>, 12 mM glucose, 26.2 mM NaHCO<sub>3</sub>, 1 mM myo-inositol, 3 mM pyruvic acid, and 1 mM ascorbic acid for a minimum of 1 hour. Recordings were performed in a recording chamber continuously perfused with artificial cerebrospinal fluid (ACSF) containing: 126 mM NaCl, 2.5 mM KCl, 2 mM CaCl<sub>2</sub>, 1.3 mM MgSO<sub>4</sub>, 1 mM NaH<sub>2</sub>PO<sub>4</sub>, 12 mM glucose, and 26.2 mM NaHCO<sub>3</sub> heated to 30–32 °C at 2 ml/min. All solutions were constantly bubbled with 95% O<sub>2</sub>/5% CO<sub>2</sub>. Fluorescence imaging was conducted with a customized Scientifica/Olympus microscope. Fluorescent signals were excited with a 470 nm LED (CoolLED), collected through a 4X objective (Olympus), and digitized through a ORCA Spark Camera (Hamamatsu). Electrical stimulation was carried out with a unipolar glass pipette (tip diameter of 3–5  $\mu\text{m}$ ) filled with ACSF. The electrode was placed in the CPU and two 0.1 ms pulses spaced by 1 sec were delivered with a stimulus intensity of 500  $\mu\text{A}$ ; stimulation was controlled using a Digidata 1440A with Clampex 10.7 (Molecular Devices) and a stimulus isolator (Warner Instruments). Data were collected with HCLImage Live 4.5 (Hamamatsu). Dopamine release was imaged at 916 x 916 pixels/frame with an exposure time of 50 ms. For image analyses,  $F_0$  was estimated as the average fluorescence signal over 0.2–0.4 s immediately before stimulation using ImageJ.  $\Delta F/F_0$  was then calculated for each pixel within a fixed, oval shape region of interest (ROI) around the stimulating electrode. Area was calculated by drawing an ROI around the area above background during peak 1.

### Behavioral tests

All data acquisition and analyses were carried out by an individual blind to the genotype. Experiments were conducted during the animals' dark cycle except the operant conditioning test, which was conducted during the animals' light cycle.

#### Open field test

2–3 months old control and SmadckKO male mice were used for the test. Each mouse was in an opaque white circular (diameter = 42 cm) open-field arena (30 lux) for 5 min. The movement of the mouse was captured by a CCD camera during the test. Captured movements were digitized and analyzed with EthoVision XT software (Noldus). The total distance traveled was quantified and evaluated.

#### Rearing test

2 months old control and SmadckKO male and female mice were used for the test. Mice were habituated in the original housing cages in the testing room for 30 min with 2 lux brightness. Then, each mouse was habituated in a rectangle Plexiglas container (length x width x height = 27 cm x 12 cm x 16 cm) with a lid in the testing room (2 lux) for 10 min. The rearing behavior of the mice was then monitored for 10 min. The movement of the mouse was captured by a portable video camera (HDC-SD60, Panasonic) during the test. Rearing was defined as both front paws lifted off the floor with an extended body and included leaning (front paws resting on the wall of the container) and free rearing (rearing with no wall support).

#### Cylinder test

2–4 months old control and unilateral-SmadckKO (unilateral inactivation of Smad) male mice were used for the test. Mice were habituated in the original housing cages in the testing room for 30 min with 2 lux brightness. Then, each mouse was placed in a transparent 2L glass beaker for 3–10 min until at least 30 rearing events were made by the mouse. The movement of the mouse was then captured by a portable video camera (HDC-SD60, Panasonic) during the test. Two mirrors were placed behind the beaker to monitor forelimb movements when the mouse turned away from the video camera. The round shape of the beaker encourages mice to make vertical exploration of the wall with the forelimbs followed by landing. No mouse climbed up to the top edge of the beaker. For scoring, the extent of the forelimb-use asymmetry was determined. In this study, the behavior during landing was scored: the percentages the mouse used both forelimbs to land or independently used the left or right forelimb to land were quantified. Replay of the video in slow motion, frame by frame, was used to quantify behavior.

#### Operant conditioning test

**Animals.** 2–3 months old control and SmadckKO male mice were used for the test. These mice are housed in groups of five mice per cage during the testing period. Food restriction was used to maintain mice at approximately 85% of their free-feeding weight throughout the experiment. Water is available ad libitum throughout the experiment. During food restriction, the daily provision of chow pellets was adjusted to keep the weight of the mice at >80% of their free-feeding weight. Weights were measured daily throughout the study.

**Touch screen apparatus.** All training and testing were conducted in Bussey-Saksida mouse touchscreen chambers (Lafayette Instruments).<sup>64,65</sup> Briefly, the touchscreen (12.1 in.; resolution 800 × 600) is surrounded by a stainless-steel floor and a trapezoidal reinforced plastic wall. A black plastic 2-window mask (the window size is 7.0 × 7.5 cm) was placed in front of the touchscreen to display an image in one of the windows, or two different images in two windows. These windows were situated at 2.0 cm above the floor. Each operant chamber was in a sound-attenuating box, fitted with a house light, a food magazine with a LED light, which illuminates coincident with reward delivery, and overhead camera to monitor and record sessions. Protocol operation, including visual stimulus presentation and reward delivery, and data analysis was conducted by ABET II Touch software (Campden Instruments). The mask, touchscreen, grid floor and tray were cleaned with 70% ethanol between animals.

**Touch screen training.** Prior to the visual discrimination and reversal learning tasks, mice were trained to use the touchscreens as follows. 1) Habituation. In this training, mice became accustomed with the chamber and reward (10% condensed milk). This training was one 60 min session per day. 200  $\mu$ L of reward was placed in the food magazine tray before the beginning of each habituation session, and mice must consume all reward within 60 min. This task took 1–2 days. 2) Magazine training. In this training, mice learned that the food magazine with the LED light on had the reward. This task was one 60 min session per day. 20  $\mu$ L of reward was delivered by a peristaltic pump into the food magazine with the LED light on. Mice required a head entry into the food magazine to obtain a reward. Upon reward collection (head entry), the LED light turned off. 30 sec after the reward collection, the LED light is turned on and another reward (20  $\mu$ L) was delivered to begin a new trial. Mice must complete 40 trials within 60 min. This task took 1–2 days. 3) Must Touch training. In this training, mice learned that a visual stimulus is associated with a reward delivery. This task was one 60 min session per day. When the trial started, a visual stimulus was displayed on one of the windows pseudo-randomly. When mice touched the visual stimulus, a tone (1000 ms, 3 kHz) was played, a reward (20  $\mu$ L) was given, and a LED light at the food chamber was turned on. Upon reward collection, the LED light was turned off, then a new trial began. Mice must complete 60 trials within 60 min to reach criterion. After these three trainings, mice were subjected to the Visual Discrimination and Reversal Learning tasks.

**Visual Discrimination (VD) and Reversal Learning (RL).** The VD task required mice to discriminate between two visual stimuli and to learn which stimulus was associated with a reward. For this task, the two images used were “fan” and “marble” patterns. The image that was associated with a reward was counterbalanced within each group but remained constant for individual mice. When a trial started, “fan” or “marble” was displayed on the left or right window pseudo-randomly. When mice touched the image associated with a reward, a tone (1000 ms, 3 kHz) was played, a reward (20  $\mu$ L) was given, and the LED light at the food chamber was turned on. Upon reward collection, the LED light was turned off, then a new trial began. When mice touched the image not associated with a reward, a different tone was played and a house light was turned on for 5 sec. Then, the LED light at the food chamber was turned on. Upon head entry into the food chamber, the LED light was turned off, then a new trial began. The VD tasks were 60 trials or for 60 min, whichever came first, per day. When the mice achieved >80% of correct responses out of 60 trials within 60 min for two consecutive days (when the fan was a rewarded image) or for three consecutive days (when the marble was a rewarded image), the VD task was completed, and the mice were moved to the RL task. For the RL task, the image associated with a reward was switched, so that the previously unrewarded image was now associated with a reward, and the previously rewarded image was now not associated with a reward. The RL tasks were 60 trials or for 60 min, whichever came first, per day. The RL task was conducted until the mice reached the criteria of >80% correct out of 60 trials within 60 min for two consecutive days (when the fan was the rewarded image) or for three consecutive days (when the marble was the rewarded image).

#### Acoustic startle response and prepulse inhibition

2–3 months old control and SmadCKO male and female mice were used for the test. Mice were habituated in the original housing cages in the testing room for 30 min.

Startle responses were measured using startle chambers (Kinder Scientific). Test sessions began by placing the mouse in the Plexiglas restrainer for a 5-min acclimation period. Next, the mouse was presented with a block of seven trials of noise. The block of trials was repeated five times (total 35 trials). The inter-trial interval was 10–20 s. One of the trials measured the startle response to the background noise (60 dB). The other six trials measured startle responses to 40 ms of sound bursts at 70, 80, 90, 100, 110, or 120 dB. The seven trials were presented in a pseudo-random order such that each trial type was presented once within a block of trials. Startle waveforms were recorded using load cell platforms, which measure the force changes during an animal's jump. Each load cell was calibrated with a 100g weight, which corresponds to 1 newton of force. The maximum startle amplitude over this sampling period was recorded. To examine the prepulse inhibition of acoustic startle response, mice were presented with prepulse stimuli, which were 20 ms tones at the 60, 70, 74, 78, or 82 dB intensity, 100 ms prior to the 110 dB startle stimulus. The five different prepulse stimuli were presented in a pseudo-random order in a block of trials. The block of trials (five different prepulse stimuli) was repeated five times (total 25 trials). The intertrial interval was 10–20 s. The maximum startle amplitude over this sampling period was recorded.

#### QUANTIFICATION AND STATISTICAL ANALYSIS

All data are expressed as mean  $\pm$  SEM. Statistical analyses were performed using GraphPad Prism software. The statistical tests performed were two-tailed Student's *t* test, one-way ANOVA, and two-way repeated-measures ANOVA as indicated in the figure legends. One-way ANOVA were followed by Tukey's or Bonferroni's *post hoc* test. Sample sizes (*n*) are indicated in the figure legends. Sample sizes were similar to those reported in previous publications.<sup>59,66–71</sup> Significance was set as \**P* < 0.05, \*\**P* < 0.01 and

\*\*\*  $P < 0.001$  for all data. *Post hoc* statistical calculation of sample sizes for immunostaining and electron microscopy was also done to ensure that sample sizes had sufficient power for subsequent statistical analyses (at least 80% power at the 0.05 level of significance for each set of experiments).

In order to reduce experimental bias, experiments were done blind to protect against observer bias. The experimenters were blinded to the conditions for imaging, quantification, and photometry studies. Steps in the experiments were randomized, to minimize the effects of confounding variables, including how mice were chosen for experiments, order of treatments, etc. Imaging was done in the same fashion between conditions. For quantification, cells and fields from brain sections were chosen randomly from the region of interest.

### Degrees of freedom and F/t values in figures

**Figure 1D:**  $F(3, 119)=16.06$  (number);  $F(3, 119)=22.83$  (size). **Figure 1E:**  $F(3, 124)=45.45$  (number);  $F(3, 124)=30.45$  (size). **Figure 1F:**  $F(4, 70)=66.26$  (number);  $F(4, 70)=25.97$  (size). **Figure 1I:**  $F(2, 48)=56.75$  (number);  $F(2, 48)=40.12$  (size). **Figure 1J:**  $F(2, 41)=34.00$  (number);  $F(2, 41)=34.44$  (size). **Figure 1K:**  $F(2, 57)=71.53$ . **Figure 1L:**  $F(2, 69)=137.3$ . **Figure 2I:**  $F(3, 53)=11.55$  (GIRK2<sup>+</sup>, TH<sup>+</sup> cells, number);  $F(3, 53)=10.32$  (GIRK2<sup>+</sup>, TH<sup>+</sup> cells, size);  $F(3, 51)=18.09$  (Calbindin<sup>+</sup>, TH<sup>+</sup> cells, number);  $F(3, 51)=7.07$  (Calbindin<sup>+</sup>, TH<sup>+</sup> cells, size). **Figure 2J:**  $F(3, 87)=27.87$  (number);  $F(3, 87)=28.29$  (size). **Figure 2K:**  $F(2, 34)=54.44$  (number);  $F(2, 34)=17.38$  (size). **Figure 2L:**  $F(3, 68)=20.69$  (number);  $F(3, 68)=28.64$  (size). **Figure 2M:**  $F(3, 60)=4.21$  (number);  $F(3, 60)=9.50$  (size). **Figure 3C:**  $F(3, 62)=43.87$  (number);  $F(3, 62)=29.93$  (size). **Figure 3F:**  $F(3, 54)=12.03$  (number);  $F(3, 54)=13.59$  (size). **Figure 3G:**  $F(3, 62)=0.098$ . **Figure 3H:**  $F(3, 83)=1.38$ . **Figure 3I:**  $t(17)=5.49$  (*Bmp6*-shRNA, CPu, density);  $t(18)=5.21$  (*Bmp6*-shRNA, CPu, size);  $t(20)=6.22$  (*Bmp2*-shRNA, CPu, density);  $t(23)=2.56$  (*Bmp2*-shRNA, CPu, size);  $t(13)=7.98$  (*Tgfb2*-shRNA, NAc, density);  $t(26)=3.13$  (*Tgfb2*-shRNA, NAc, size). **Figure 3J:**  $t(22)=1.93$  (*Tgfb2*-shRNA, CPu, density);  $t(21)=4.86$  (*Tgfb2*-shRNA, CPu, size);  $t(14)=3.75$  (*Bmp6*-shRNA, NAc, density);  $t(21)=1.15$  (*Bmp6*-shRNA, NAc, size);  $t(21)=2.28$  (*Bmp2*-shRNA, CPu, density);  $t(21)=1.28$  (*Bmp2*-shRNA, CPu, size). **Figure 4G:**  $t(216)=15.71$  (BMPR);  $t(65)=6.84$  (TGF $\beta$ 2). **Figure 4H:**  $F(3, 56)=21.44$  (number);  $F(3, 56)=12.60$  (size). **Figure 4I:**  $F(3, 53)=19.00$  (number);  $F(3, 53)=13.99$  (size). **Figure 4L:**  $F(3, 10)=80.52$ . **Figure 4M:**  $F(3, 9)=34.37$ . **Figure 4P:**  $t(7)=5.07$ . **Figure 4Q:**  $t(10)=3.60$ . **Figure 5C:**  $t(31)=5.839$  (CPu, number);  $t(31)=8.512$  (CPu, size). **Figure 5F:**  $t(46)=3.948$  (NAc, number);  $t(46)=5.401$  (NAc, size). **Figure 5O:**  $t(118)=5.591$  (CPu). **Figure 5P:**  $t(113)=3.864$  (NAc). **Figure 6A:**  $t(18)=4.113$  (control and *Smad1cKO* mice). **Figure 6B:**  $t(43)=3.120$  (control and *Smad1cKO* mice). **Figure 6C:**  $t(8)=4.596$  (control and *Smad1cKO* mice, both paw landing, SNc);  $t(8)=3.490$  (control and *Smad1cKO* mice, ipsilateral paw landing, SNc). **Figure 6F:**  $t(18)=3.655$  (control and *Smad1cKO* mice, VD);  $t(18)=2.352$  (control and *Smad2cKO* mice, RL). **Figure 6G:**  $t(18)=2.620$  (control and *Smad1cKO* mice, VD). **Figure 6H:**  $t(18)=3.631$  (control and *Smad1cKO* mice, VD). **Figure 6I:**  $F(1, 18)=4.99$  (control and *Smad2cKO* mice). **Figure 6J:**  $t(78)=2.700$  (control and *Smad2cKO* mice, RL).

# Supplemental figures

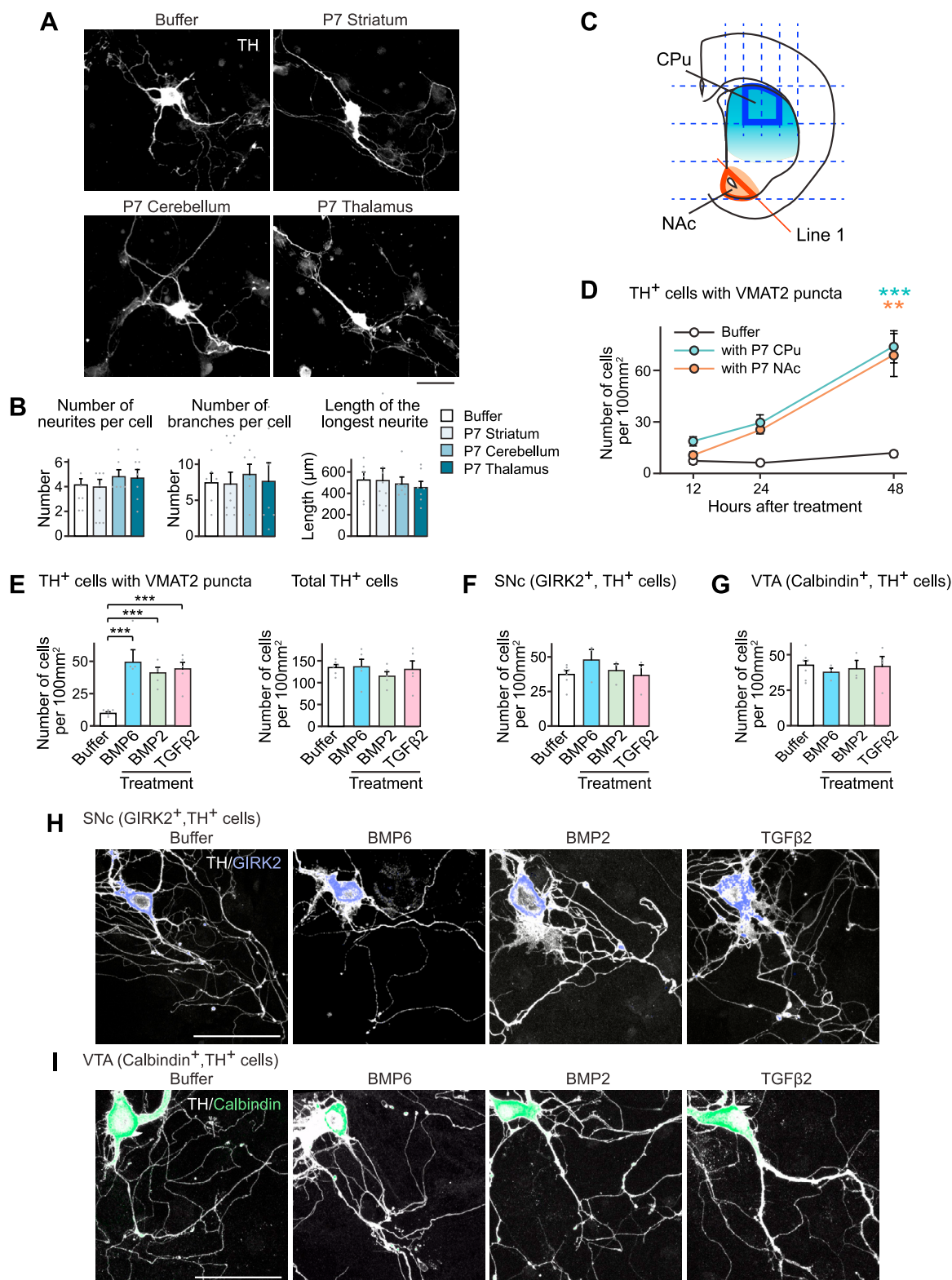




**Figure S1. P7 striatal extract, BMP6, BMP2, and TGF- $\beta$ 2 induce VMAT2 clustering in mDA neurons without affecting their number and morphology in culture, related to Figures 1 and 2**

(A and B) Application of rat brain extracts does not alter the morphology of cultured mDA neurons (related to Figure 1). Midbrain neuronal cultures were treated with extracts prepared from the P7 striatum, cerebellum, or thalamus at 4 DIV. At 7 DIV, cells were fixed and stained for TH. (A) Representative images. (B) The number of neurites per cell, the number of branches per cell, and the length of the longest neurite were quantified. Scale bar, 50  $\mu$ m. Data are shown as mean  $\pm$  SEM. Data are from 6 to 9 cells from 4 to 6 independent experiments. Statistical analysis was done by one-way ANOVA followed by Tukey's test.

(C and D) Application of CPu or NAc extract induces VMAT2 clustering in cultured mDA neurons (related to Figure 1). (C) Schematic illustration of the areas dissected to prepare CPu and NAc samples. Rat forebrain coronal slices (400- $\mu$ m thickness) were placed in Hank's balanced salt solution (HBSS) for dissection. To prepare the CPu sample (the area marked with the solid blue line), the dorsal one-third of the striatum (see dotted horizontal lines) was dissected out and vertically divided into four pieces (see dotted vertical lines). The middle two pieces were used as CPu samples. To prepare the NAc sample (the red area), the NAc more ventral from a 45° angled line (relative to a horizontal line) drawn from the ventral end of the lateral ventricle (line 1) was dissected. (D) Time course of the number of mDA neurons (TH-positive, [TH<sup>+</sup>]) with VMAT2 puncta after the extract treatment. 48-h treatment with the CPu or NAc extracts dramatically increased the number of mDA neurons with VMAT2 puncta. Data are shown as mean  $\pm$  SEM. Data are from 3 coverslips from 3 independent experiments. Significant differences from control (Buffer) at \*\*p < 0.01 and \*\*\*p < 0.001 by one-way ANOVA followed by Tukey's test.

(E–I) BMP6, BMP2, and TGF- $\beta$ 2 induce VMAT2 clustering in mDA neurons without affecting the number and morphology of SNc and VTA dopaminergic neurons in culture (related to Figure 2). Midbrain cultures were treated with recombinant BMP6, BMP2, or TGF- $\beta$ 2 at 3 DIV. Cells were stained at 7 DIV. (E) 4-day treatment with 10 ng/mL of BMP6 or BMP2 or 2 ng/mL of TGF- $\beta$ 2 significantly increased the number of mDA (TH-positive) neurons with VMAT2 puncta (left graph), without changing the total number of mDA neurons (right graph). (F) Treatment with BMP6, BMP2, or TGF- $\beta$ 2 did not alter the number of SNc dopaminergic neurons (GIRK2-positive, TH-positive cells). (G) Treatment with BMP6, BMP2, or TGF- $\beta$ 2 did not alter the number of VTA dopaminergic neurons (calbindin-positive, TH-positive cells). (H and I) Representative images (TH staining) of cultured SNc (GIRK2-positive, blue) and VTA (calbindin-positive, green) dopaminergic neurons treated with factors. Treatment with BMP6, BMP2, or TGF- $\beta$ 2 did not apparently affect the neurite elongation and overall morphology of cultured SNc (H) and VTA (I) dopaminergic neurons. Observations were from 12 to 15 cells from 3 to 5 independent experiments. Scale bars are 50  $\mu$ m. Bars in the graphs are mean  $\pm$  SEM. Data are from (E) 5–6 coverslips from 5 to 6 independent experiments, and (F and G) 3–7 coverslips from 3 to 7 independent experiments. Statistical analysis was done by one-way ANOVA followed by Tukey's test. Significant differences from control (Buffer) at \*\*\*p < 0.001.

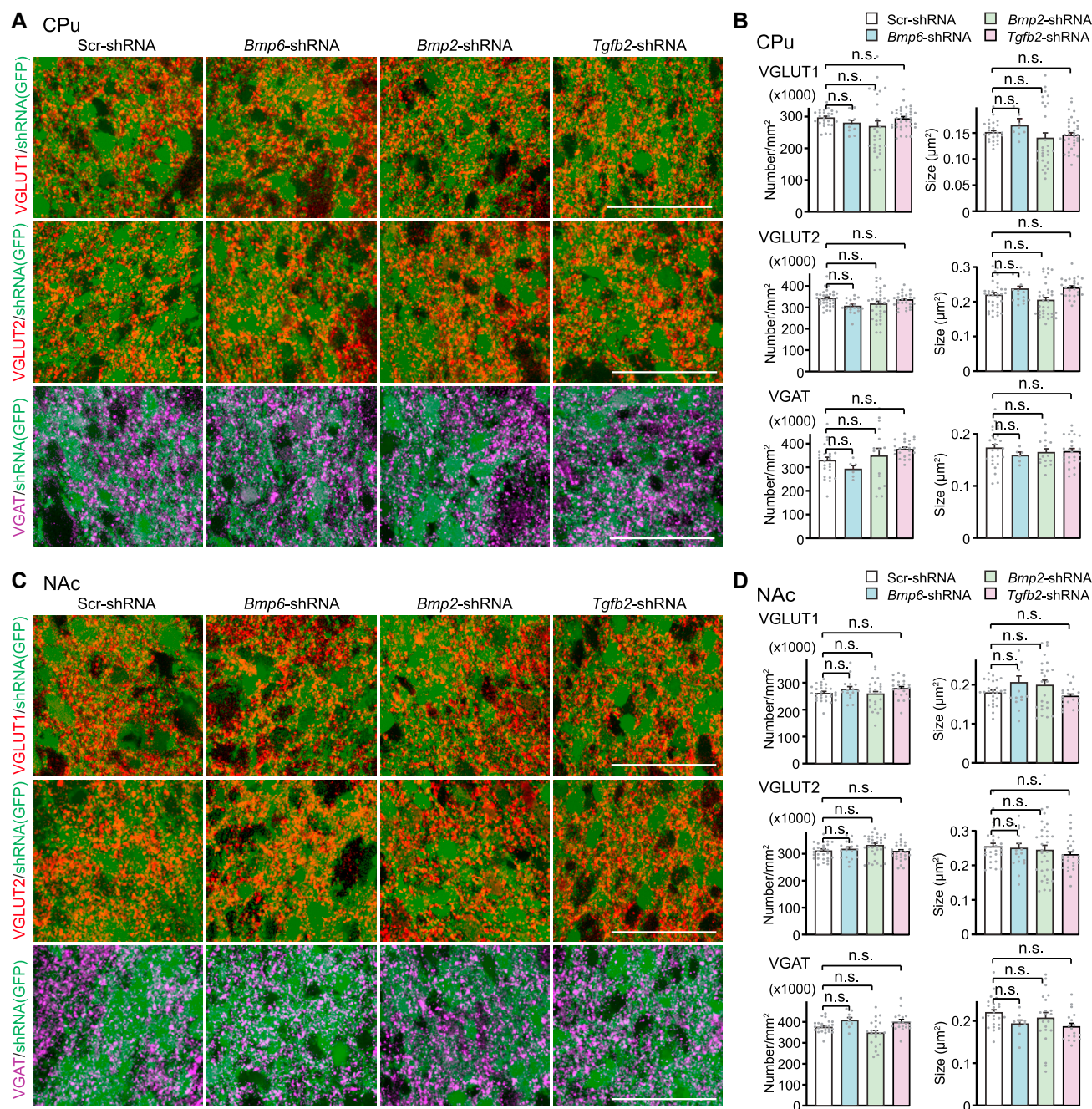


**Figure S2. Knockdown of BMP6, BMP2, or TGF- $\beta$ 2 in the rat CPu and NAc does not affect glutamatergic and GABAergic presynaptic differentiation, related to Figure 3**

Lentivirus expressing either *Bmp6*-shRNA, *Bmp2*-shRNA, *Tgfb2*-shRNA, or scramble-shRNA, together with GFP, was injected into the rat CPu or NAc at P3 by stereotaxic injection. Brains were stained at P12.

(A and B) Glutamatergic and GABAergic synapses in the CPu. (A) Representative pictures of sections stained for VGLUT1, VGLUT2, or VGAT. Virus-infected areas are in green. (B) Quantification of the density and size of VGLUT1, VGLUT2, and VGAT puncta in the virus-infected areas in the CPu. VGLUT1, VGLUT2, and VGAT clustering in the BMP6, BMP2, or TGF- $\beta$ 2 knocked down areas was not significantly different from that in the scramble-shRNA expressing areas.

(C and D) Glutamatergic and GABAergic synapses in the NAc. (C) Representative pictures of stained sections for VGLUT1, VGLUT2, or VGAT. (D) Quantification of the density and size of VGLUT1, VGLUT2, and VGAT puncta in the virus-infected areas in the NAc. VGLUT1, VGLUT2, and VGAT clustering in the BMP6, BMP2, or TGF- $\beta$ 2 knocked down areas was not significantly different from that in the scramble-shRNA expressing areas. Scale bars, 50  $\mu$ m. Bars in the graphs are mean  $\pm$  SEM. Data are from (B) 6–36 fields from 3 sections from 2 to 4 animals and (D) 9–33 fields from 3 sections from 2 to 3 animals. Statistical analysis was done by one-way ANOVA followed by Tukey's test.

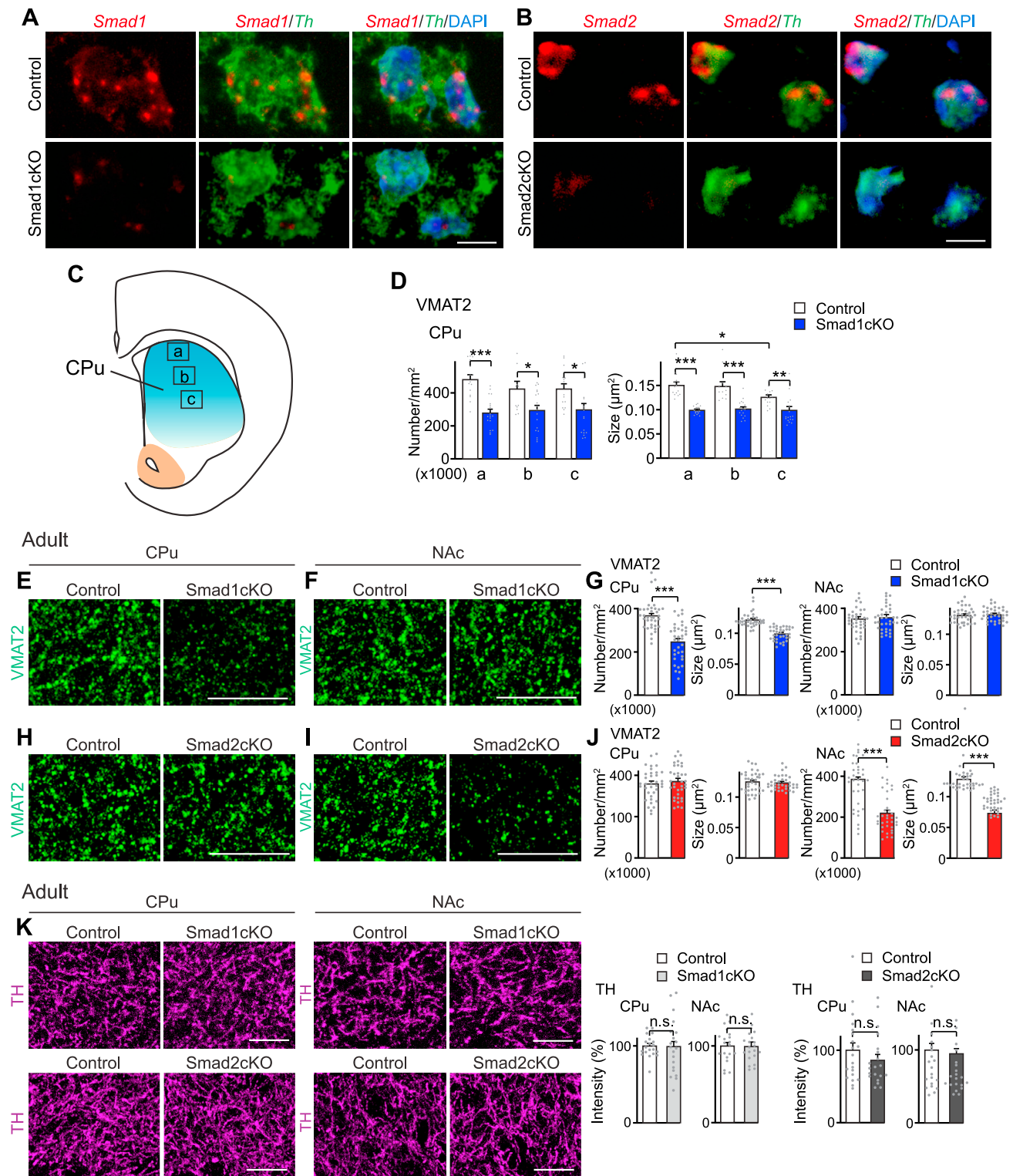


**Figure S3. Pathway-specific defects in dopaminergic presynaptic differentiation in P14 and adult Smad1cKO and Smad2cKO mice, related to Figure 5**

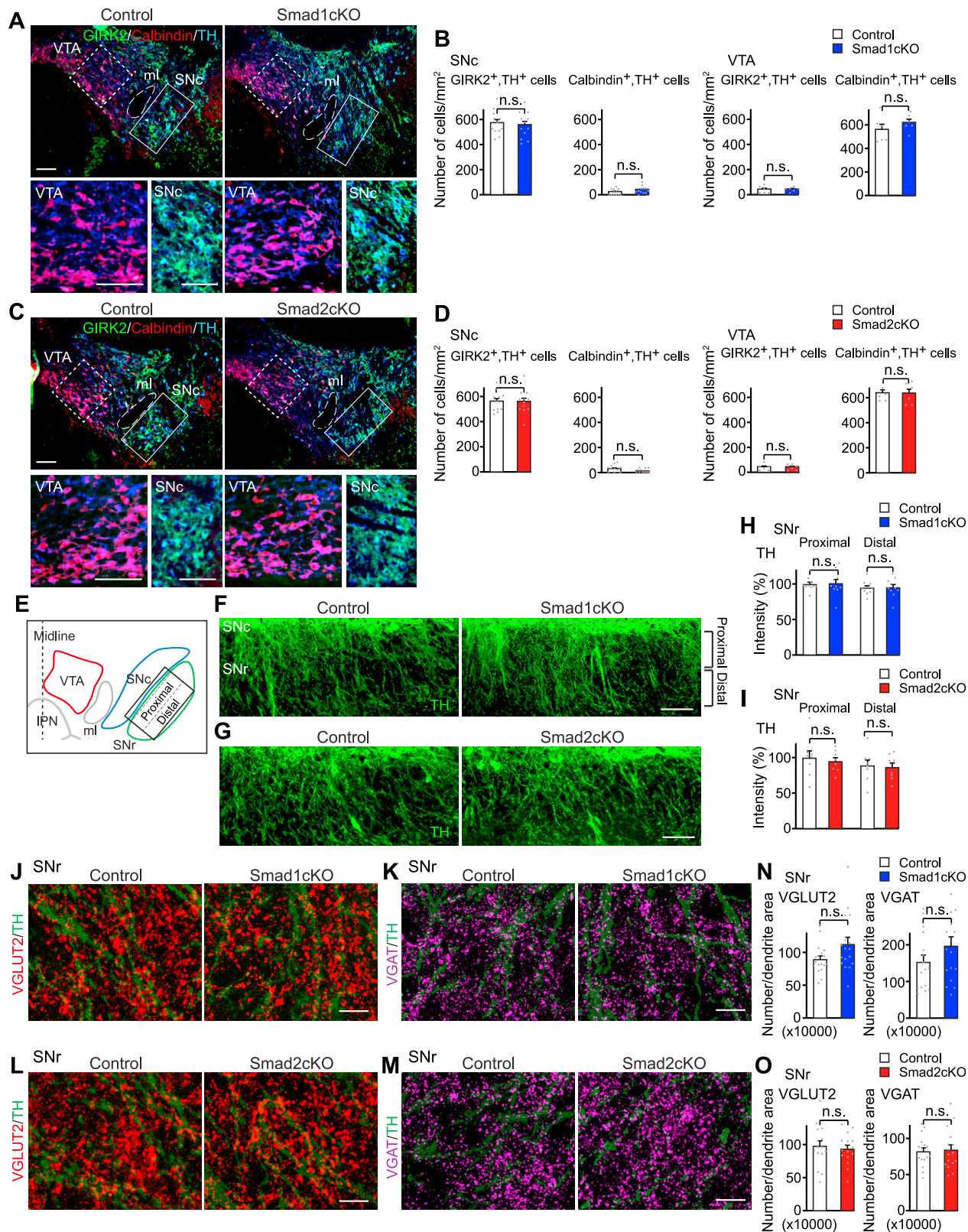
(A and B) Verification of Smad1cKO and Smad2cKO mice. Sections prepared from P10 Smad1cKO (*Smad1<sup>flx/flx</sup>::DAT-CreER*), Smad2cKO (*Smad2<sup>flx/flx</sup>::DAT-CreER*), and control (*Smad<sup>wt/wt</sup>::DAT-CreER*) mice (tamoxifen injections at P1) were subjected to RNAscope *in situ* hybridization. (A) RNAscope *in situ* hybridization with midbrain sections prepared from Smad1cKO and control mice for *Smad1* (red) and *Th* (green). Almost no *Smad1* signal was detected in *Th*-positive

(legend continued on next page)



mDA neurons in *Smad1cKO* mice. (B) RNAscope *in situ* hybridization with midbrain sections prepared from *Smad2cKO* and control mice for *Smad2* (red) and *Th* (green). Almost no *Smad2* signal was detected in mDA neurons in *Smad2cKO* mice. Observations were from 2 sections/mouse, 3–4 mice. Scale bars, 10  $\mu$ m. (C and D) The defects in VMAT2 accumulation in *Smad1cKO* mice are more significant in the dorsal CPU than in ventral CPU. Striatal sections from P14 from *Smad1cKO* and control mice were immunostained for VMAT2. The rectangles in (C) show the locations of the dorsal (a), middle (b), and ventral (c) regions of the CPU used for analysis. The graphs in (D) show the density and size of VMAT2 puncta in the dorsal (a), middle (b), and ventral (c) regions of the CPU of *Smad1cKO* and control mice. In the control mice, the density and size of VMAT2 puncta showed a gradient pattern: highest in the dorsal and lowest in the ventral region of the CPU. In *Smad1cKO* mice, the decrease in VMAT2 clustering was more severe in the dorsal CPU than in the middle or ventral CPU. Bars in the graphs are mean  $\pm$  SEM. Data are from 12 to 18 fields from 4 to 5 mice. Significant differences at \* $p < 0.05$ , \*\* $p < 0.01$ , \*\*\* $p < 0.001$  by one-way ANOVA followed by Tukey's test. (E–K) Pathway-specific defects in dopaminergic presynaptic differentiation persist in adult *Smad1cKO* and *Smad2cKO* mice. Striatal sections from adult (3–4 months old) *Smad1cKO*, *Smad2cKO*, and control mice were immunostained for VMAT2 (green) and TH (magenta). (E–G) *Smad1cKO* and control mice. Representative images from the CPU (E) and NAc (F). (G) Quantification of the density and size of VMAT2 puncta in the CPU and NAc. VMAT2 clustering was significantly decreased in the CPU, but not NAc, of adult *Smad1cKO* mice relative to control mice. (H–J) *Smad2cKO* and control mice. Representative images from the CPU (H) and NAc (I). (J) Quantification of the density and size of VMAT2 puncta in the CPU and NAc. VMAT2 clustering was significantly decreased in the NAc, but not CPU, of adult *Smad2cKO* mice relative to control mice. (K) Quantification of the intensity of TH staining (% control) in the CPU and NAc of adult mice. The intensity of TH staining was similar between adult *Smad1cKO*, *Smad2cKO*, and control mice. Bars in the graphs are mean  $\pm$  SEM. Scale bars, 10  $\mu$ m. Data are from (G and J) 36 fields from 3 mice, and (K) 20 fields from 5 mice. Significant differences from control at \*\*\* $p < 0.001$  by Student's *t* test. n.s., not significant.





(legend on next page)

**Figure S4. The number of SNc and VTA mDA neurons, dendritic development of mDA neurons, and glutamatergic and GABAergic synapses formed onto them in Smad1cKO and Smad2cKO mice, related to Figure 5**

(A–D) No change in the numbers of SNc and VTA mDA neurons in Smad1cKO and Smad2cKO mice. Midbrain sections from P14 Smad1cKO, Smad2cKO, and control mice were immunostained for GIRK2 (green), calbindin (red), and TH (blue). (A and B) Smad1cKO and control mice. (C and D) Smad2cKO and control mice. (A and C) Representative images from the ventral midbrain. Dotted squares (magnified in bottom panels) show the VTA areas analyzed, and rectangles (magnified in bottom panels) show the SNc areas analyzed. (B and D) Quantification of the numbers of GIRK2-positive, TH-positive neurons (nigrostriatal dopaminergic neurons) and calbindin-positive, TH-positive neurons (mesolimbic dopaminergic neurons) in the SNc and VTA.

(E–I) No defects in the dendritic development of mDA neurons in Smad1cKO and Smad2cKO mice. Midbrain sections from P14 Smad1cKO, Smad2cKO, and control mice were immunostained for TH (green). (E) A schematic diagram of the ventral midbrain. (F and G) Representative images from the SNr of Smad1cKO and control mice (F) and Smad2cKO and control mice (G). The intensities of TH immunostaining in the proximal and distal regions of the SNr (relative to the intensity in the proximal region of the control) are shown in graphs (H and I).

(J–O) No defects in the glutamatergic and GABAergic synapses formed onto mDA neurons in Smad1cKO and Smad2cKO mice. Midbrain sections from P14 Smad1cKO, Smad2cKO, and control mice were immunostained for VGLUT2 (red) and TH (green) to examine glutamatergic synapses on mDA neurons, or VGAT (magenta) and TH (green) to examine GABAergic synapses on mDA neurons. (J–M) Representative images from the SNr of Smad1cKO and control mice (J and K) and Smad2cKO and control mice (L and M). The numbers of VGLUT2 puncta or VGAT puncta on TH-positive dendrites in the SNr were quantified (number per dendrite area [ $\mu\text{m}^2$ ]) and shown in graphs (N and O). No significant change was found in VGLUT2 and VGAT accumulation on mDA neurons in the SNr in either Smad1cKO or Smad2cKO mice. Bars in the graphs are mean  $\pm$  SEM. Data are from 6 to 12 fields from 3 mice (B and D), 8–10 fields from 4 to 5 mice (H and I), 15–18 fields from 3 to 4 mice (N and O), Student's *t* test. n.s., not significant; SNr, substantia nigra pars reticulata; ml, medial lemniscus; IPN, interpeduncular nucleus. Scale bars, 100  $\mu\text{m}$  (A, C, F, and G) and 10  $\mu\text{m}$  (J–M).



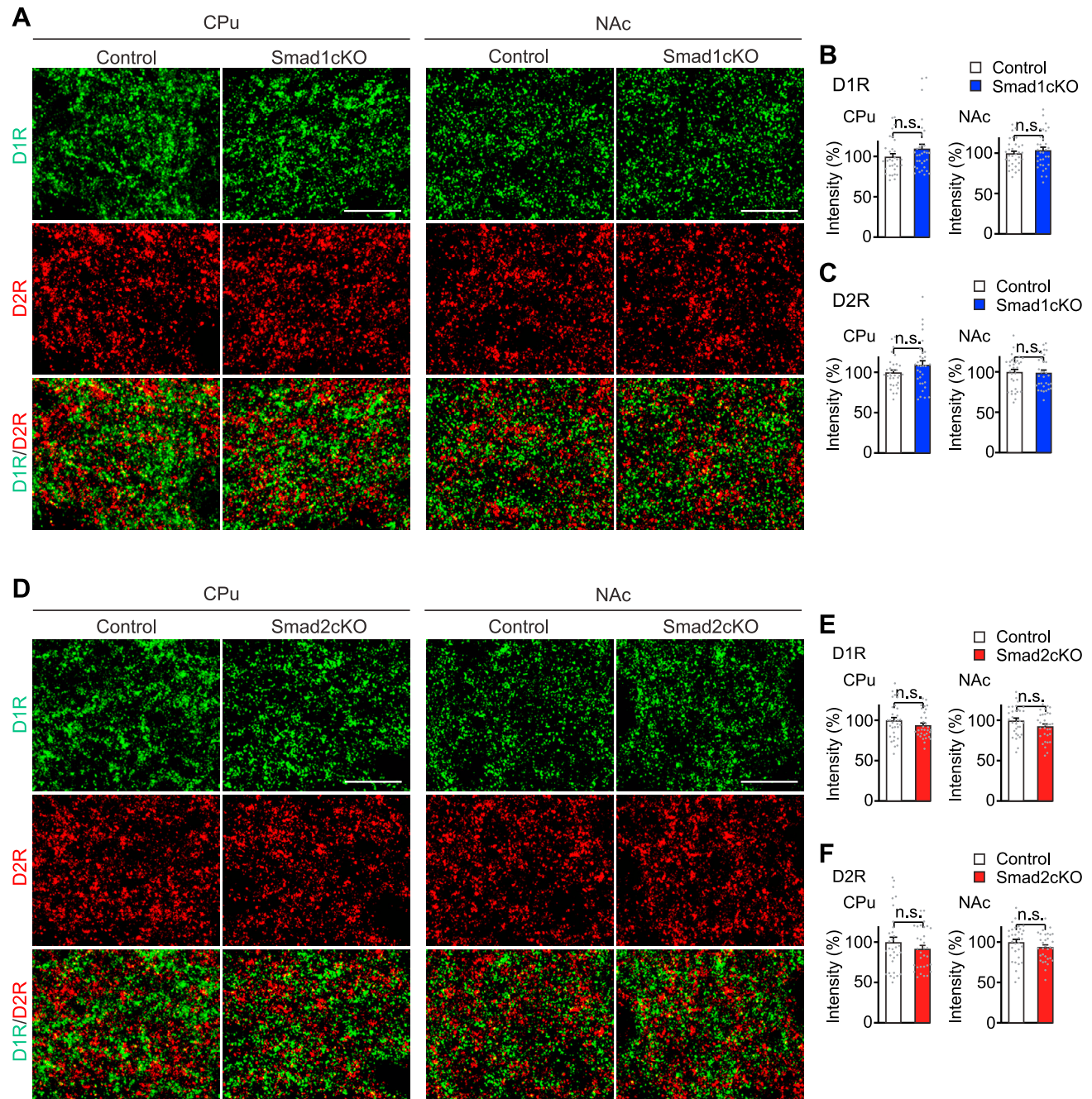


**Figure S5. No change in the intensity of D1R and D2R puncta in Smad1cKO and Smad2cKO mice, related to Figure 5**

Striatal sections from P14 Smad1cKO, Smad2cKO, and control mice were immunostained for dopamine D1 receptor (D1R, green) and dopamine D2 receptor (D2R, red).

(A–C) Smad1cKO mice. (A) Representative images from the CPu and NAc of Smad1cKO and control mice. The intensities of D1R (B) and D2R (C) immunostaining (relative to the control) are shown in graphs.

(D–F) Smad2cKO mice. (D) Representative images from the CPu and NAc of Smad2cKO and control mice. The intensities of D1R (E) and D2R (F) immunostaining (relative to the control) are shown in graphs. Scale bars, 10  $\mu$ m. Bars in the graphs are mean  $\pm$  SEM. Data are from 32 fields from 4 mice, Student's t test. n.s., not significant.

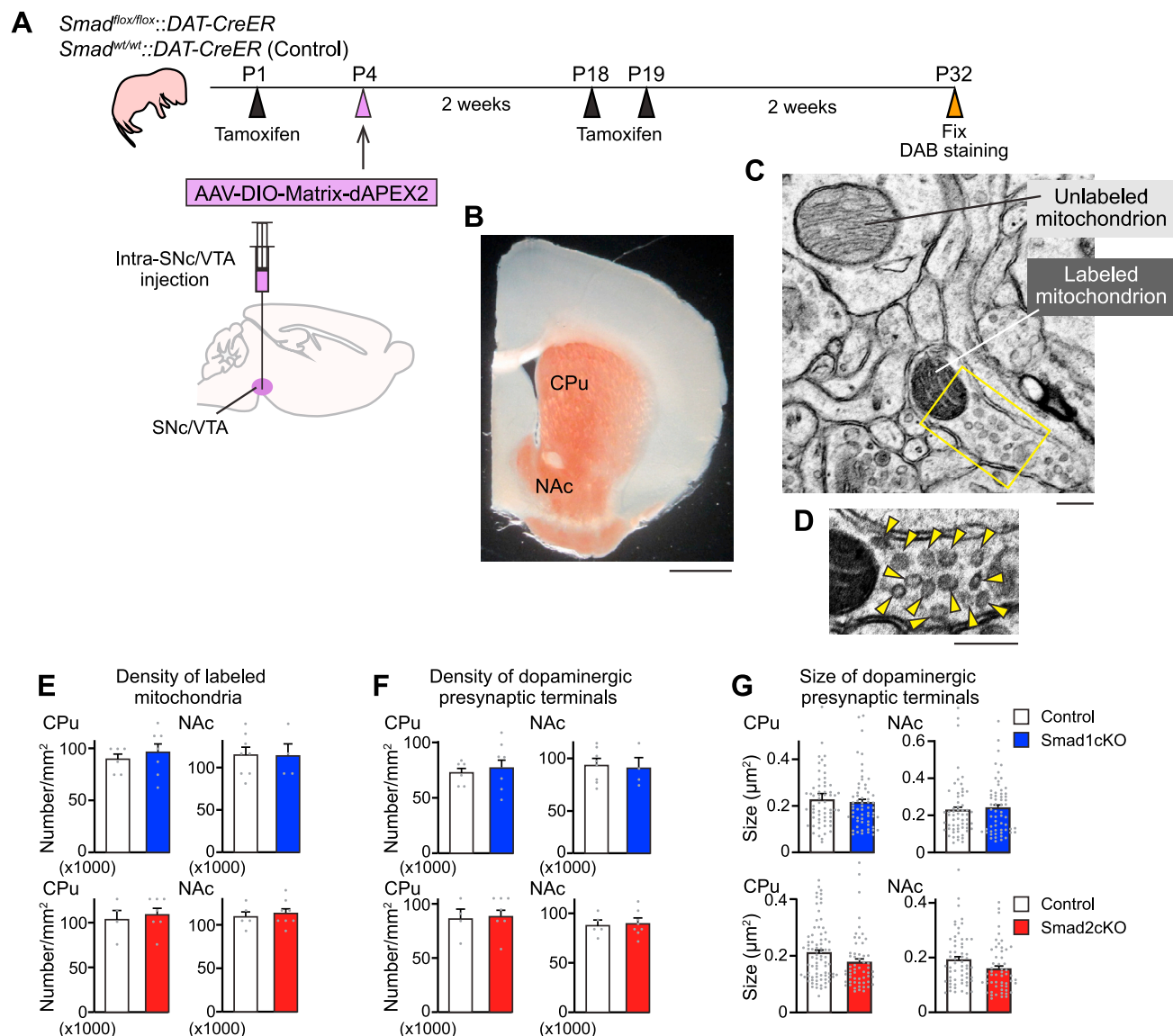


**Figure S6. dAPEX2-based labeling of dopaminergic presynaptic terminals for electron microscopic analysis, related to Figure 5**

(A) Experimental flow diagram. To inactivate *Smad1* or *Smad2* postnatally in dopaminergic neurons, *Smad1<sup>flox/flox</sup>::DAT-CreER* and *Smad2<sup>flox/flox</sup>::DAT-CreER* mice were administered with tamoxifen at P1. *Smad<sup>wt/wt</sup>::DAT-CreER* mice were used as controls. To label dopaminergic presynaptic terminals, AAV-DIO-Matrix-dAPEX2 was injected into the midbrain at P4. At P18 and P19, tamoxifen was injected to express Matrix-dAPEX2 in mDA neurons. At P32, striatal sections were prepared and stained with diaminobenzidine (DAB), followed by electron microscopic analysis.

(B) A representative image of a striatal section after DAB staining. The entire striatum is labeled with Matrix-dAPEX2 (DAB oxidized by dAPEX2 forms an orange/brown precipitate).

(C) A representative electron microscopic image from the striatum. A non-labeled mitochondrion (i.e., in a non-mDA neuron) and a dAPEX2-labeled mitochondrion (i.e., in an mDA neuron) are indicated.

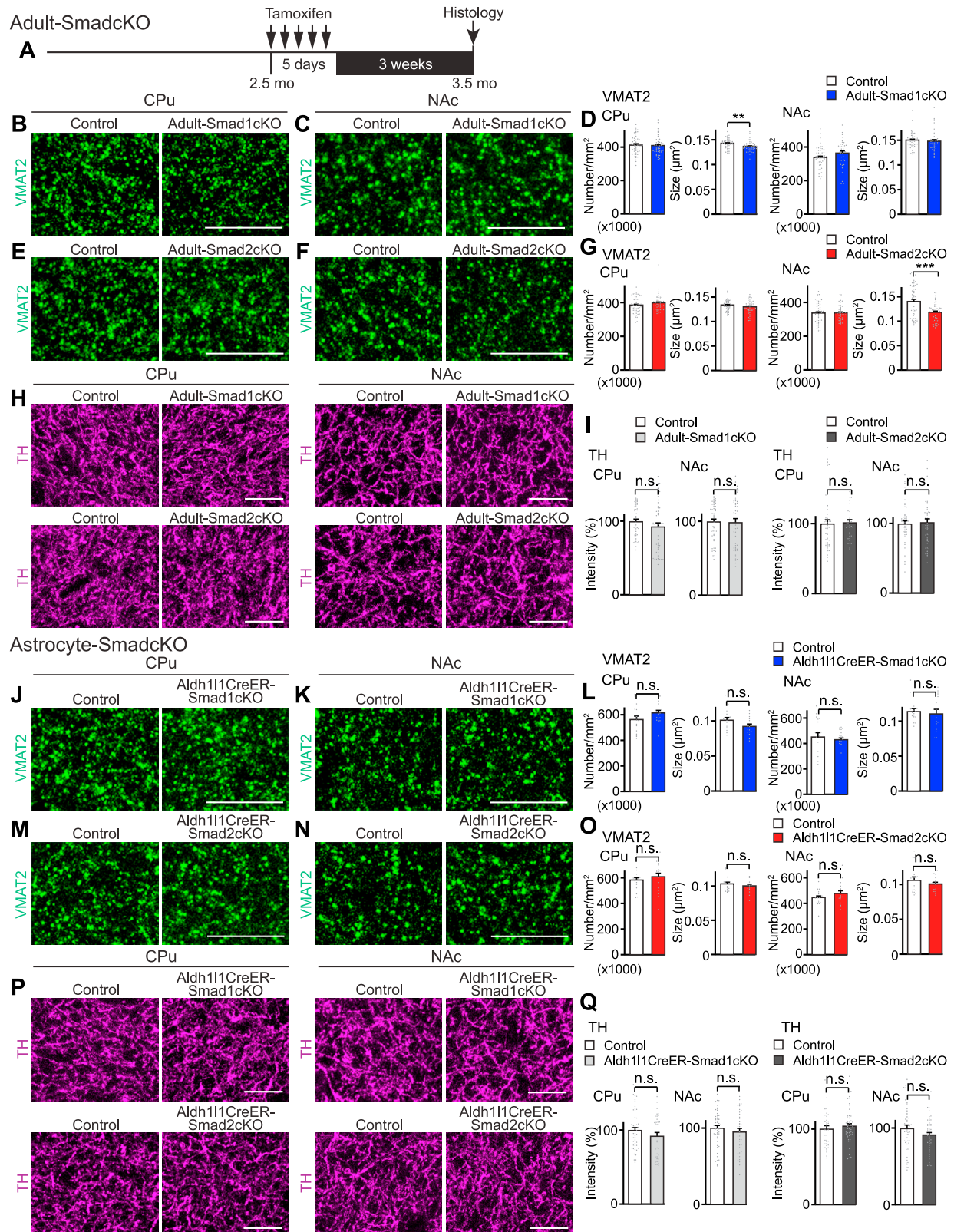
(D) A dopaminergic presynaptic terminal containing a labeled mitochondrion and many dopaminergic synaptic vesicles (SVs; yellow arrowheads).

(E) The density of labeled mitochondria in the striatum (#/mm<sup>2</sup>) was not significantly different between *Smad1cKO* and control mice.

(F) The density of dopaminergic presynaptic terminals in the CPu and NAc (#/mm<sup>2</sup>) was not significantly different between *Smad1cKO* and control mice. Dopaminergic presynaptic terminals were defined as boutons containing a labeled mitochondrion and at least one SV.

(G) The average size of dopaminergic presynaptic terminals in the CPu and NAc was not significantly different between *Smad1cKO* and control mice. Bars in the graphs are mean ± SEM. Data are from (E and F) 4–8 fields from 2 to 3 mice and (G) 55–80 dopaminergic presynaptic terminals from 3 to 4 mice. Scale bars are (B) 1 mm, (C and D) 200 nm.





(legend on next page)

**Figure S7. Dopaminergic presynaptic differentiation in mice in which Smad is inactivated in DA neurons in adult (adult SmadcKO) and in mice in which Smad is inactivated in astrocytes (astrocyte-SmadcKO), related to Figure 5**

(A–I) Smad1 and Smad2 contribute to the maintenance of dopaminergic synapses in adults in a pathway-specific manner. (A) Experimental timeline of the generation and analysis of adult-Smad1cKO and adult-Smad2cKO mice. *Smad1<sup>flox/flox</sup>::DAT-CreER* and *Smad2<sup>flox/flox</sup>::DAT-CreER* mice were injected with tamoxifen at 2.5 months of age (20 mg/kg for 5 days) to generate adult-Smad1cKO and adult Smad2cKO. Histological analysis was performed at the age of 3.5 months. (B–G) Striatal sections from adult-Smad1cKO, adult-Smad2cKO, and their control mice were immunostained for VMAT2 (green). (B and C) Representative images from the CPu (B) and NAc (C) of adult-Smad1cKO and control mice. (D) Quantification of the density and size of VMAT2 puncta in the CPu and NAc in adult-Smad1cKO and control mice. The size of VMAT2 puncta was significantly decreased in the CPu, but not NAc, of adult-Smad1cKO mice relative to control mice. (E and F) Representative images from the CPu (E) and NAc (F) of adult-Smad2cKO and control mice. (G) Quantification of the density and size of VMAT2 puncta in the CPu and NAc in adult-Smad2cKO and control mice. The size of VMAT2 puncta was significantly decreased in the NAc, but not CPu, of adult-Smad2cKO mice relative to control mice. (H and I) Striatal sections from adult-Smad1cKO, adult-Smad2cKO, and their control mice were immunostained for TH (magenta). (H) Representative images from the CPu and NAc of adult-Smad1cKO, adult-Smad2cKO, and their control mice. (I) The intensity of TH staining (% of control) was similar between adult-Smad1cKO, adult-Smad2cKO, and their control mice.

(J–Q) Postnatal inactivation of Smads in astrocytes has no effect on dopaminergic presynaptic differentiation in the striatum. *Smad1<sup>flox/flox</sup>::Aldh111-CreER*, *Smad2<sup>flox/flox</sup>::Aldh111-CreER*, and *Smad<sup>wt/wt</sup>::Aldh111-CreER* (control) mice were injected with tamoxifen at P1. Histological analysis was performed at P60. (J–O) Striatal sections from Aldh111CreER-Smad1cKO, Aldh111CreER-Smad2cKO, and their control mice were immunostained for VMAT2 (green). (J and K) Representative images from the CPu (J) and NAc (K) of Aldh111CreER-Smad1cKO and control mice. (L) Quantification of the density and size of VMAT2 puncta in the CPu and NAc in Aldh111CreER-Smad1cKO and control mice. (M and N) Representative images from the CPu (M) and NAc (N) of Aldh111CreER-Smad2cKO and control mice. (O) Quantification of the density and size of VMAT2 puncta in the CPu and NAc in Aldh111CreER-Smad2cKO and control mice. In both Aldh111CreER-SmadcKO mice, VMAT2 clustering was not altered in the CPu and NAc. (P and Q) Striatal sections from Aldh111CreER-Smad1cKO, Aldh111CreER-Smad2cKO, and their control mice were immunostained for TH (magenta). (P) Representative images from the CPu and NAc of Aldh111CreER-Smad1cKO, Aldh111CreER-Smad2cKO, and their control mice. (Q) The intensity of TH staining (% of control) was similar in Aldh111CreER-Smad1cKO, Aldh111CreER-Smad2cKO, and control mice. Scale bars, 10  $\mu$ m. Bars in the graphs are mean  $\pm$  SEM. Data are from (D) 36–48 fields from 3 to 4 mice, and (G) 42–48 fields from 4 mice, (I) 48 fields from 4 mice, (L and O) 32 fields from 4 mice, and (Q) 48 fields from 4 mice. Significant differences from control at \*\*p < 0.01, \*\*\*p < 0.001 by Student's t test. n.s., not significant.